The sub-damped Ly α system toward HE 0515–4414

Dissertation
zur Erlangung des Doktorgrades
des Fachbereichs Physik
der Universität Hamburg

vorgelegt von
Ralf Quast
aus Hamburg

Hamburg
2006

Gutachter der Dissertation:	Prof. Dr. Dieter Reimers Prof. Dr. Lutz Wisotzki
Gutachter der Dissertation:	Prof. Dr. Dieter Reimers Prof. Dr. Peter H. Hauschildt
Datum der Disputation:	24.02.2006
Vorsitzender des Prüfungsausschusses:	PD Dr. Franz-Josef Zickgraf
Vorsitzender des Promotionsauschusses:	Prof. Dr. Günter Huber
Dekan des Fachbereichs Physik:	Prof. Dr. Günter Huber

ZUSAMMENFASSUNG

Kontext: Extragalaktische Absorber mit einer Säulendichte von $N_{\mathrm{H\,I}} \geq 2 \times 10^{20}$ Wasserstoffatomen cm^{-2} werden als gedämpfte Ly α (DLA) Systeme bezeichnet. Diese Absorber bestehen im wesentlichen aus vorwiegend neutralem Gas, eine Grundvoraussetzung für die Entstehung von Sternen. Die Spektroskopie dieser Absorber bietet somit die beste Möglichkeit, die chemische Zusammensetzung dieser Äquivalente des interstellaren Mediums lokaler Galaxien in einem früheren Stadium der kosmischen Entwicklung zu studieren. Absorber im sub-DLA Bereich mit $N_{\mathrm{H\,I}} \geq 10^{19}$ cm^{-2} können ebenfalls aus überwiegend neutralem Gas bestehen, wenn der kosmische UV Hintergrund reduziert ist. Die beobachtete kinematische Struktur der Absorptionslinien, sowie die Statistik über Säulendichte und Metallizität der Absorber sind wesentliche Prüfsteine für Modelle der Galaxienentstehung und kosmischen Strukturbildung. Detektierte Feinstrukturlinien bieten die Möglichkeit, die aus der Friedmann-Kosmologie folgende Relation zwischen Rotverschiebung und Temperatur der kosmischen Mikrowellenhintergrundstahlung zu überprüfen, oder auf die physikalischen Bedingungen innerhalb der Absorber rückzuschließen. Genaue Messungen der relativen Abstände ausgewählter Metalllinien können der von vielen gegenwärtig diskutierten Theorien zur Vereinigung der Wechselwirkungen eingeforderten kosmologischen Veränderlichkeit der Feinstrukturkonstanten α Grenzen auferlegen.

Vorhaben: Es werden die Ionisation, Häufigkeit und Staubkondensation von Metallen in dem sub-DLA System in Richtung des Quasars HE 0515–4414 untersucht. Die kinematische Struktur der Metalllinien wird diskutiert. Feinstrukturlinien des neutralen Kohlenstoffs werden benutzt, um auf die Temperatur der kosmischen Mikrowellenhintergrundstahlung bei der Rotverschiebung $z = 1.15$ und die physikalischen Bedingungen innerhalb des absorbierenden Mediums rückzuschließen. Mittels genauer Messung der Abstände einzelner Komponenten innerhalb eines Ensembles von Fe II Resonanzlinien wird die mögliche Abweichung der Feinstrukturkonstanten von ihrem heutigen Wert bestimmt.

Methoden: Empirische Basis der Untersuchungen sind hochaufgelöste Spektren, die mit den Spektrographen STIS und UVES aufgenommen wurden. Im Optischen ist die Qualität der Daten außergewöhnlich. Das für die Analyse der Spektren verwendete Programm wurde von Grund auf neu entwickelt. Herzstück des Programms ist eine Evolutionsstrategie, die auf einer derandomisierten Adaption der Kovarianzmatrix beruht. Im Gegensatz zu den üblichen deterministischen Optimierungsverfahren, benötigt die Evolutionsstrategie keine spezifische Initialisierung um eine optimale Dekomposition zu berechnen. Die Ionisationsverhältnisse innerhalb des Absorbers wurden mit Hilfe der Simulationssoftware Cloudy analysiert.

Ergebnisse: Das sub-DLA System mit Rotverschiebung $z = 1.15$ ist in mehrfacher Hinsicht außergewöhnlich. Am außergewöhnlichsten ist die Ausdehnung des Absorptionsintervalls der mit der H I Absorption assoziierten Metalllinien, die sich über einen Bereich von 700 $\mathrm{km\,s}^{-1}$ verteilen. Die zweitgrößte Ausdehnung, die in diesem Kontext je beobachtet wurde. Die extreme Ausbreitung des Absorptionsintervalls ermöglicht die ungewöhnliche Detektion zweier periphärer H I Komponenten, im Abstand von 530 und 240 $\mathrm{km\,s}^{-1}$ von der $N_{\mathrm{H\,I}} = 8 \times 10^{19}$ cm^{-2} Hauptkomponente. Die assoziierten Metallinien setzen sich aus mindestens 31 Komponenten zusammen. Die kinematische Verteilung der Komponenten ist bimodal, möglicherweise ein Hinweis auf die Anwesenheit zweier interagierender Absorber. Unterstützt wird diese Interpretation durch den Befund einer uneinheitlichen Ionisationsstruktur. Der Hauptabsorber besteht im wesentlichen aus vorwiegend neutralem Gas, wohingegen die Peripherie hochionisiert ist. Für den Hauptabsorber deuten die relativen Häufigkeiten refraktärer und flüchtiger Elemente auf das Vorhandensein beträchtlicher Mengen von Staub. Das für DLA Systeme ungewöhnlich differenzierte Häufigkeitsmuster ähnelt denen aus dem interstellaren Medium der Milchstraße und dem interstellaren Gas der Magellanschen Wolken bekannten. Die staubkorrigierte Metallizität des Hauptabsorbers ist mit $[\mathrm{Fe/H}] = -0.08 \pm 0.19$ nahezu solar, die unkorrigierte Metallizität ist $[\mathrm{Zn/H}] = -0.38 \pm 0.04$. Die Elementhäufigkeiten in der Peripherie sind mit solaren Werten vergleichbar. Der kosmische Mikrowellenhintergrund trägt zu der beobachteten Besetzung der angeregten Feinstrukturzustände der Kohlenstoffatome nur geringfügig bei. Die Anregung wird vorwiegend durch lokale FUV Strahlung, sowie Kollisionen mit Wasserstoffatomen verursacht. Die kinetische Temperatur des absorbierenden Mediums beträgt einige zehn bis wenige hundert Kelvin. Die gemessene Abweichung der Feinstukturkonstanten von ihrem heutigen Wert $\langle \Delta\alpha/\alpha \rangle = (0.1 \pm 1.7) \times 10^{-6}$ kann die in Arbeiten von John Webb und Michael Murphy gefundene Detektion einer kosmologischen Variation nicht bestätigen. Das Messergebnis der vorliegenden Arbeit wurde mittlerweile von zwei weiteren Autorenteams vollauf bekräftigt.

Schlussfolgerungen: Die Ergebnisse der vorliegenden Arbeit zeigen, dass die chemische Entwicklung des sub-DLA Systems in Richtung HE 0515–4414 ungewöhnlich weit fortgeschritten ist. Da DLA Absorber bei Rotverschiebungen $z \leq 1.5$ diesbezüglich eher hinter den Erwartungen zurückbleiben, stellt sich die Frage, ob das in der vorliegenden Arbeit untersuchte System möglicherweise mehr als nur einen Sonderfall darstellt. Es ist jedoch insbesondere bei niedrigen Rotverschiebungen zu wenig über die Population der sub-DLA Absorber bekannt, um diese Frage beantworten zu können. Moderne Surveys mit einem Detektionslimit unterhalb der traditionellen Schwelle von $N_{\mathrm{H\,I}} = 2 \times 10^{20}$ cm^{-2} könnten interessante Einsichten vermitteln.

ABSTRACT

Context: Extragalactic absorbers with column densities exceeding $N_{\mathrm{H\,I}} = 2 \times 10^{20}$ hydrogen atoms cm^{-2} are generally termed damped Ly α (DLA) systems. The absorbers are basically comprised of predominantly neutral gas, which is an essential prerequisite for the formation of stars. The spectroscopy of absorbers offers the best possibility to study the chemical composition of the supposed equivalents of the interstellar medium of local galaxies at an earlier stage of cosmic evolution. Absorbers in the sub-DLA range with $N_{\mathrm{H\,I}} \geq 10^{19}$ cm^{-2} may consist of predominantly neutral gas, if the cosmic UV background is reduced. The observed kinematic structure of absorption lines as well as the column density and metallicty statistics of absorbers provide substantial tests for models of galaxy formation and cosmic structuring. Fine-structure lines offer the possibility to examine the temperature-redshift relation of the cosmic microwave background radiation predicted by Friedmann cosmology, or to infer the physical condition of the absorbing medium. Precise measurements of the relative positions of selected metal lines can impose stringent constraints on the cosmological variability of the fine structure constant α, which is an implication of many unifying theories currently discussed.

Aims: The primary aim of this study is the examination of the ionization, abundance and dust depletion of metals in the sub-DLA absorber toward the QSO HE 0515–4414. The kinematic structure of metal absorption lines is discussed. Neutral carbon fine-structure lines are used to infer the temperature of the cosmic microwave background at redshift $z = 1.15$, and to diagnose the physical condition of the absorbing medium. Based on accurate positional measurements of individual components within an ensemble of selected Fe II resonance lines, the possible deviation of the fine structure constants from its current value is probed.

Methods: High-resolution spectra obtained with the STIS and UVES spectrographs provide the empirical basis of this work. In the optical the quality of the data is exceptional. The program used for the analysis has been developed from scratch. The software is driven by an evolution strategy, which is based on a derandomized adaptation the covariance matrix. The strategy is proven to be a highly competitive algorithm capable of calculating an optimal line profile decomposition without requiring any particular initialization. The ionization conditions within the absorber have been analyzed using the simulation software Cloudy.

Results: The sub-DLA system with redshift $z = 1.15$ is unusual in several respects. The velocity interval of metal lines associated with the H I absorption extends for more than 700 km s^{-1}, which is the second largest spread yet observed in this context. The extreme spread facillitates the unusual detection of two peripheral H I components located at distances of 530 and 240 km s^{-1} from the $N_{\mathrm{H\,I}} = 8 \times 10^{19}$ cm^{-2} main component. The associated metal lines consist of at least 31 components. The kinematic distribution of metal line components is bimodal, which is possibly indicating the presence of two interacting absorbers. This interpretation is supported by the finding of a nonuniform ionization structure. The main absorber essentially consists of predominantly neutral gas, whereas the periphery is highly ionized. For the former, the abundances ratios of refractory elements to zinc range from Galactic warm disk to halo-like and essentially undepleted patterns. The dust-corrected metallicity of the main absorber is almost solar $[\mathrm{Fe/H}] = -0.08 \pm 0.19$, whereas the uncorrected metallicity is $[\mathrm{Zn/H}] = -0.38 \pm 0.04$. The element abundances in the periphery do conform with solar composition. The cosmic microwave background is only a minor source of the observed population of excited fine-structure levels. The excitation is predominantly caused by local FUV radiation and collisions with hydrogen atoms. The kinetic temperature of the absorbing medium is some ten to hundred Kelvin. The measured deviation of the fine-structure constant from its present value $\langle \Delta\alpha/\alpha \rangle = (0.1 \pm 1.7) \times 10^{-6}$ does not confirm the detection of a cosmological variation found in the studies of John Webb and Michael Murphy. The present measurement has been affirmed by two further research teams.

Conclusions: The present study shows that the chemical evolution of sub-DLA system toward HE 0515–4414 must have reached an advanced state. Since in this context regular DLA absorbers fall behind expectations at redshifts $z \leq 1.5$, the question arises whether the sub-DLA absorber examined in the present work is more than just an exceptional case. In particular at lower redshifts the population of sub-DLA absorbers is largely unknown. Modern Surveys setting the detection limit below the traditional threshold of $N_{\mathrm{H\,I}} = 2 \times 10^{20}$ cm^{-2} may provide interesting insights.

Inhalt

Vorwort

Der erste Teil dieser Dissertation besteht aus einer Synopsis, in der Grundlagen erläutert und die verschiedenen Aspekte dieser Studie zueinander in Bezug gesetzt werden. Die weiteren Teile umfassen meine bereits publizierten oder zur Publikation eingereichten Arbeiten. Drei der abgedruckten Manuskripte sind überarbeitete Versionen bereits veröffentlichter Artikel. Die in diesen Artikeln angegebenen Quellen wurden aktualisiert und die *Abstracts* gemäß der von *Astronomy & Astrophysics* neu eingeführten Struktur angepasst. Das Manuskript des zuerst erschienenen Artikels wurde auf den Stand der späteren Arbeiten gebracht, denen Spektren mit genauerer Vakuumkorrektur und ein Dekompositionsalgorithmus mit besserer Fehlerabschätzung zu Grunde liegen. Zudem wurde für das generische interstellare Strahlungsfeld eine spektrale Form gewählt, die durch einen einfachen analytischen Ausdruck definiert ist (Draine & Bertoldi 1996, ApJ, 468, 269). Diese Form der Energiedichte ist in Cloudy implementiert und bei Vergleichsrechnungen von Vorteil. Die zuletzt abgedruckte Publikation ist ein Konferenzbeitrag zum *22nd Texas Symposium for Relativistic Astrophysics at Stanford University*.

Danksagungen

Herzlicher Dank gilt Prof. Dr. Dieter Reimers und Dr. Robert Baade für ihre stets freundliche und kompetente Unterstützung meiner Arbeit. Dankend erwähnen möchte ich auch alle anderen Mitarbeiter der Hamburger Sternwarte und den externen Gutachter Prof. Dr. Lutz Wisotzki.

Synopsis

ZUSAMMENFASSUNG

Es werden Grundlagen der Themen Kosmologie, Quasarabsorptionslinien, gedämpfte Ly α Systeme und Veränderlichkeit der Feinstrukturkonstanten erläutert. Bezüge zu den auf diesen Text folgenden Artikeln werden betont.

1. Kosmologie

1.1. Geometrie

Die Grundlage der theoretischen Beschreibung des Weltalls bildet Einsteins Theorie der Allgemeinen Relativität, welche die Raumzeit mit einer differenzierbaren Mannigfaltigkeit M identifiziert auf der eine Lorentz-Metrik g_{ab} definiert ist. Die Krümmung dieser Metrik, G_{ab}, verhält sich zu der Verteilung von Energie und Impuls, T_{ab}, gemäß der Einstein-Gleichung (in abstrakter Indexnotation, lateinische Indizes kennzeichnen lediglich Stufe und Typ eines Tensors)

$$G_{ab} + \Lambda g_{ab} = \frac{8\pi G}{c^4} T_{ab}. \tag{1}$$

Der Faktor Λ bezeichnet die kosmologische Konstante. Die Dimension dieser Konstanten ist diejenige einer Krümmung. Unter der Annahme einer in jedem Punkt isotropen Raumzeit reduziert sich die Metrik g_{ab} auf eine Summe zweier orthogonaler Terme

$$g_{ab} = -u_a u_b + h_{ab}(t), \tag{2}$$

wobei $h_{ab}(t)$ für jedes t einer Riemann-Metrik mit konstanter Krümmung K entspricht (z.B. Wald 1984). Drei Fälle sind zu unterscheiden: Für $K > 0$ entspricht $h_{ab}(t)$ der Metrik einer in den vierdimensionalen euklidischen Raum eingebetteten 3-Sphäre, für $K = 0$ der Metrik des dreidimensionalen euklidischen Raums, und für $K < 0$ der Metrik eines in den vierdimensionalen Minkowski-Raum eingebetteten 3-Hyperboloids. In synchron bewegten Koordinaten (Abb. 1) nimmt die Metrik g_{ab} Robertson-Walker Form an

$$\mathrm{d}s^2 = -c^2\mathrm{d}t^2 + R^2(t)\left[\frac{\mathrm{d}r^2}{1-kr^2} + r^2(\mathrm{d}\theta^2 + \sin^2(\theta)\mathrm{d}\phi^2)\right], \tag{3}$$

wobei $k = \mathrm{sgn}(K)$ die Signatur der räumlichen Krümmung wiedergibt (Abb. 2). Die Flächen konstanter Koordinaten (t, r) beschreiben raumartige 2-Sphären mit Krümmungsradius $R(t)r$. Die Koordinaten (θ, ϕ) entsprechen Standardwinkelkoordinaten auf diesen Sphären.

1.2. Dynamik

Durch die sowohl theoretisch als auch empirisch fundierte Annahme der Isotropie (Barrow 1995) ist die Metrik der Raumzeit bis auf die Signatur der räumlichen Krümmung und eine positiv definite Funktion R fixiert. Zudem entspricht der Energie-Impuls-Tensor demjenigen einer idealen Flüssigkeit mit Massendichte ρ und Druck p,

$$T_{ab} = \rho c^2 u_a u_b + p h_{ab}. \tag{4}$$

Einsetzen dieses Ausdrucks und der Robertson-Walker-Metrik in Gl. (1) ergibt die Friedmann-Gleichungen

$$3\frac{\dot{R}^2}{R^2} - \Lambda c^2 + 3\frac{kc^2}{R^2} = 8\pi G\rho, \tag{5}$$

$$-2\frac{\ddot{R}}{R} - \frac{\dot{R}^2}{R^2} + \Lambda c^2 - \frac{kc^2}{R^2} = 8\pi G\frac{p}{c^2}, \tag{6}$$

wobei ein Punkt über einer Größe deren zeitliche Ableitung bezeichnet. Unter Benutzung der ersten Gleichung, kann die zweite auch geschrieben werden als

$$3\frac{\ddot{R}}{R} - \Lambda c^2 = -4\pi G\left(\rho + 3\frac{p}{c^2}\right). \tag{7}$$

Multiplizieren von Gl. (5) mit R^2, Ableiten der resultierenden Gleichung nach t und Eliminieren von $\ddot{R}$ mittels (7) ergibt

$$\dot{\rho} + 3\left(\rho + \frac{p}{c^2}\right)\frac{\dot{R}}{R} = 0. \tag{8}$$

1.2.1. Drucklose Materie

Sowohl für baryonische Materie als auch für *cold dark matter* (CDM) dominiert die Massendichte den Druckterm, und Gl. (8) führt auf die Massenerhaltung

$$\frac{\mathrm{d}}{\mathrm{d}t}(\rho R^3) = 0. \tag{9}$$

Einsetzen der kosmologischen Parameter

$$H = \frac{\dot{R}}{R}, \tag{10}$$

$$\Omega = \frac{8\pi G\rho}{3H^2}, \tag{11}$$

$$\lambda = \frac{\Lambda c^2}{3H^2} \tag{12}$$

in die erste Friedmann-Gleichung ergibt unmittelbar

$$kc^2 = H^2R^2(\Omega + \lambda - 1). \tag{13}$$

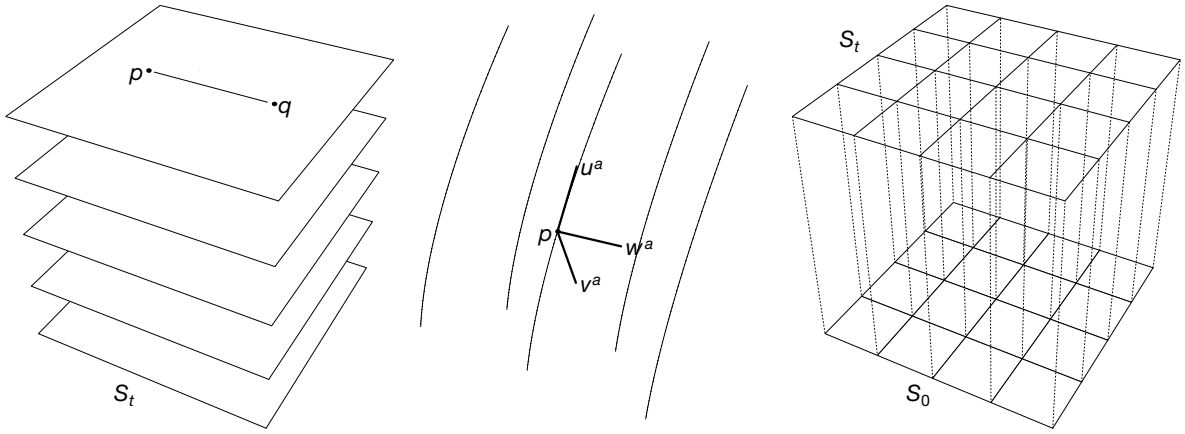

Abb. 1. *Räumliche Homogenität:* Zu jedem t und zu jedem Paar von Punkten $p, q \in S_t$ gibt es eine Isometrie, die p auf q abbildet. *Isotropie*: Es gibt eine Kongruenz zeitartiger Kurven (anschaulich als Weltlinien fundamentaler Beobachter zu beschreiben) mit Tangentenvektoren $u^a \in M$, so dass zu jedem Punkt $p \in M$ und zu jedem Paar von Vektoren $v^a, w^a \perp u^a$ eine Isometrie existiert die p und u^a bei p respektiert und v^a auf w^a abbildet. *Synchron bewegte Koordinaten:* Ein auf einer beliebigen Hyperfläche S_0 einmal eingeführtes Koordinatensystem kann entlang der Weltlinien fundamentaler Beobachter auf jede andere Hyperfläche S_t verschoben werden. Ohne Beschränkung der Allgemeinheit kann der Parameter t mit der Bogenlänge dieser Weltlinien (der Eigenzeit der fundamentalen Beobachter) identifiziert werden. Die Rotationsfreiheit des Vektorfelds u^a garantiert die Übereinstimmung aller von den fundamentalen Beobachtern auf ihrem Weg zwischen zwei beliebigen Hyperflächen erfahrenen Eigenzeitdifferenzen

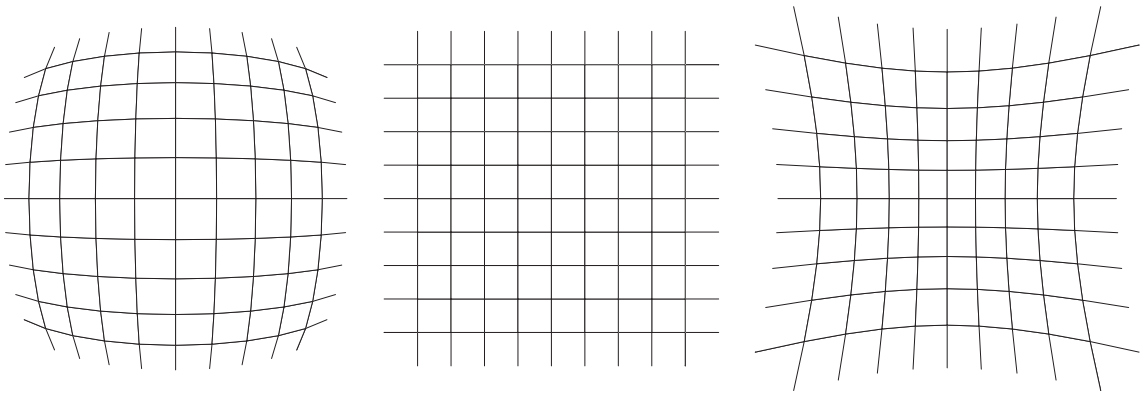

Abb. 2. Raumkrümmungen positiver, verschwindender und negativer Signatur. Ursprünglich parallele Geodäten laufen entweder zusammen, nebeneinander, oder auseinander

Werden die heutigen Werte dieser Parameter mit dem Index ‚0' gekennzeichnet, kann Gl. (5) mit Hilfe von (9)–(13) in eine Form überführt werden, die nach Einführen der kosmologischen Rotverschiebung

$$z = \frac{R_0}{R} - 1 \tag{14}$$

und der Notation

$$P(z) = \Omega_0(1+z)^3 - (\Omega_0 + \lambda_0 - 1)(1+z)^2 + \lambda_0 \tag{15}$$

nur noch beobachtbare Größen enthält,

$$\dot{z}^2 = H_0^2(1+z)^2 P(z). \tag{16}$$

Gleichung (16) stellt die Grundgleichung für die Interpretation kosmologischer Beobachtungen dar. Beispielsweise ist die Lichtlaufzeit zwischen zwei Ereignissen mit Rotverschiebungen $x < y$ gleich dem Integral über den Kehrwert der zeitlichen Ableitung der Rotverschiebung,

$$t_{xy} = H_0^{-1} \int_x^y (1+z)^{-1} P(z)^{-1/2}\, \mathrm{d}z. \tag{17}$$

Die theoretische Interpretation aller räumlichen Entfernungsmaße basiert auf der Eigenentfernung (im Englischen oft als *comoving distance* bezeichnet)

$$l_{xy} = cH_0^{-1} \int_x^y P(z)^{-1/2}\, \mathrm{d}z, \tag{18}$$

die aber wie die Lichtlaufzeit keine Messgröße ist. Die Entfernung des in dieser Arbeit untersuchten Absorptionsliniensystems ist Abb. 3 zu entnehmen.

1.2.2. Strahlung

Im Gegensatzt zu baryonischer Materie oder CDM, kann für Strahlung der Druckterm in Gl. (8) nicht vernachlässigt werden. Einsetzen der Zustandsgleichung für Strahlung $p = \rho c^2/3$ führt auf

$$\frac{\mathrm{d}}{\mathrm{d}t}(\rho R^4) = 0. \tag{19}$$

Da die Strahlung innerhalb eines Volumenelements bei einer Expansion des Universums an der Umgebung Arbeit leistet,

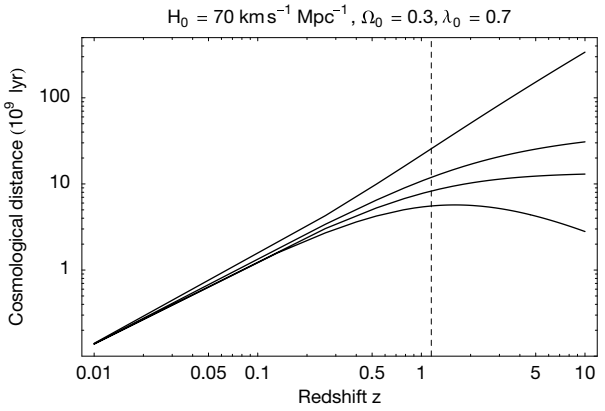

Abb. 3. Kosmologische Entfernungen basierend auf Leuchtkraft, Eigenbewegung, Lichtlaufzeit und Winkeldurchmesser (von oben nach unten; Carroll et al. 1992). Eigenentfernung und Eigenbewegungsentfernung sind für flache Weltmodelle identisch. Die angegebenen Werte der kosmologischen Parameter entsprechen den Ergebnissen des Sloan Digital Sky Survey und des Wilkinson Microwave Anisotropy Probe (Tegmark et al. 2004). Die Rotverschiebung des in dieser Arbeit untersuchten Absorptionsliniensystems ist markiert

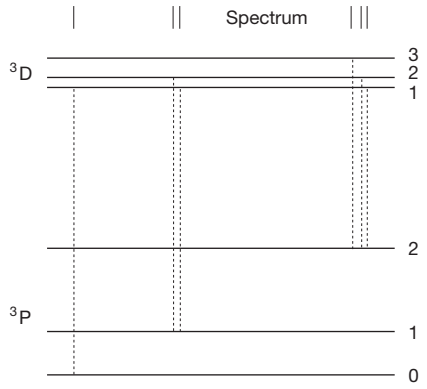

Abb. 4. Elektronenübergänge zwischen einem ^{3}P und einem ^{3}D Term, wie sie beispielsweise im Kohlenstoffatom stattfinden. Da die Besetzung der Grundzustandsniveaus $^3P_1$ und $^3P_2$ durch den kosmischen Mikrowellenhintergrund angeregt wird, ergibt die aus den Besetzungszahlen abgeleitete Temperatur eine obere Schranke für die Temperatur der Mikrowellenstrahlung. Ist der Mikrowellenhintergrund einzige Anregungsquelle, entsprechen Anregungs- und Strahlungstemperatur einander exakt

nimmt die Energiedichte stärker ab als der Volumenfaktor R^3 zunimmt. Unter Benutzung von Gl. (14) folgt aus Gl. (19)

$$\rho = (1+z)^4 \rho_0. \tag{20}$$

Für thermische Strahlung wie den kosmischen Mikrowellenhintergrund ist die Energiedichte proportional zur vierten Potenz der Temperatur, $\rho \propto T^4$, so dass obige Gleichung äquivalent ist zu

$$T = (1+z) T_0. \tag{21}$$

Da die Temperatur der kosmischen Hintergrundstrahlung für Rotverschiebungen $z > 0$ keine beobachtbare Größe ist, kann die Gültigkeit dieser Relation nur indirekt nachgewiesen werden (z.B. Bahcall 2000). Eine Methode besteht in der Analyse von Quasarabsorptionslinien, deren Grundzustand Feinstruktur aufweist (Bahcall & Wolf 1968). In dem ab Seite 18 abgedruckten Artikel wird die Anwendung dieser Methode auf Feinstrukturlinien des neutralen Kohlenstoffs (Abb. 4) beschrieben.

2. Quasarabsorptionslinien

Die Entdeckung des Quasars 3C 273 durch Maarten Schmidt (1963) war eine Sternstunde der Astronomie. Der einzelne Stern am Ende des bis dahin nur als diffuse Radioquelle bekannten Objekts 3C 273 zeigte im Optischen eine ungewöhnliche Helligkeit. Bei dem Versuch, ein Spektrum dieses Sterns aufzunehmen, wurde die erste Fotoplatte praktisch geröstet. Das Spektrum zeigte Emissionslinien die keiner bekannten Materieform entsprechen, ähnlich anderen damals als Radiosterne bezeichneten Objekten. Zu etwa gleicher Zeit erhielt Schmidt ein Manuskript von Jesse Greenstein über einen Radiostern mit der Bezeichnung 3C 48, dessen Geheimnis dieser glaubte entschlüsselt zu haben. 3C 48 sollte ein Zwergstern sein, dessen Schwermetalle Curium, Neptunium und Plutonium im Spektrum leuchteten. Ungläubig suchte Schmidt in den Spektrallinien von 3C 273 nach bekannten Mustern. Dabei entdeckte er, dass es sich bei den meisten Emissionslinien tatsächlich um rotverschobene Balmer-Linien handelte. Weitere Linien konnte er Magnesium und Sauerstoff zuordnen. Auch Greensteins Plutoniumstern zeigte im wesentlichen Balmer-Linien, allerdings mit einer höheren Rotverschiebung als 3C 273 (Greenstein & Schmidt 1964).

Die Entdeckung der extragalaktischen Natur der Quasare durch Maarten Schmidt (nachzulesen bei Preston 1996) leitete eine neue Ära der beobachtenden Kosmologie ein. Seitdem sind nicht nur Quasare und deren nähere Umgebung Gegenstand astronomischen Interesses, sondern auch die Materie im intergalaktischen Raum (Gunn & Peterson 1965; Bahcall & Salpeter 1965). Dieses Interesse kommt nicht von ungefähr, denn Quasarabsorptionslinien beinhalten wesentliche Informationen über die räumliche Struktur des Universums und die chemische Zusammensetzung und physikalischen Eigenschaften des absorbierenden Mediums.

2.1. Formale Beschreibung

Absorption ist definiert durch das Verhältnis von einfallender und transmittierter Strahlung. Die optische Tiefe einer Absorption wird beschrieben durch den Logarithmus dieses Verhältnisses

$$\tau(\lambda) = \log \frac{C(\lambda)}{F(\lambda)}. \tag{22}$$

Die Form einer Absorptionslinie wird bestimmt durch den Absorptionskoeffizienten des Mediums. Entspreche λ_{ij} der Wellenlänge des Übergangs eines Elektrons im Anfangszustand i in den Endzustand j, und sei n_i die Anzahldichte von Atomen mit Elektronen im Anfangszustand. Für ein homogenes Ensemble ruhender Teilchen ist der Absorptionskoeffizient gegeben durch eine Lorentz-Funktion

$$\kappa(\lambda) = \frac{e^2 n_i f_{ij} \lambda_{ij}^2}{4\pi\epsilon_0 mc^2} \frac{\gamma_{ij}}{(\lambda - \lambda_{ij})^2 + \gamma_{ij}^2}, \tag{23}$$

wobei f_{ij} die Oszillatorstärke der Linie und

$$\gamma_{ij} = \frac{\lambda_{ij}^2}{4\pi c}\left(\frac{1}{\tau_i} + \frac{1}{\tau_j}\right) \tag{24}$$

deren Dämpfungskoeffizienten bezeichnet. Für Resonanzabsorptionslinien ist dieser umgekehrt proportional zur Lebensdauer des Endzustands

$$\tau_j = \frac{1}{\sum_{k<j} A_{jk}}. \tag{25}$$

Für ein inhomogenes Ensemble sich bewegender Teilchen verbreitert sich die durch Gl. (23) beschriebene Linienform auf Grund des Doppler-Effekts gemäß

$$\kappa(\lambda) = \frac{e^2 f_{ij}\lambda_{ij}^2\gamma_{ij}}{4\pi\epsilon_0 mc^2}\int \frac{\frac{\partial n_i}{\partial v}(x,v)}{\left[\lambda - \lambda_{ij}\left(1+\frac{v}{c}\right)\right]^2 + \gamma_{ij}^2}\,\mathrm{d}v, \tag{26}$$

wobei v die zur Sichtlinie parallele Komponente des Geschwindigkeitsvektors bezeichnet. Für Teilchen der Masse M mit einer thermischen Geschwindigkeitsdispersion

$$\frac{\partial n}{\partial v}(x,v) = \frac{n(x)}{\sqrt{\pi}b}\,\mathrm{e}^{-v^2/b^2} \tag{27}$$

mit

$$b^2 = \frac{2kT}{M} \tag{28}$$

ist der Absorptionskoeffizient gegeben durch

$$\kappa(\lambda) = \frac{e^2}{4\epsilon_0 mc}\frac{n_i f_{ij}\lambda_{ij}}{b}\,H(a,u), \tag{29}$$

wobei

$$u = \frac{c}{b}\frac{\lambda-\lambda_{ij}}{\lambda_{ij}}, \qquad a = \frac{c}{b}\frac{\gamma_i}{\lambda_{ij}}. \tag{30}$$

Die Voigt-Funktion

$$H(a,u) = \frac{a}{\pi^{3/2}}\int \frac{\mathrm{e}^{-v^2}\,\mathrm{d}v}{(u-v)^2 + a^2} \tag{31}$$

ist allgemein als Faltung einer Lorentz- und einer Gauss-Funktion definiert. Mit

$$N_i = \int_l n_i(x)\,\mathrm{d}x \tag{32}$$

kann die optische Tiefe entlang der Sichtlinie $\tau(\lambda) = \int_l \kappa(\lambda)\,\mathrm{d}x$ geschrieben werden als

$$\tau(\lambda) = \frac{e^2}{4\epsilon_0 mc}\frac{N_i f_{ij}\lambda_{ij}}{b}\,H(a,u). \tag{33}$$

Im Limes $a \to 0$ wird

$$H(a,u) \to \frac{1}{\sqrt{\pi}}\,\mathrm{e}^{-u^2}, \tag{34}$$

so dass sich die optische Tiefe (33) auf den Doppler-Kern reduziert

$$\tau(\lambda) = \frac{e^2}{4\epsilon_0 mc}\frac{N_i f_{ij}\lambda_{ij}}{\sqrt{\pi}b}\exp\left[-\left(\frac{c}{b}\frac{\lambda-\lambda_{ij}}{\lambda_{ij}}\right)^2\right]. \tag{35}$$

Ensembles von Absorptionslinien werden durch Superposition mehrerer Komponenten beschrieben. Diese sind jedoch auf Grund der Verschmierung der Linien durch den Spektrographen für den Beobachter nicht von der Wirkung makroskopischer Geschwindigkeitsfelder $v(x)$ zu unterscheiden. Für deren Beschreibung ist das zweite Argument der Voigt-Funktion in Gl. (29) durch $u - v(x)/b$ zu ersetzen, so dass beispielsweise

$$\tau(\lambda) = \frac{e^2}{4\epsilon_0 mc}\frac{f_{ij}\lambda_{ij}}{\sqrt{\pi}b}\int_l n(x)\exp\left[-\left(\frac{c}{b}\frac{\lambda-\lambda_{ij}}{\lambda_{ij}} - \frac{v(x)}{b}\right)^2\right]\mathrm{d}x. \tag{36}$$

Die Wirkung mikroskopischer stochastischer Geschwindigkeitsfelder mit Varianz σ^2 kann mittels Gl. (27) beschrieben werden sofern

$$b^2 = \frac{2kT}{M} + 2\sigma^2. \tag{37}$$

Für die Beschreibung von Quasarabsorptionslinien ist in allen Ausdrücken für den Absorptionskoeffizienten und die optische Tiefe statt der beobachteten Wellenlänge λ die systemische Wellenlänge $\lambda/(1+z)$ zu verwenden.

2.2. Dekomposition

Die Geschichte über die Entdeckung der Quasare durch Maarten Schmidt zeigt ein erstes Problem, das sich bei der Analyse von Quasarabsorptionslinien stellt: die korrekte Identifikation der Spektrallinien. Da diese allesamt um einen a priori unbekannten Faktor rotverschoben sind, können nur die Verhältnisse der beobachteten Wellenlängen Auskunft über Art und Zugehörigkeit geben. Ein zweites Problem ist die korrekte Dekomposition von Spektrallinien in einzelne Komponenten: Durch die Faltung mit dem instrumentellen Profil des Spektrographen ergeben sich für Ensembles schmaler Linien keine eindeutigen Lösungen. Die gewöhnlich zur Dekomposition verwendeten deterministischen Optimierungsverfahren sind für diese Situation wenig geeignet, da oft nur lokal optimale Lösungen gefunden werden, die zudem stark von Anfangswertvorgaben abhängen. Diese Unzulänglichkeit gab Anlass, in dieser Dissertation statt der üblichen deterministischen Optimierungsverfahren, Evolutionsstrategien zu verwenden. Wie andere stochastische Verfahren, sind Evolutionsstrategien gegenüber Anfangswertvorgaben weniger empfindlich und zudem zuverlässiger bei der Suche nach einer global optimalen Lösung. Die Anwendung von Evolutionsstrategien auf die Dekomposition von Quasarspektren wird in dem ab Seite 9 abgedruckten Artikel im Detail beschrieben. Die Überlegenheit dieses Verfahrens gegenüber verschiedenen klassischen Methoden wird demonstriert.

3. Gedämpfte Ly α Systeme

Quasarabsorptionsliniensysteme mit einer Säulendichte von $N_{\rm H\,I} \geq 2 \times 10^{20}$ Wasserstoffatomen cm^{-2} werden als gedämpfte Ly α (DLA) Systeme bezeichnet.[1] Der Schwellwert von 2×10^{20} cm^{-2} entspricht dem historischen Detektionslimit der 21 cm Linie in Spiralgalaxien der näheren Umgebung, ist aber auch physikalisch relevant: Absorber oberhalb dieses Schwellwerts bestehen auch bei hohen Rotverschiebungen im wesentlichen aus vorwiegend neutralem Gas. Genau diese Eigenschaft macht DLA Systeme für die Forschung interessant, denn ein Reservoir von neutralem Gas ist eine Grundvoraussetzung für die Entstehung von Sternen. DLA Systeme bieten daher die beste Möglichkeit, die vermutlichen Äquivalente des interstellaren Mediums lokaler Galaxien in einem früheren Stadium der kosmischen Entwicklung zu studieren. Absorber im sub-DLA Bereich bis zu $N_{\rm H\,I} \geq 10^{19}$ cm^{-2} sind in der Regel teilweise ionisiert, können aber aus überwiegend neutralem Gas bestehen wenn der kosmische UV Hintergrund schwach ist (Dessauges-Zavadsky et al. 2003; Péroux et al. 2003; Peroux et al. 2006).

3.1. Physikalische Natur

Die physikalische Natur der DLA Systeme ist weitgehend ungeklärt. Klar ist lediglich, dass DLA Absorber eine heterogene Population von extragalaktischen H I Regionen bilden, die viele Ähnlichkeiten, aber auch Unterschiede zu dem interstellaren Medium lokaler Galaxien aufweist. Es gibt jedoch einige indirekte Hinweise auf die Natur der Absorber. Deneindeutigsten Hinweis stellt die im Vergleich zum intergalaktischen Medium um Größenordnungen höhere Metallizität dar, die ohne eine unmittelbare Verbindung zu Sternen und Galaxien nicht denkbar ist. Weitere Hinweise gibt die kinematische Struktur der assoziierten Metalllinien, die im Rahmen hierarchischer Galaxienentstehungsmodelle als Resultat rotierender, sich zufällig und aufeindanderzu bewegender und miteinander verschmelzender protogalaktischer Gasformationen begriffen werden kann (Haehnelt et al. 1998). Der Ausfluss von Materie auf Grund massiver Sternentstehung und induzierter galaktischer Winde stellt eine weitere Möglichkeit dar, die beobachteten Strukturen zu erklären (Nulsen et al. 1998; Schaye 2001). Die Übereinstimmung der statistischen Eigenschaften beobachteter DLA Systemen mit hydrodynamischen Simulationen kosmischer Strukturbildung zeigt an, dass die Absorptionslinien in kaltem Gas ansonsten heißer CDM Halos entstehen (Nagamine et al. 2004, siehe auch Abb. 5). Ein aufschlussreicher Indikator ist molekularer Wasserstoff, dessen geringe Menge oder Fehlen implizert, dass die Absorber in der Regel wärmeres Gas enthalten als das interstellare Medium der Milchstraße, diesbezüglich eher vergleichbar mit dem interstellaren Medium der Magellanschen Wolken (Petijean et al. 2000; Ledoux et al. 2003). Beispiele von Absorbern im Vordergrund von Doppelquasaren (Lopez et al. 2005) und vor allem die ab Seite 26 abgedruckte Studie des sub-DLA Systems in Richtung von HE 0515–4414 zeigen das DLA Absorber in ihrer chemischen

[1] Die Bezeichnung ist von der Tatsache abgeleitet, dass die Dämpfungsflügel der natürlichen Profilfunktion der Ly α Linie des Wasserstoffatoms optisch dick sind.

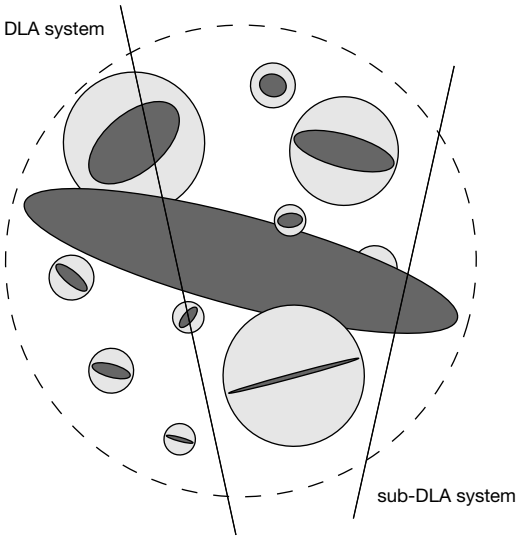

Abb. 5. Gas in semianalytischen Galaxienentstehungsmodellen (Maller et al. 2001, 2003). Die dunkelgrau gefüllten Ellipsen entsprechen neutralem Gas, während die hellgrau unterlegten Kreise heißes Gas in sphärischen Subhalos darstellen. Der gesamte CDM Halo (gestrichelte Linie) ist ebenfalls mit heißem Gas gefüllt. Zwei Sichtlinien illustieren die Entstehung von DLA und sub-DLA Systemen

Zusammensetzung nicht homogen sind. Die Seltenheit von molekularem Wasserstoff ist daher auch durch einen geringen Absorptionsquerschnitt molekularer Strukturen erklärbar. Direkte Identifikationen von DLA Absorbern mit Galaxien geben ein uneinheitliches Bild. Die Leuchtkräfte der identifizierten DLA Absorber mit Rotverschiebungen $z \geq 1.5$ sind mit denjenigen normaler Galaxien vergleichbar (Chen et al. 2005; Chen & Lanzetta 2003; Rao et al. 2003). Die wenigen identifizierten Absorber mit höheren Rotverschiebungen ähneln leuchtschwachen Starburst Galaxien (Moeller et al. 2002, 2004). Wenn DLA Absorber und Galaxien einander generell entsprechen, sind die beobachteten Eigenschaften überwiegend zufälliger Art, beispielsweise resultierend aus dem Impaktparameter der Sichtlinie und dem Inklinationswinkel und Typ der DLA Galaxie. Dennoch lassen einige Merkmale Evolution erkennen.

3.2. Evolution von neutralem Gas im Universum

Nahezu der gesamte Vorrat an neutralem Gas im Rotverschiebungsbereich $1.6 \leq z \leq 5.0$ ist in DLA Absorbern konzentriert (Lanzetta et al. 1995; Wolfe et al. 2005). Der Beitrag der in diesen Absorbern enthaltenen neutralen Gasmenge zur kosmologischen Massendichte Ω ist eine Beobachtungsgröße, deren Evolution einen wichtigen Prüfstein für die Bewertung kosmischer Strukturbildungsmodelle darstellt (Sommerville et al. 2001; Cen et al. 2003; Nagamine et al. 2004). Ausgangspunkt für den Vergleich zwischen Modell und Beobachtung ist die Verteilungsfunktion

$$f(N,z) = \frac{\partial^2 \mathcal{N}}{\partial N \partial z}(N,z) \tag{38}$$

wobei $\mathcal{N}(N,z)$ der Anzahl von Absorbern mit Wasserstoffsäulendichten kleiner als N und Rotverschiebungen kleiner als

z entspricht. Bezeichne $n(N, z)$ die mitbewegte Anzahldichte von Absorbern mit Wasserstoffsäulendichten kleiner als N, und sei $A(N, z)$ der geometrische Absorptionsquerschnitt eines Absorbers, dann kann $f(N, z)$ geschrieben werden als

$$f(N, z) = (1 + z)^2 A(N, z) \frac{\mathrm{d}l}{\mathrm{d}z}(z) \frac{\mathrm{d}n}{\mathrm{d}N}(N, z). \quad (39)$$

Der aus der Verwendung mitbewegter Größen resultierende Faktor $(1 + z)^2$ kann eliminiert werden mittels der Transformation

$$X = H_0 c^{-1} \int (1 + z)^2 \frac{\mathrm{d}l}{\mathrm{d}z}(z)\, \mathrm{d}z, \quad (40)$$

so dass

$$f(N, X) = c H_0^{-1} A(N, X) \frac{\mathrm{d}n}{\mathrm{d}N}(N, X). \quad (41)$$

Bezeichne m die Masse des Wasserstoffatoms, und sei μ das mittlere Molekulargewicht, dann kann die Masse eines Absorbers geschrieben werden als $M = \mu m N A(N, X)$. Die mitbewegte kosmische Massendichte daher aus

$$\rho_{\mathrm{ng}}(X) = H_0 c^{-1} \mu m \int f(N, X) N \, \mathrm{d}N. \quad (42)$$

Für eine vollständige Stichprobe von Absorbern in einem Intervall $[X - \delta, X + \delta]$ gilt die Relation

$$\rho_{\mathrm{ng}}(X) = H_0 c^{-1} \mu m \frac{\sum_i N_i}{2\delta}. \quad (43)$$

Eine auf mehr als 600 DLA Systemen basierende aktuelle Studie zeigt, dass Gl. (43) konvergiert und ρ_{ng} einer Evolution unterliegt (Prochaska et al. 2005). Beispielsweise fällt

$$\Omega_{\mathrm{ng}} = \frac{8\pi G \rho_{\mathrm{ng}}}{3 H_0^2} \quad (44)$$

von 1.0×10^{-3} bei $z \geq 3.5$ auf 0.5×10^{-3} bei $z = 2.5$. Bei $z \geq 3.5$ ist Ω_{ng} um einen Faktor 10 größer als der heutige Beitrag irregulärer Zwerggalaxien zu Ω_0, was einer generellen Evolution von DLA Absorbern in Objekte diesen Typs widerspricht. Interessanterweise ist Ω_{ng} bei $z \geq 3.5$ um einen Faktor 2–3 kleiner als der heutige stellare Beitrag zu Ω_0, was indirekt ein stetiges Nachfüllen des Reservoirs an neutralem Gas impliziert. Besondere Bedeutung hat diese Implikation für Strukturbildungsmodelle. Direkte Anzeichen für die Akkretion intergalaktischer Materie durch DLA Systeme wurden noch nicht beobachtet.

Alle empirischen Methoden zur Bestimmung der Funktion $f(N, X)$ unterliegen Auswahleffekten. Ein unbekannter Effekt ist insbesondere die durch einen hohen Anteil von Staub in DLA Absorbern verursachte Extinktion der Quasare im Hintergrund (Fall & Pei 1993). In dem ab Seite 58 abgedruckten Konferenzbeitrag bildet dieser Aspekt einen Schwerpunkt.

3.3. Evolution der kosmischen Metallizität

Eine ebenso wie Ω_{ng} unmittelbar empirische Größe ist die kosmische Metallizität $\langle Z \rangle$, welche definiert ist als Logarithmus des Verhältnisses der kosmischen Dichten von Metallen und neutralem Gas relativ zum solaren Wert,

$$\langle Z \rangle = \log \frac{\sum_i 10^{[Y/\mathrm{H}]} N_i}{\sum_i N_i}, \quad (45)$$

wobei Y das als Metallizitätsindikator verwendete Element bezeichnet. Basierend auf mehr als 120 DLA Systemen, zeigen aktuelle Arbeiten einen leichten Anstieg der kosmischen Metallizität von $\langle Z \rangle = -1.5 \pm 0.3$ bei $z \geq 3.5$ zu $\langle Z \rangle = -0.8 \pm 0.3$ bei $z \leq 1.5$ (Prochaska et al. 2003; Kulkarni et al. 2005; Rao et al. 2005; Wolfe et al. 2005). Der heterogenen Herkunft der DLA Systeme entsprechend, streut die Metallizität um etwa eine Größenordnung, unabhängig von der Rotverschiebung. Die im Vergleich zu lokalen Galaxien relativ geringe Metallizität der Absorber bei $z \leq 1.5$ wird als *missing metals* Problem bezeichnet (Prochaska et al. 2003). Die Anzahl der bekannten DLA Absorber bei $z \leq 1.5$ ist jedoch relativ gering. Die kosmische Metallizität in diesem Bereich ist unsicher, zumal auf Grund des reduzierten UV Hintergrunds signifikante Beiträge von Absorbern im sub-DLA Bereich möglich sind. In der Tat entspricht das System mit der bisher höchsten beobachteten Metallizität einem sub-DLA Absorber (Peroux et al. 2006). Ionisationseffekte und Staubkondensation erschweren die Messungen wesentlich (Dessauges-Zavadsky et al. 2006). Insbesondere Staubkondensation wird mit zunehmender Metallizität immer wahrscheinlicher, so dass neben einem geringen Absorptionsquerschnitt der interstellaren Regionen mit der höchsten Metallizität, auch Auswahleffekte als Verursacher des *missing metals* Problems infrage kommen (Vladilo 2004; Vladilo & Péroux 2005).

3.4. Ungelöste Probleme

Das über allen aktuellen Untersuchungen schwebende Problem ist die Aufklärung der trotz vieler Einsichten immer noch unbekannten physikalischen Natur der DLA Absorber. Da diese Objekte vielfältigen Ursprungs sind, können die statistischen Eigenschaften der gesamten Population generelle Hinweise geben. Im Einzelfall sind diese jedoch nicht ausreichend. Insbesondere bei Absorbern deren Eigenschaften stark vom Mittel abweichen ist ohne detallierte Einzelanalysen kein Erkenntnisgewinn zu erwarten.

Die Untersuchung der Eigenschaften des interstallaren Mediums in DLA Systemen steht erst am Anfang. Spektren hoher Qualität werden benötigt, um beispielsweise die Existenz kühler Phasen molekularen Gases nachzuweisen. Ebenso fehlen direkte Nachweise für aktive Sternentstehung oder die Akkretion von Materie aus dem intergalaktischen Mediums. Neben Akkretion ist auch der umgekehrte Vorgang – der Ausstoß metallhaltigen Materials in das umgebende Medium – denkbar. Der Nachweis eines derartigen Feedbacks würde sowohl zur Lösung des *missing metals* Problems als auch zum besseren Verständnis der Wechselwirkungen zwischen DLA Absorbern und dem intergalaktischen Medium beitragen. Eine der brennendsten Fragen ist die nach Auswahleffekten im Zusammenhang mit Staubkondensation, deren Wirkung teilweise kontrovers diskutiert wird (Murphy & Liske 2004; Vladilo & Péroux 2005; Smette et al. 2005). Die ab Seite 26 abgedruckte Arbeit

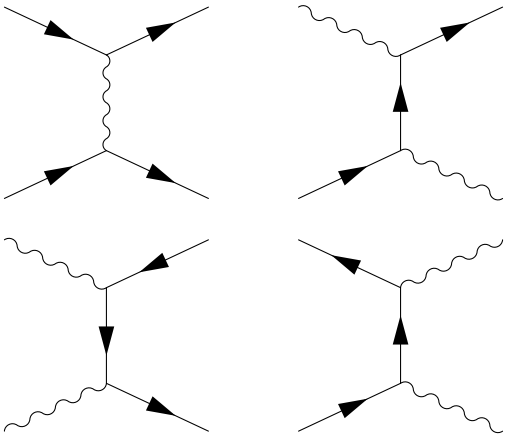

Abb. 6. Beispiele für quantenelektrodynamische Prozesse: Elektron-Elektron-Streuung, Compton-Streuung, Paarerzeugung und Paarvernichtung. Jeder Vertex trägt einen Faktor $\alpha^{1/2}$ zur Amplitude bei

über das sub-DLA System in Richtung HE 0515–4414 legt den Schwerpunkt auf die Untersuchung der Eigenschaften des absorbierenden Mediums. Ionisationseffekte und Staubkondensation werden detailliert behandelt.

4. Veränderlichkeit der Feinstrukturkonstanten

Die unmittelbare Entsprechung von Spektrallinien und atomaren Energieniveaus ermöglicht, mit der Überprüfung physikalischer Gesetze und Theorien in kosmologische Entfernungen vorzudringen. Insbesondere können Quasarabsorptionslinien genutzt werden, um die von vielen gegenwärtig diskutierten Theorien zur Vereinigung aller Wechselwirkungen geforderte Veränderlichkeit der Feinstrukturkonstanten

$$\alpha = \frac{e^2}{4\pi\epsilon_0\hbar c} \tag{46}$$

zu untersuchen (Bahcall et al. 1967; Webb et al. 1999, 2001). Da die Feinstrukturkonstante eng mit der Kopplungskonstanten der Quantenelektrodynamik verknüpft ist, hat eine Veränderung der Feinsturktur Auswirkungen auf alle elektromagnetischen Effekte (Abb. 6). Die Auswirkungen auf atomare Energieniveaus werden durch relativistische Quantenmechanik und Vielteilchen-Störungstheorie quantifiziert.

4.1. Atomare Feinstruktur

Der nichtrelativistische Hamiltonoperator für ein Elektron im elektrostatischen Potential eines Atomkerns mit Kernladungszahl Z ist gegeben durch

$$H = \frac{|\boldsymbol{P}|^2}{2m} - \hbar c\frac{Z\alpha}{r}. \tag{47}$$

Die Eigenwerte dieses Operators

$$E_n = -mc^2\frac{(Z\alpha)^2}{2n^2} \tag{48}$$

sind mit der Multiplizität $2n^2$ entartet, da sie nicht von den Quantenzahlen für den Bahndrehimpuls und Spin des Elektrons abhängen. Durch die relativistische Behandlung des Elektrons wird diese Entartung teilweise aufgehoben, denn die Dirac-Gleichung liefert Eigenwerte, die neben der Hauptquantenzahl n auch von der Quantenzahl j für den Gesamtdrehimpuls des Elektrons abhängen

$$E_{n,j} = \frac{mc^2}{\sqrt{1+\left(\dfrac{Z\alpha}{n-j-\frac{1}{2}+\sqrt{\left(j+\frac{1}{2}\right)^2-\alpha^2}}\right)^2}}. \tag{49}$$

Die Entwicklung dieses Ausdrucks in eine Potenzreihe von $Z\alpha$ ergibt eine einfach zu interpretierende Form

$$E_{n,j} = mc^2\left[1-\frac{(Z\alpha)^2}{2n^2}-\frac{(Z\alpha)^4}{2n^4}\left(\frac{n}{j+\frac{1}{2}}-\frac{3}{4}\right)+\cdots\right]. \tag{50}$$

Das erste Glied dieser Reihe entspricht der Ruhemasse des Elektrons, das zweite Glied dem nichtrelativistischen Eigenwert (48), und nur das dritte Glied beinhaltet die relativistische Korrektur. Unter Verwendung von Gl. (48) kann diese auch geschrieben werden als

$$\Delta_{n,j} = \frac{E_n}{n}(Z\alpha)^2\left(\frac{1}{j+\frac{1}{2}}-\frac{3}{4n}\right). \tag{51}$$

Reihenglieder höherer Ordnung sind nicht relevant gegenüber Effekten, die in der Dirac-Gleichung keine Berücksichtigung finden, wie Hyperfeinstruktur und höhere quantenelektrodynamische Beiträge. Für den allgemeineren Fall eines Atoms mit einem Valenzelektron hat die relativistische Korrektur die Form

$$\Delta_{n,l,j} = \frac{E_n}{\nu}(Z\alpha)^2\left(\frac{1}{j+\frac{1}{2}}-C(Z,l,j)\right), \tag{52}$$

wobei ν einer durch Ladungsabschirmung definierten effektiven Hauptquantenzahl entspricht und $C(Z,l,j)$ relativistische Vielteilcheneffekte beinhaltet (Dzuba et al. 1999). Letztere sind für verschiedene Atome und Partialwellen unterschiedlich.

4.2. Messung

Vollständige Vielteilchen-Dirac-Hartree-Fock Rechungen ergeben für die Vakuumwellenlängen λ_i der betrachteten Elektronenübergänge eine Parametrisierung der Form

$$\frac{1}{\lambda_i} = \frac{1}{\lambda_{0,i}} + q_i x(x+2), \tag{53}$$

wobei $\lambda_{0,i}$ die im Labor gemessene Wellenlänge und $x = \Delta\alpha/\alpha$ die relative Änderung der Feinstrukturkonstanten gegenüber ihrem heutigen Wert bezeichnen (Dzuba et al. 2002). Der Korrekturkoeffizient q_i ist für viele der in Quasarspektren gewöhnlich beobachteten Resonanzlinien tabelliert (Dzuba et al. 2002; Kozlov et al. 2004). Da die Wellenlängen verschiedener Elektronenübergänge unterschiedlich stark von Änderungen der Feinsturkturkonstanten abhängen, sind Abweichungen dieser Konstanten von ihrem heutigen Wert im Prinzip messbar. In der ab Seite 51 abgedruckten Arbeit wird die Änderung der Feinstukturkonstanten mittels verschiedener Fe II Linien untersucht (Abb. 7).

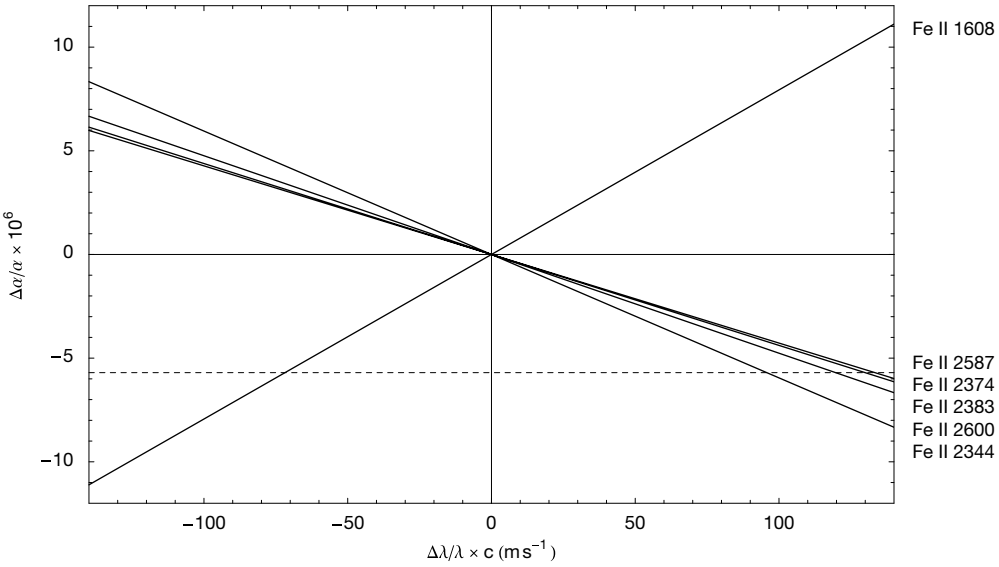

Abb. 7. Wellenlängenabhängigkeit verschiedener Fe II Linien. Die von Murphy et al. (2003, 2004) gefundene Variation (gestrichelte Linie) würde ein Anwachsen der Linienabstände um etwa 200 m s^{-1} bewirken

Literatur

Bahcall, J. N. 2000, Nature, 408, 916
Bahcall, J. N. & Salpeter, E. E. 1965, ApJ, 142, 1677
Bahcall, J. N. & Wolf, R. A. 1968, ApJ, 152, 701
Bahcall, J. N., Sargent, W. L. W., & Schmidt, M. 1967, ApJ, 149, L11
Barrow, J. D. 1995, Phys. Rev. D, 51, 3113
Carroll, S. M., Press, W. H., & Turner, E. L. 1992, ARA&A, 30, 499
Cen, R., Ostriker, J. P., Prochaska, J. X., & Wolfe, A. M. 2003, ApJ, 598, 741
Chen, H. & Lanzetta, K. M. 2003, ApJ, 597, 706
Chen, H., Kennicut, R. C., & Rauch, M. 2005, ApJ, 403, 55
Dessauges-Zavadsky, M., Péroux, C., Kim, T.-S., D'Odorico, S., & McMahon, R. G. 2003, MNRAS, 345, 447
Dessauges-Zavadsky, M., Prochaska, J. X., D'Odorico, S., Calura, F., & Matteucci, F. 2006, A&A, 445, 93
Dzuba, V. A., Flambaum, V. V., & Webb, J. K. 1999, Phys. Rev. A, 59, 230
Dzuba, V. A., Flambaum, V. V., Kozlov, M. G., & Marchenko, M. 2002, Phys. Rev. A, 66, 022501
Fall, S. M. & Pei, Y. C. 1993, ApJ, 402, 479
Greenstein, J. L. & Schmidt, M. 1964, ApJ, 140, 1
Gunn, J. E. & Peterson, B. A. 1965, ApJ, 142, 1633
Haehnelt, M. G., Steinmetz, M., & Rauch, M. 1998, ApJ, 495, 647
Kozlov, M. G., Karol, V. A., Berengut, J. C., Dzuba, V. A., & Flambaum, V. V. 2004, Phys. Rev. A, 70, 0621108
Kulkarni, V. P., Fall, S. M., Lauroesch, J. T., et al. 2005, ApJ, 618, 68
Lanzetta, K. M., Wolfe, A. M., & Turnshek, D. A. 1995, ApJ, 440, 435
Ledoux, C., Petijean, P., & Srianand, R. 2003, MNRAS, 346, 209
Lopez, S., Reimers, D., Gregg, M. D., et al. 2005, ApJ, 626, 767
Maller, A. H., Prochaska, J. X., Sommerville, R. S., & Primack, J. R. 2001, MNRAS, 326, 1475
Maller, A. H., Prochaska, J. X., Sommerville, R. S., & Primack, J. R. 2003, MNRAS, 343, 268
Moeller, P., Warren, S. J., Fall, S. M., Fynbo, J. U., & Jakobsen, P. 2002, ApJ, 574, 51
Moeller, P., Fynbo, J. P. U., & Fall, S. M. 2004, A&A, 422, L33
Murphy, M. T. & Liske, J. 2004, MNRAS, 354
Murphy, M. T., Webb, J. K., & Flambaum, V. V. 2003, MNRAS, 345, 609
Murphy, M. T., Flambaum, V. V., Webb, J. K., et al. 2004, Lect. Not. Phys., 648, 131
Nagamine, K., Springel, V., & Hernquist, L. 2004, MNRAS, 348, 421
Nulsen, P. E. J., Barcons, X., & Fabian, A. C. 1998, MNRAS, 301, 168
Péroux, C., Dessauges-Zavadsky, M., D'Odorico, S., Kim, T.-S., & McMahon, R. G. 2003, MNRAS, 345, 480
Peroux, C., Kulkarni, V. P., Meiring, J., et al. 2006, A&A, im Druck
Petijean, P., Srianand, R., & Ledoux, C. 2000, A&A, 364, L26
Preston, R. 1996, First Light. The Search for the Edge of the Universe (Random House)
Prochaska, J. X., Gawiser, E., Wolfe, A. M., Castro, S., & Djorgovski, S. G. 2003, ApJ, 595, L9
Prochaska, J. X., Herbert-Fort, S., & Wolfe, A. M. 2005, ApJ, 635, 123
Rao, S. M., Nestor, D. B., Turnshek, D. A., et al. 2003, ApJ, 595, 94
Rao, S. M., Prochaska, J. X., Howk, J. C., & Wolfe, A. M. 2005, AJ, 129, 9
Schaye, J. 2001, ApJ, 559, L1
Schmidt, M. 1963, Nature, 197, 1040
Smette, A., Wisotzki, L., Ledoux, C., et al. 2005, in Proc. IAU, Vol. 1, Probing Galaxies through Quasar Absorption Lines, 475–477
Sommerville, R. S., Primack, J. R., & Faber, S. M. 2001, MNRAS, 320, 504
Tegmark, M., Strauss, M. A., Blanton, M. R., et al. 2004, Phys. Rev. D, 69, 103501
Vladilo, G. 2004, A&A, 421, 479
Vladilo, G. & Péroux, C. 2005, A&A, 444, 461
Wald, R. M. 1984, General Relativity (University of Chicago Press)
Webb, J. K., Flambaum, V. V., Churchill, C. W., Drinkwater, M. J., & Barrow, J. D. 1999, Phys. Rev. Lett., 82, 884
Webb, J. K., Murphy, M. T., Flambaum, V. V., et al. 2001, Phys. Rev. Lett., 87, 091301
Wolfe, A. M., Gawiser, E., & Prochaska, J. X. 2005, ARA&A, 43, 861

Revised manuscript. The original version was published in A&A 431, 1167–1175 (2005)

Evolution strategies applied to the problem of line profile decomposition in QSO spectra

R. Quast, R. Baade, and D. Reimers

Hamburger Sternwarte, Universität Hamburg, Gojenbergsweg 112, D-21029 Hamburg, Germany
e-mail: {rquast,rbaade,dreimers}@hs.uni-hamburg.de

Received 6 July 2004 / Accepted 21 October 2004 / Revised 6 December 2005

ABSTRACT

Aims. We test the decomposition of QSO absorption line ensembles by means of evolutionary forward modelling. The modelling is optimized using an evolution strategy based on a novel concept of completely derandomized self-adaption. The algorithm is described in detail.
Methods. The global optimization performance of the evolution strategy in decomposing a series of simulated test spectra is compared to that of classical deterministic algorithms.
Results. Evolutionary forward modelling is a highly competitive technique capable of calculating the optimal decomposition without requiring any particular initialization.

Key words. methods: data analysis – methods: numerical – quasars: absorption lines

1. Introduction

The standard astronomical data analysis packages such as the Image Reduction and Analysis Facility (IRAF) and many popular custom-built applications offer only deterministic algorithms for the purpose of parametric model fitting. In practice, however, deterministic algorithms often require considerable operational intervention by the user. In contrast, stochastic strategies such as evolutionary algorithms minimize the operational interaction, a highly appealing feature.

Any parametric model-fitting technique reduces to the purely numerical problem of finding the minimum of an objective function $f : \mathbb{R}^n \to \mathbb{R}$, i.e. constructing a sequence of object parameter vectors

$$(\boldsymbol{x}^{(g)})_{g\in\mathbb{N}}, \quad \boldsymbol{x}^{(g)} \in \mathbb{R}^n \tag{1}$$

such that $\lim_{g\to\infty} f(\boldsymbol{x}^{(g)})$ is as small as possible. Several classical algorithms are suitable for overcoming the problem of minimization. Among the best established strategies are the conjugate gradient, variable metric and Levenberg-Marquardt algorithms, which all collect information about the local topography of f by calculating its partial derivatives (i.e. the gradient or the Hessian matrix) and thereby ensure the rapid convergence to a nearby minimum (e.g., Press et al. 2002, Numerical Recipes). The nature of these classical algorithms is deterministic: each member of the sequence $(\boldsymbol{x}^{(g)})_g$ is determined by its predecessor, i.e. the whole sequence is determined by the intial object parameter vector $\boldsymbol{x}^{(0)}$. Exactly this turns out to be the cardinal deficiency when f exhibits many local minima: The success of the algorithms in locating the global minimum of f depends crucially on the adequacy of the initial guess $\boldsymbol{x}^{(0)}$. Hence, the results are biased and several optimization runs are normally necessary. In particular in case of noisy data or strong inter-parameter correlations the problem of finding an adequate initialization $\boldsymbol{x}^{(0)}$ is tedious and often dominates the time needed to complete the optimization. In addition, the classical algorithms are not practicable if the objective function is not continuously differentiable, oscillating, or if the calculation of partial derivatives is too expensive or numerically inaccurate.

In contrast, stochastic strategies such as simulated annealing and evolutionary algorithms where each member of the sequence $(\boldsymbol{x}^{(g)})_g$ is the result of a random experiment, are not only promising for the purpose of global optimization but also apply to any objective function which is computable or available by experiment. However, the obligatory drawback of stochastic optimization strategies is lower efficiency: even if an adequate local downhill move exists, a random step will almost always lead astray. Therefore, many more evaluations of the objective function are required before the sequence $(\boldsymbol{x}^{(g)})_g$ converges to a minimum.

Evolutionary algorithms are inspired by the principles of biological evolution. Conceptually, three major subclasses are discerned: evolutionary programming, genetic algorithms, and evolution strategies (ES). While all subclasses apply quite generally, ES are particularly suited for the purpose of continu-

Send offprint requests to: R. Quast

ous parametric optimization. Recently, Hansen & Ostermeier (2001, hereafter Paper A) and Hansen et al. (2003, hereafter Paper B) have established a novel concept of completely derandomized self-adaption in ES which selectively approximates the inverse Hessian matrix of the objective function and thereby considerably improves the efficiency in case of non-separable problems or mis-scaled parameter mappings while even increasing the chance of finding the global optimum in case of strong multimodality.

The interpretation and analysis of QSO absorption lines basically involves the decomposition of line ensembles into individual line profiles. In general, the decomposition of QSO spectra presents an ambigous parametric inverse problem, and automatizing the decomposition requires an efficient but at first stable optimization algorithm. In this study we summarize the concept of completely derandomized self-adaption introduced in Paper A and test the global optimization performance of the resulting ES when applied to the problem of line profile decomposition in QSO spectra.

2. Evolution strategies (ES)

2.1. General concepts

The state of an ES in generation g is defined by the parental family of object parameter vectors $\boldsymbol{x}_1^{(g)}, \ldots, \boldsymbol{x}_{\mu\in\mathbb{N}}^{(g)} \in \mathbb{R}^n$ and the mutation operator $p^{(g)} : \mathbb{R}^n \to \mathbb{R}^n$. The generic ES algorithm is completely defined by the transition from generation g to $g+1$. For instance, in the illustrative case of a simple single parent strategy:

1. Mutation of the parental vector $\boldsymbol{x}^{(g)}$ to produce a new population of $\lambda > 1$ offspring
$$\boldsymbol{y}_1^{(g+1)}, \ldots, \boldsymbol{y}_\lambda^{(g+1)} \in \mathbb{R}^n \quad \leftarrow \quad p^{(g)}\boldsymbol{x}^{(g)} = N(\boldsymbol{x}^{(g)}, \sigma^2\boldsymbol{I}), \quad (2)$$
where each offspring is sampled from an n-dimensional normal mutation distribution with mean $\boldsymbol{x}^{(g)}$ and isotropic variance σ^2.
2. Selection of the best individual among the offspring population to become the new parental vector
$$\boldsymbol{x}^{(g+1)} = \boldsymbol{y}_{1:\lambda}^{(g+1)}, \quad (3)$$
where the notation $\boldsymbol{y}_{i:\lambda}$ refers to the i^{th} best among $\boldsymbol{y}_1, \ldots, \boldsymbol{y}_\lambda$ individuals, and $\boldsymbol{y}_i$ is better than $\boldsymbol{y}_j$ if $f(\boldsymbol{y}_i) < f(\boldsymbol{y}_j)$.

In general, the transition of the parental family of object parameter vectors $\boldsymbol{x}_1^{(g)}, \ldots, \boldsymbol{x}_\mu^{(g)}$ from generation g to $g+1$ is accomplished according to the following coherent scheme:

1. Recombination of $\rho \le \mu$ randomly selected parental vectors into the recombinant vector $\langle\boldsymbol{x}\rangle^{(g)}$. The recombination is either a definite or random algebraic operation.
2. Mutation of the recombinant vector $\langle\boldsymbol{x}\rangle^{(g)}$ to produce a new population of $\lambda > \mu$ offspring
$$\boldsymbol{y}_1^{(g+1)}, \ldots, \boldsymbol{y}_\lambda^{(g+1)} \in \mathbb{R}^n \quad \leftarrow \quad p^{(g)}\langle\boldsymbol{x}\rangle^{(g)}, \quad (4)$$
where the maximally unbiased mutation operator corresponds to an n-dimensional correlated normal mutation distribution with zero mean and covariance matrix $\boldsymbol{C}^{(g)}$, i.e
$$p^{(g)}\langle\boldsymbol{x}\rangle^{(g)} = \langle\boldsymbol{x}\rangle^{(g)} + N(0, \boldsymbol{C}^{(g)}). \quad (5)$$

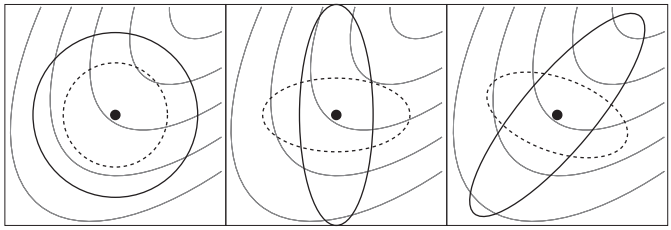

Fig. 1. Examples of isotropic, uncorrelated, and correlated mutation distributions (indicated by circles, axis-parallel ellipsoids, and rotated ellipsoids, respectively) rendered over an elongated valley topography. The best average progress toward the topographic minimum in the direction of the upper right corner is achieved in the right panel, where the mutation distribution (solid ellipsoid) is adapted to the topography

3. Selection of the μ best individuals among the offspring population (or the union of offspring and parents) to become the next generation of parental vectors
$$\boldsymbol{x}_i^{(g+1)} = \boldsymbol{y}_{i:\lambda}^{(g+1)}, \quad i = 1, \ldots, \mu. \quad (6)$$

In contrast to the transition of parental vectors, there is no coherent conceptual scheme for the transition of the mutation operator $p^{(g)}$ from generation g to $g+1$. However, for basic considerations, any advanced transition scheme is expected to reflect the following elementary principles:

1. Invariance of the resulting ES with respect to any strictly monotone remapping of the range of the objective function as well as any linear transformation of the object parameter space. In particular, the resulting ES is expected to be unaffected by translation, rotation, and reflection.
2. Self-adaption of (the shape of) the mutation distribution to the topography of the objective function (Fig. 1). In particular, the mutation distribution is expected to reproduce the precedently selected mutation steps with increased likelihood.

The rigid implementation of these principles results in a concept of completely derandomized self-adaption where the transition of the mutation operator from one generation to the next is accomplished by successively updating the covariance matrix of the mutation distribution with information provided by the actually selected mutation step. The further demand of nonlocality involves the cumulation of the selected mutation steps into an evolution path.

2.2. Covariance matrix adaption (CMA)

If $\boldsymbol{z}_1, \ldots, \boldsymbol{z}_{m\in\mathbb{N}} \in \mathbb{R}^n$, $m \ge n$ are a generating set of $\mathbb{R}^n$ and $q_1, \ldots, q_m \in \mathbb{R}$ are a sequence of $(0, 1)$-normally distributed random variables, then

$$q_1\boldsymbol{z}_1 + \ldots + q_m\boldsymbol{z}_m \quad (7)$$

renders an n-dimensional normal distribution with zero mean and covariance matrix

$$\boldsymbol{z}_1\boldsymbol{z}_1^{\mathrm{T}} + \ldots + \boldsymbol{z}_m\boldsymbol{z}_m^{\mathrm{T}}. \quad (8)$$

In fact, Eq. (7) facilitates the realization of any normal distribution with zero mean. In particular, the symmetric rank-one matrix $\boldsymbol{z}_i\boldsymbol{z}_i^{\mathrm{T}}$ corresponds to the normal distribution with zero mean

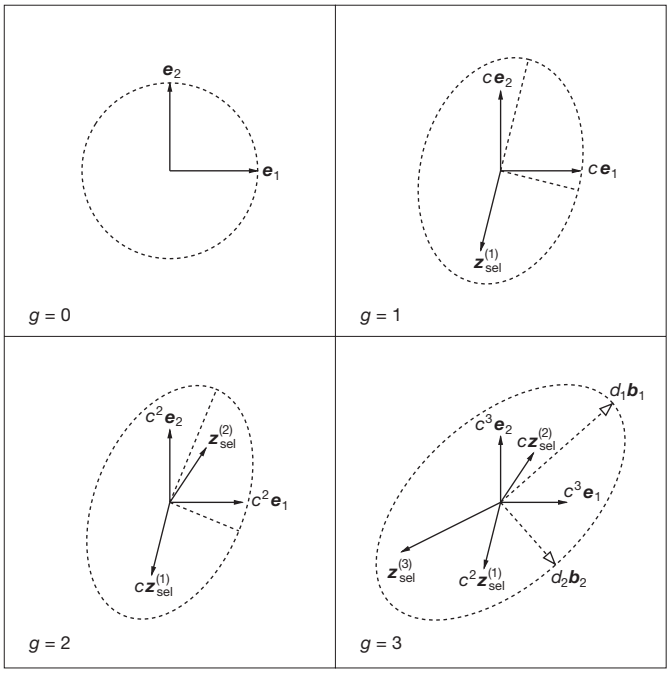

Fig. 2. The conceptual scheme of covariance matrix adaption (CMA). Initially, the covariance matrix of the mutation distribution is $\boldsymbol{C}^{(0)} = \boldsymbol{e}_1\boldsymbol{e}_1^{\mathrm{T}} + \boldsymbol{e}_2\boldsymbol{e}_2^{\mathrm{T}}$. In the course of the transition to the next generation $g+1$ the symmetric rank-one matrix $z_{\mathrm{sel}}^{(g+1)}(\boldsymbol{z}_{\mathrm{sel}}^{(g+1)})^{\mathrm{T}}$, where $z_{\mathrm{sel}}^{(g+1)}$ is the actually selected mutation step, is added to the downscaled covariance matrix. In the third generation, the covariance matrix is $\boldsymbol{C}^{(3)} = c^6\boldsymbol{e}_1\boldsymbol{e}_1^{\mathrm{T}} + c^6\boldsymbol{e}_2\boldsymbol{e}_2^{\mathrm{T}} + \sum_{i=1}^{3} c^{2(3-i)}z_{\mathrm{sel}}^{(i)}(\boldsymbol{z}_{\mathrm{sel}}^{(i)})^{\mathrm{T}} = d_1^2\boldsymbol{b}_1\boldsymbol{b}_1^{\mathrm{T}} + d_2^2\boldsymbol{b}_2\boldsymbol{b}_2^{\mathrm{T}}$, where $\boldsymbol{b}_1$ and $\boldsymbol{b}_2$ are the unit eigenvectors of $\boldsymbol{C}^{(3)}$ corresponding to the eigenvalues d_1^2 and d_2^2. The resulting mutation distribution reads $N(0,\boldsymbol{C}^{(3)}) = N(0,1)\,d_1\boldsymbol{b}_1 + N(0,1)\,d_2\boldsymbol{b}_2$

producing the vector $\boldsymbol{z}_i$ with the maximum likelihood. Since the objective of CMA is to reproduce the precedent mutation steps with increased likelihood, the whole trick to accomplish this objective is to add the symmetric rank-one matrix

$$\boldsymbol{z}_{\mathrm{sel}}^{(g+1)}(\boldsymbol{z}_{\mathrm{sel}}^{(g+1)})^{\mathrm{T}}, \tag{9}$$

where $\boldsymbol{z}_{\mathrm{sel}}^{(g+1)}$ denotes the actually selected mutation step, to the covariance matrix of the mutation distribution. The conceptual scheme is illustrated in Fig. 2. Initially, the mutation distribution is isotropic

$$N(0,\boldsymbol{C}^{(0)}) = N(0,1)\,\boldsymbol{e}_1 + N(0,1)\,\boldsymbol{e}_2, \tag{10}$$

whereas in the course of the transition to the next generation the symmetric rank-one matrix Eq. (9) is added to the downscaled covariance matrix

$$\boldsymbol{C}^{(g+1)} = c^2\boldsymbol{C}^{(g)} + \boldsymbol{z}_{\mathrm{sel}}^{(g+1)}(\boldsymbol{z}_{\mathrm{sel}}^{(g+1)})^{\mathrm{T}}, \quad c \in [0,1). \tag{11}$$

In the course of the third generation, for instance, the mutation distribution reads

$$\begin{aligned} N(0,\boldsymbol{C}^{(3)}) &= N(0,1)\,c^3\boldsymbol{e}_1 + N(0,1)\,c^3\boldsymbol{e}_2 + \sum_{i=1}^{3} N(0,1)\,c^{3-i}\boldsymbol{z}_{\mathrm{sel}}^{(i)} \\ &= N(0,1)\,d_1\boldsymbol{b}_1 + N(0,1)\,d_2\boldsymbol{b}_2, \end{aligned} \tag{12}$$

where $\boldsymbol{b}_1$ and $\boldsymbol{b}_2$ are the unit eigenvectors of $\boldsymbol{C}^{(3)}$ corresponding to the eigenvalues d_1^2 and d_2^2. Obviously, the mutation distribution tends to reproduce the precedent selected mutation steps. Finally, the mutation distribution becomes stationary (apart from the scale) while its principal axes achieve conjugate perpendicularity, and $\boldsymbol{C}^{(g)}$ effectively approaches the scaled inverse Hessian matrix of the objective function.

2.3. Evolution path cumulation

The efficiency as well as the stability of an ES improve significantly if the decision how to adapt the mutation distribution is based on the cumulation of several selected mutation steps rather than a single step. While the latter maximizes the local selection probability the former is more likely to advance the global progress rate. The benefit from superseding the successively selected mutation steps in favor of the evolution path

$$\boldsymbol{p}^{(g+1)} = (1-c)\boldsymbol{p}^{(g)} + \sqrt{c(2-c)}\boldsymbol{z}_{\mathrm{sel}}^{(g+1)}, \quad c \in (0,1] \tag{13}$$

is illustrated in detail in Paper A: If several successively selected mutation steps are parallel (antiparallel) correlated, the evolution path will be lengthened (shortened). If the evolution path is long (short), the size of the mutation steps in direction of the evolution path increases (decreases). The effect of cumulation is particularly beneficial for small populations where the topographical information gathered within one generation is not sufficient. If $c = 1$, no cumulation will occur and $\boldsymbol{p}^{(g+1)} = \boldsymbol{z}_{\mathrm{sel}}^{(g+1)}$.

2.4. The CMA evolution strategy (CMA-ES)

In this section we compile a unified formulation of the generic CMA-ES algorithms given in Papers A and B. In this form, the algorithm is not presented elsewhere. Besides the rank-one CMA outlined in the previous sections the algorithm features the advanced-rank CMA introduced in Paper B and an additional step size control. Finally, we conclude with remarks concerning the numerical implementation of the CMA-ES algorithm we provide online.

2.4.1. Generic algorithm

The state of the (μ,λ)-CMA-ES in generation g is defined by the family of parental vectors $\boldsymbol{x}_1^{(g)},\ldots,\boldsymbol{x}_\mu^{(g)} \in \mathbb{R}^n$, the covariance matrix of the mutation distribution $\boldsymbol{C}^{(g)} \in \mathbb{R}^{n\times n}$, the global mutation step size $\sigma^{(g)} \in \mathbb{R}^+$, and the evolution paths $\boldsymbol{p}_{\mathrm{c}}^{(g)}, \boldsymbol{p}_\sigma^{(g)} \in \mathbb{R}^n$. The generic algorithm is completely defined by the transition from generation g to $g+1$:

1. Weighted intermediate recombination[1] of the parental vectors into the recombinant vector

$$\langle\boldsymbol{x}\rangle^{(g)} = \frac{\sum_{i=1}^{\mu} w_i\boldsymbol{x}_i^{(g)}}{\sum_{i=1}^{\mu} w_i}, \quad w_1,\ldots,w_\mu \in \mathbb{R}^+. \tag{14}$$

[1] Discrete recombination such as the cross-over commonly practiced in genetic algorithms is not invariant with respect to linear transformations of the search space.

The weights $w_1, \ldots, w_\mu$ are internal strategy parameters with canonical values

$$w_i = \ln(\mu + 1) - \ln(i), \quad i = 1, \ldots, \mu. \tag{15}$$

The initial recombinant vector $\langle \boldsymbol{x} \rangle^{(0)}$ is expected to enable the resulting mutation operator to sample the relevant part of the object parameter space.

2. Mutation of the recombinant vector to produce a new family of $\lambda > \mu$ offspring

$$\boldsymbol{y}_k^{(g+1)} = \langle \boldsymbol{x} \rangle^{(g)} + \sigma^{(g)} \boldsymbol{B}^{(g)} \boldsymbol{D}^{(g)} \boldsymbol{z}_k^{(g+1)}, \quad k = 1, \ldots, \lambda, \tag{16}$$

where $\boldsymbol{z}_1^{(g+1)}, \ldots, \boldsymbol{z}_\lambda^{(g+1)} \in \mathbb{R}^n$ are a family of $(0, \boldsymbol{I})$-normally distributed random vectors (i.e. the vector components are $(0, 1)$-normally distributed), and $\boldsymbol{D}^{(g)}, \boldsymbol{B}^{(g)} \in \mathbb{R}^{n \times n}$ diagonalize the covariance matrix

$$\boldsymbol{C}^{(g)} = \boldsymbol{B}^{(g)} \boldsymbol{D}^{(g)} \boldsymbol{D}^{(g)} (\boldsymbol{B}^{(g)})^{\mathrm{T}}. \tag{17}$$

The elements of the diagonal matrix $\boldsymbol{D}^{(g)}$ are the square roots of the eigenvalues of $\boldsymbol{C}^{(g)}$, while the column vectors of $\boldsymbol{B}^{(g)}$ are the corresponding unit eigenvectors. Constrained optimization can be realized by resampling $\boldsymbol{z}_1^{(g+1)}, \ldots, \boldsymbol{z}_\lambda^{(g+1)}$ until the constraints are satisfied.

3. Selection of the μ best individuals among the offspring population to become the next generation of parental vectors

$$\boldsymbol{x}_i^{(g+1)} = \boldsymbol{y}_{i:\lambda}^{(g+1)}, \quad i = 1, \ldots, \mu. \tag{18}$$

Since the production of offspring is independent of order the values of the objective function

$$f(\boldsymbol{y}_k^{(g+1)}), \quad k = 1, \ldots, \lambda \tag{19}$$

can be computed in parallel.

4. Cumulation of the distribution evolution path

$$\boldsymbol{p}_{\mathrm{c}}^{(g+1)} = (1 - c_{\mathrm{c}}) \boldsymbol{p}_{\mathrm{c}}^{(g)} + c_w \sqrt{c_{\mathrm{c}}(2 - c_{\mathrm{c}})} \boldsymbol{B}^{(g)} \boldsymbol{D}^{(g)} \langle \boldsymbol{z} \rangle^{(g+1)} \tag{20}$$

with

$$c_w = \frac{\sum_{i=1}^{\mu} w_i}{\sqrt{\sum_{i=1}^{\mu} w_i^2}} \tag{21}$$

and

$$\langle \boldsymbol{z} \rangle^{(g+1)} = \frac{\sum_{i=1}^{\mu} w_i \boldsymbol{z}_{i:\lambda}^{(g+1)}}{\sum_{i=1}^{\mu} w_i}, \tag{22}$$

where $\boldsymbol{z}_{i:\lambda}^{(g+1)}$ follows from $\boldsymbol{y}_{i:\lambda}^{(g)}$ by Eq. (16). The distribution cumulation rate $c_{\mathrm{c}} \in (0, 1]$ is an internal strategy parameter with canonical value

$$c_{\mathrm{c}} = \frac{4}{n + 4}. \tag{23}$$

If $c_{\mathrm{c}} = 1$, no cumulation will occur. Initially, the distribution evolution path is $\boldsymbol{p}_{\mathrm{c}}^{(0)} = 0$.

5. Adaption of the covariance matrix

$$\boldsymbol{C}^{(g+1)} = (1 - c_{\mathrm{cov}}) \boldsymbol{C}^{(g)} + c_{\mathrm{cov}} \left(\alpha_{\mathrm{cov}} \boldsymbol{p}_{\mathrm{c}}^{(g+1)} (\boldsymbol{p}_{\mathrm{c}}^{(g+1)})^{\mathrm{T}} + (1 - \alpha_{\mathrm{cov}}) \langle \boldsymbol{Z} \rangle^{(g+1)} \right), \tag{24}$$

where

$$\langle \boldsymbol{Z} \rangle^{(g+1)} = \frac{\sum_{i=1}^{\mu} w_i \boldsymbol{B}^{(g)} \boldsymbol{D}^{(g)} \boldsymbol{z}_{i:\lambda}^{(g+1)} \left(\boldsymbol{B}^{(g)} \boldsymbol{D}^{(g)} \boldsymbol{z}_{i:\lambda}^{(g+1)} \right)^{\mathrm{T}}}{\sum_{i=1}^{\mu} w_i}. \tag{25}$$

The expressions $\boldsymbol{p}_{\mathrm{c}}^{(g+1)} (\boldsymbol{p}_{\mathrm{c}}^{(g+1)})^{\mathrm{T}}$ and $\langle \boldsymbol{Z} \rangle^{(g+1)}$ are symmetric matrices of rank one and $\min(\mu, n)$, respectively, and generalize the conceptual scheme illustrated in Fig. 2 in case of a single parent ES. The parameter $\alpha_{\mathrm{cov}} \in [0, 1]$ combines the two adaption mechanisms whereas $c_{\mathrm{cov}} \in [0, 1)$ moderates the adaption rate. Both numbers are internal strategy parameters with canonical values

$$\alpha_{\mathrm{cov}} = c_w^{-2} \tag{26}$$

and

$$c_{\mathrm{cov}} = \frac{2\alpha_{\mathrm{cov}}}{(n + \sqrt{2})^2} + (1 - \alpha_{\mathrm{cov}}) \min\left(1, \frac{2c_w^2 - 1}{(n + 2)^2 + c_w^2}\right). \tag{27}$$

If $c_{\mathrm{cov}} = 0$, no adaption will occur. Initially, $\boldsymbol{C}^{(0)} = \boldsymbol{I}$ or the square of any diagonal matrix properly scaling the optimization problem.

6. Cumulation of the step size evolution path

$$\boldsymbol{p}_\sigma^{(g+1)} = (1 - c_\sigma) \boldsymbol{p}_\sigma^{(g)} + c_w \sqrt{c_\sigma(2 - c_\sigma)} \boldsymbol{B}^{(g)} \langle \boldsymbol{z} \rangle^{(g+1)}, \tag{28}$$

where the step size cumulation rate $c_\sigma \in (0, 1]$ is an internal strategy parameter with canonical value

$$c_\sigma = \frac{c_w^2 + 2}{n + c_w^2 + 3}. \tag{29}$$

If $c_\sigma = 1$, no cumulation will occur. Initially, the step size evolution path is $\boldsymbol{p}_\sigma^{(0)} = 0$.

7. Adaption of the global mutation step size

$$\sigma^{(g+1)} = \sigma^{(g)} \exp\left(\frac{c_\sigma}{d_\sigma} \frac{\|\boldsymbol{p}_\sigma^{(g+1)}\| - E_n}{E_n} \right), \tag{30}$$

where the second fraction is the relative deviation of the length of $\boldsymbol{p}_\sigma^{(g+1)}$ from its expected value if there were no selection pressure, $E_n = \sqrt{2}\Gamma(\frac{n+1}{2})/\Gamma(\frac{n}{2})$, and the damping constant $d_\sigma \geq c_\sigma$ is an internal strategy parameter with canonical value

$$d_\sigma = 1 + c_\sigma + 2 \max\left(0, \sqrt{\frac{c_w^2 - 1}{n + 1}} - 1\right). \tag{31}$$

The initial mutation step size $\sigma^{(0)}$ is expected to enable the resulting mutation distribution to sample the relevant part of the object parameter space.

The impact and canonical setting of internal strategy parameters are discussed in detail in Paper A and in Hansen & Kern (2004).

2.4.2. Numerical implementation

The numerical implementation of the CMA-ES algorithm is quite straightforward.[2] We coded different function templates

[2] Sophisticated examples are given on the home page of Nikolaus Hansen at `http://www.bionik.tu-berlin.de`

for both unconstrained and constrained optimization. The template instantiation requires a random number generator and an eigenvalue decomposition algorithm to be supplied as generic arguments. The numerical code is designed to perform in parallel when running on shared memory multiprocessing architectures and has been applied in practice by Quast et al. (2002, 2004) and Reimers et al. (2003).[3]

Since an adequate random number generator producing high-dimensional equidistribution is absolutely essential to ensure that the ES performs in practice as expected in theory, we apply the Mersenne Twister algorithm furnishing equidistributed uniform deviates in up to 623 dimensions with period $2^{19937}-1$ (Matsumoto & Nishimura 1998). The uniform deviates are converted into normal deviates by means of the polar method.

The Linear Algebra Package provides several algorithms suitable for diagonalizing the covariance matrix. For example, the routines decomposing tridiagonal matrices into relatively robust representations accurately complete the diagonalization of an $n \times n$ symmetric tridiagonal matrix in $O(n^2)$ rather than the regular $O(n^3)$ arithmetic operations (Dhillon & Parlett 2004). In particular, it is feasible to diagonalize the covariance matrix just every $n/10$ generation to minimize the numerical overhead (Paper A). For, say, $n > 10\,000$ using completely correlated mutation distributions will be impracticable and an ES algorithm calculating just the tridiagonal covariance matrix elements or adapting just individual step sizes ($\boldsymbol{B}^{(g)} = \boldsymbol{I}$, $\boldsymbol{C}^{(g)} = \boldsymbol{D}^{(g)}\boldsymbol{D}^{(g)}$ diagonal) will be appropriate.

3. Spectral decomposition

In the case of pure line absorption, the observed spectral flux $F(\lambda)$ is modelled as the product of the continuum background and the instrumentally convolved absorption term

$$F(\lambda) = C(\lambda) \int P(\xi)\, \mathrm{e}^{-\tau(\lambda-\xi)}\, \mathrm{d}\xi. \tag{32}$$

Defining

$$A(\lambda) = \int P(\xi)\, \mathrm{e}^{-\tau(\lambda-\xi)}\, \mathrm{d}\xi \tag{33}$$

and approximating the local continuum background by a linear combination of Legendre polynomials, Eq. (32) transforms into

$$F(\lambda) = \sum_k c_k\, L_k[\phi(\lambda)] A(\lambda), \tag{34}$$

where L_k denotes the Legendre polynomial of order k, and ϕ is a linear map onto the interval $[-1, 1]$. The instrumental profile $P(\xi)$ is modelled by a normalized Gaussian defined by the spectral resolution of the instrument. The instrumental convolution can be calculated piecewise analytically by approximating the absorption term with a polyline or a cubic spline. Without significant loss of accuracy the integration can be restricted to the interval $|\xi| \le 2\delta$, where δ is the full width at half maximum of the instrumental profile.

[3] The source code is publicly available on the home page of RQ at `http://www.hs.uni-hamburg.de`

On the presumption of pure Doppler broadening, the optical depth τ is modelled by a superposition of Gaussian functions. If λ_i, f_i, z_i, b_i, N_i, and $\lambda_{z_i} = (1+z_i)\lambda_i$ denote, respectively, the rest wavelength, the oscillator strength, the cosmological redshift, the line broadening velocity, the column density, and the observed wavelength corresponding to line i, then

$$\tau(\lambda) = \sum_i g_i(\lambda) \tag{35}$$

with

$$g_i(\lambda) = \frac{e^2}{4\varepsilon_0 mc} \frac{N_i f_i \lambda_i}{\sqrt{\pi} b_i} \exp\left[-\left(\frac{c}{b_i}\frac{\lambda-\lambda_{z_i}}{\lambda_{z_i}}\right)^2\right]. \tag{36}$$

If natural broadening is important, the Gaussian functions will have to be replaced with Voigt functions. The latter can be calculated efficiently by using pseudo-Voigt approximations (Ida et al. 2000).

Taking the proper identification of lines for granted, the decomposition of an absorption line spectrum into individual profiles is a parametric inverse problem involving a tuple of three model parameters per line: position, broadening velocity, and column density. Given an observed set of spectral fluxes $F_1, F_2, \ldots$ and normally distributed errors $\sigma_1, \sigma_2, \ldots$ sampled at wavelengths $\lambda_1, \lambda_2, \ldots$ the optimal parametric decomposition $F(\lambda)$ is calculated by minimizing the normalized residual sum of squares

$$\mathrm{RSS} = \sum_j \left(\frac{F_j - F(\lambda_j)}{\sigma_j}\right)^2. \tag{37}$$

For any $A(\lambda)$, the minimization with respect to the coefficients c_k presents a linear optimization problem

$$\mathrm{RSS} = \sum_j \left(\frac{F_j - \sum_k c_k L_k[\phi(\lambda_j)] A(\lambda_j)}{\sigma_j}\right)^2 \tag{38}$$

which is solved directly by means of Cholesky decomposition. For normally distributed errors the minimum RSS maximizes the likelihood. Note that since the normalized RSS is invariant with respect to permutations of line parameter 3-tuples, any self-adaptive ES will initially require several generations to adapt to the symmetry. Any further global degeneracies of the search space will lengthen the initial adaption phase.

4. Performance tests

4.1. Test cases

We have synthesized four exemplary test cases to investigate the global optimization performance of the CMA-ES when applied to the problem of spectral decomposition. The test cases are based on the characteristics of real QSO spectra and present a series of metal line ensembles increasing in complexity. Test cases A, B, C, and D render superpositions of six, eight, ten, and twelve components, respectively (Fig. 3). All test cases are synthesized simulating an instrumental resolution of $R = 60\,000$ and a curved background continuum. Both Poissonian and Gaussian white noise are added, producing a

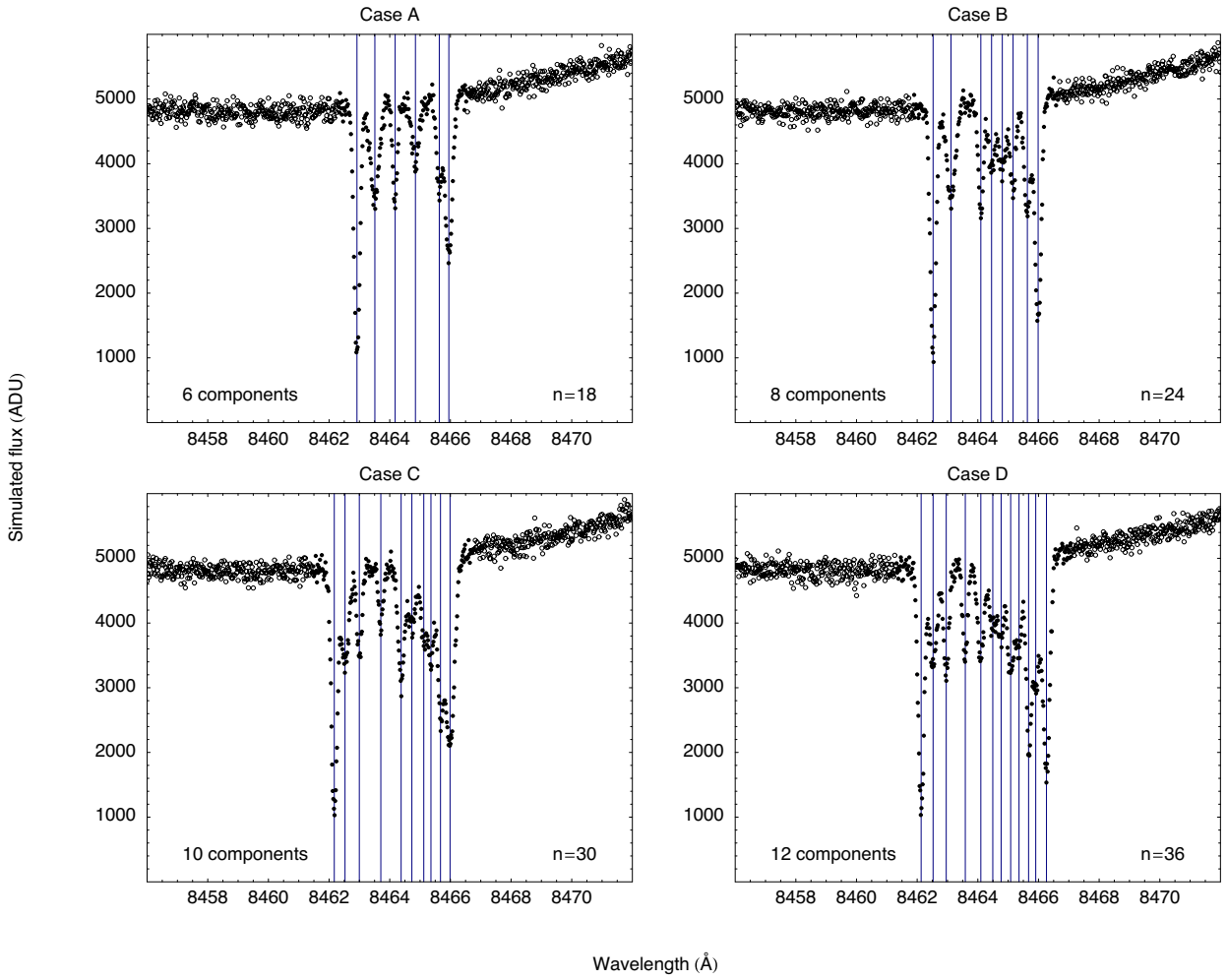

Fig. 3. Artificial test cases based on an ensemble of extragalactic Ca II λ3935 lines toward the QSO HE 0515–4414. The simulated instrumental resolution is $R = 60\,000$ while the simulated signal-to-noise ratio is about 50. Individual components are marked by vertical lines.

random continuum noise level of about two percent. Since ES are not destabilized by small scale oscillations of the objective function, the complexity of the decomposition problem does not depend on the noise level of the data but is solely determined by the number and separation of spectral lines. The parameterization of the artificial lines used to synthesize the test cases is listed in Table 1. Several lines are barely separated or occcur close to the limit of the simulated spectral resolution. The test case characteristics are motivated by the analysis of QSO spectra recorded with the UVES spectropgraph installed at the ESO VLT. Further test cases exhibiting different characteristics will emerge in the future throughout the analysis of QSO spectra recorded with the CES spectrograph. We do not consider line ensembles consisting of less than six components since these cases normally pose no challenge to the CMA-ES algorithm. Primitive cases exhibiting just a single component are completed in less than 50 generations using the canonical $(1, 10)$-CMA-ES.

4.2. Algorithm application

We compare the global performance of the CMA-ES to that of several classical optimization algorithms provided by the Numerical Recipes collection: Fletcher-Reeves-Polak-Ribiere (FRPR, a conjugate gradient variant), Broyden-Fletcher-Goldfab-Shanno (BFGS, a virtual metric variant), Levenberg-Marquardt, Powell (a direction set variant), and the downhill simplex. The latter two algorithms do not require the calculation of partial derivatives and serve as direct standards of comparison.

The positional search space is restricted to an interval 40 percent wider than the separation of the outer components (Fig. 3), while the broadening velocities and column densities are confined to $1.0 \leq b\ (\mathrm{km\,s^{-1}}) \leq 10.0$ and $10.0 \leq \log N\ (\mathrm{cm^{-2}}) \leq 14.0$. Since the classical algorithms are not able to handle simple parametric bounds per se, the Numerical Recipes routines are modified in such a way that any step that attempts to escape is suppressed. The partial derivatives required by the FRPR, BFGS, and Levenberg-Marquardt algorithms are calculated numerically using the symmetrized difference quotient approximation. Regarding the CMA-ES, we apply an $(100, 200)$ algorithm with internal strategy parameters preset to the canonical values except for $\alpha_{\mathrm{cov}} = 0$ and an increased covariance matrix adaption rate c_{cov}. The diagonal elements of $\boldsymbol{C}^{(0)}$ are initialized to the squared half widths of the parameter intervals while the mutation step size is initialized to $\sigma^{(0)} = 0.5$.

Table 1. Parameterization of the artificial lines used to synthesize the test cases rendered in Fig. 3. Rest wavelengths and oscillator strengths comply with the Ca II λ3935 transition. All CMA-ES runs converging at the global minimum result in the same parameterization indicated in parentheses, along with standard deviations provided by the diagonal elements of the scaled covariance matrix

Line	z	b (km s^{-1})	$\log N$ (cm^{-2})
A-1	1.150800 (800)	3.0 (2.9 ± 0.1)	12.30 (12.32 ± 0.01)
A-2	1.150950 (949)	6.0 (6.0 ± 0.2)	11.80 (11.80 ± 0.01)
A-3	1.151120 (119)	2.5 (1.9 ± 0.2)	11.60 (11.60 ± 0.02)
A-4	1.151290 (290)	5.0 (4.8 ± 0.3)	11.50 (11.51 ± 0.02)
A-5	1.151490 (488)	3.0 (2.8 ± 0.3)	11.60 (11.58 ± 0.02)
A-6	1.151570 (569)	4.5 (4.6 ± 0.2)	12.00 (12.01 ± 0.01)
B-1	1.150700 (700)	3.0 (2.9 ± 0.1)	12.30 (12.32 ± 0.01)
B-2	1.150850 (850)	6.0 (6.0 ± 0.2)	11.80 (11.80 ± 0.01)
B-3	1.151100 (101)	2.5 (2.5 ± 0.2)	11.70 (11.69 ± 0.01)
B-4	1.151190 (189)	4.0 (4.0 ± 0.5)	11.50 (11.50 ± 0.03)
B-5	1.151280 (279)	5.5 (5.6 ± 0.7)	11.60 (11.61 ± 0.03)
B-6	1.151370 (370)	3.0 (3.2 ± 0.3)	11.60 (11.60 ± 0.02)
B-7	1.151490 (490)	4.5 (4.4 ± 0.2)	11.80 (11.80 ± 0.01)
B-8	1.151580 (580)	3.5 (3.5 ± 0.1)	12.20 (12.20 ± 0.01)
C-1	1.150610 (610)	3.0 (2.9 ± 0.1)	12.30 (12.32 ± 0.02)
C-2	1.150700 (701)	5.5 (5.4 ± 0.3)	11.80 (11.79 ± 0.02)
C-3	1.150820 (821)	3.0 (2.8 ± 0.3)	11.60 (11.59 ± 0.02)
C-4	1.151000 (000)	2.5 (2.5 ± 0.4)	11.40 (11.38 ± 0.02)
C-5	1.151170 (170)	4.0 (3.9 ± 0.3)	11.80 (11.79 ± 0.02)
C-6	1.151260 (261)	5.5 (5.9 ± 0.8)	11.60 (11.61 ± 0.04)
C-7	1.151360 (358)	3.5 (3.2 ± 0.8)	11.50 (11.51 ± 0.07)
C-8	1.151420 (421)	4.0 (3.9 ± 0.8)	11.70 (11.71 ± 0.05)
C-9	1.151500 (500)	3.5 (3.3 ± 0.4)	11.90 (11.90 ± 0.03)
C-10	1.151580 (579)	6.0 (6.1 ± 0.2)	12.20 (12.21 ± 0.01)
D-1	1.150600 (600)	3.0 (3.0 ± 0.1)	12.30 (12.30 ± 0.01)
D-2	1.150700 (700)	5.5 (5.5 ± 0.2)	11.80 (11.81 ± 0.01)
D-3	1.150810 (810)	3.0 (3.0 ± 0.2)	11.70 (11.70 ± 0.01)
D-4	1.150970 (968)	2.5 (2.5 ± 0.2)	11.60 (11.59 ± 0.01)
D-5	1.151100 (098)	4.0 (4.1 ± 0.2)	11.70 (11.70 ± 0.02)
D-6	1.151200 (203)	5.5 (5.5 ± 1.0)	11.60 (11.60 ± 0.06)
D-7	1.151270 (270)	3.0 (2.8 ± 0.8)	11.50 (11.47 ± 0.08)
D-8	1.151350 (347)	4.5 (4.0 ± 0.6)	11.80 (11.77 ± 0.05)
D-9	1.151420 (418)	3.5 (4.6 ± 0.8)	11.60 (11.69 ± 0.06)
D-10	1.151500 (500)	2.5 (2.2 ± 0.3)	12.00 (12.00 ± 0.02)
D-11	1.151560 (562)	5.0 (5.3 ± 0.7)	11.90 (11.93 ± 0.04)
D-12	1.151650 (651)	4.0 (3.9 ± 0.1)	12.20 (12.19 ± 0.01)

For each algorithm and test case we monitor the history of 100 randomly initialized optimization runs. Providing the true number of absorption components as prior information, the initial object parameters are randomly drawn from a uniform distribution. The random noise is generated only once for each test case and is the same for all runs. All optimization runs are stopped after 100 000 evaluations of the normalized RSS.

4.3. Test results

The optimization runs are evaluated in terms of the ratio of the final normalized RSS to the normalized RSS corresponding to the true parameterization. For all test cases the RSS ratio is marginally less than unity at the global minimum. In general, an RSS ratio of unity just indicates the statistical consistency of the optimized and the true absorption profiles, but does not indicate the consistency of the optimized and the true parameterization. In particular in the case of QSO spectra exhibiting lower signal-to-noise ratios inconsistent optimized parameters will occur regularly. However, since in our test cases the true parameterization is recovered by all runs converging at the global minimum (Table 1) the RSS ratio is appropriate for assessing the global optimization performance. The outcome of optimization runs is summarized in Fig. 4 and Table 2 while Fig. 5 illustrates the performance of the CMA-ES during different stages of the optimization. In the following paragraphs the test results are described in detail.

4.3.1. Case A

Case A consists of four isolated and two blended components. The lowest local minimum occurs when the weaker line of the blend is missed, but an isolated line is hit twice instead. Higher local minima occur whenever the blend is modelled correctly but any isolated component is missed. The CMA-ES hits the global minimum in 56, and the lowest local minimum in 38 runs. Another six runs converge at higher local minima but miss an isolated component. The most stable classical technique is the Powell algorithm, which arrives at the global minimum in six, at the lowest local minimum in nine, and between these both in twelve runs. The most successful gradient technique is the Levenberg-Marquardt algorithm, which reaches the global minimum in three runs. The latter algorithm is also the fastest, needing about 1000 evaluations of the normalized RSS to locate the global minimum, whereas the Powell and CMA-ES algorithms require about 14 000 and 18 000 evaluations, respectively. The FRPR and simplex algorithms hit the global minimum in two runs each, needing about 36 000 and 68 000 RSS evaluations, respectively. Except for the Powell algorithm the majority of deterministic runs misses two or more components. The BFGS algorithm never hits any component.

4.3.2. Case B

Case B is similar to case A but exhibits two additional components and a less narrow blend. The CMA-ES hits the global minimum in 77 and the lowest local minimum in 15 runs. Another eight runs converge at higher local minima. No deterministic algorithm locates the global minimum in more than three runs. The Powell algorithm is still relatively stable, missing one or two components in the majority of runs.

4.3.3. Case C

Case C again exhibits two additional components resulting in an ensemble of largely blended lines. The lowest local minimum occurs when the seventh component is missed, but another component is hit twice instead. The global minimum of the objective function almost has degenerated, being different from the lowest local minimum by merely seven percent. The CMA-ES hits the global minimum in 32 and the lowest local

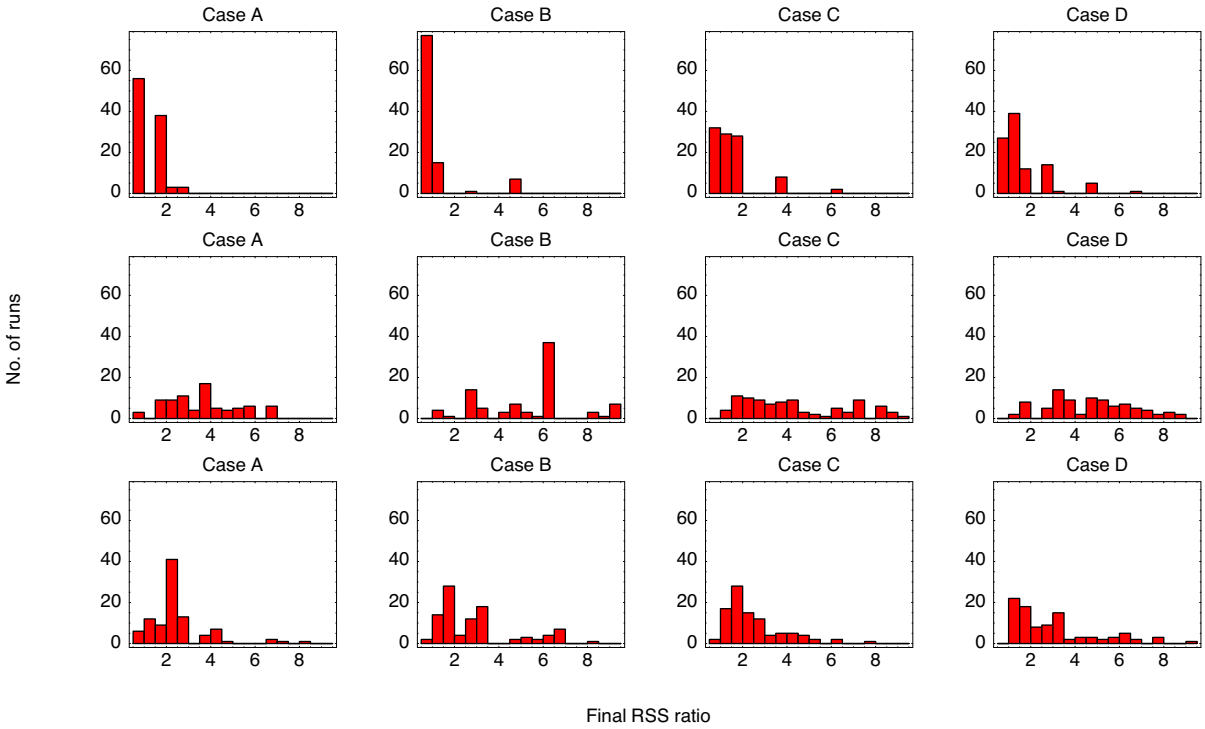

Fig. 4. Outcome of 100 randomly initialized optimization runs using the CMA-ES (first row of histograms), Levenberg-Marquardt (second row), and Powell algorithms. The number of runs converging at the global minimum is indicated by the leftmost bar. The FRPR, BFGS, and simplex algorithms perform less well and are omitted for convenience

Table 2. Global optimization performance summarized in terms of the median of the final normalized RSS ratio, the number of runs converging at the global minimum, and the median number of RSS evaluations needed

Algorithm	Case A			Case B			Case C			Case D		
CMA-ES	0.97	56	18 000	0.99	77	40 000	1.04	32	62 000	1.09	27	82 000
FRPR	4.86	2	36 000	9.45	3	70 000	6.65	–	–	11.7	–	–
BFGS	26.8	–	–	32.9	–	–	34.7	–	–	37.5	–	–
Levenberg-Marquardt	3.97	3	1000	6.11	–	–	4.24	–	–	5.04	–	–
Powell	2.12	6	14 000	2.67	2	20 000	2.05	2	26 000	2.69	–	–
Simplex	12.2	2	68 000	25.6	–	–	6.96	–	–	35.8	–	–

minimum in 22 runs. The majority of the remaining runs converges at higher local minima while missing a different component than the seventh. The Powell algorithm hits the global as well as the lowest local minimum in 2 runs each and misses one or two components in the majority of runs. No other classical algorithm hits the global minimum.

4.3.4. Case D

Case D is very similar to case C but exhibits two additional components. The CMA-ES hits the global minimum in 27 runs. The majority of runs arrives at lower local minima without becoming stationary (Fig. 5). No classical algorithm hits the global minimum.

4.3.5. Efficiency

The number of RSS evaluations required by the CMA-ES to converge at the global minimum increases linearly with the number of lines superimposed in the test case (Table 2). The CMA-ES needs about $a = 10\,000$ additional RSS evaluations per additional line, while for the Powell algorithm the additional cost is $a = 3000$.

5. Summary and conclusions

All tested classical algorithms require an adequate initial guess to locate the global optimum of the objective function when applied to the problem of spectral decomposition. In contrast, the CMA-ES is demonstrably capable of calculating the optimal decomposition without demanding any particular initialization, and therefore particularly qualifies for the application in automatized spectroscopic analysis software.

The CMA-ES does not guarantee that the optimal solution will be found: characteristic spectral features are modelled correctly, but features exhibiting just a small attractor volume such as narrow components or tight blends are frequently not distinguished properly. Larger populations are expected to improve

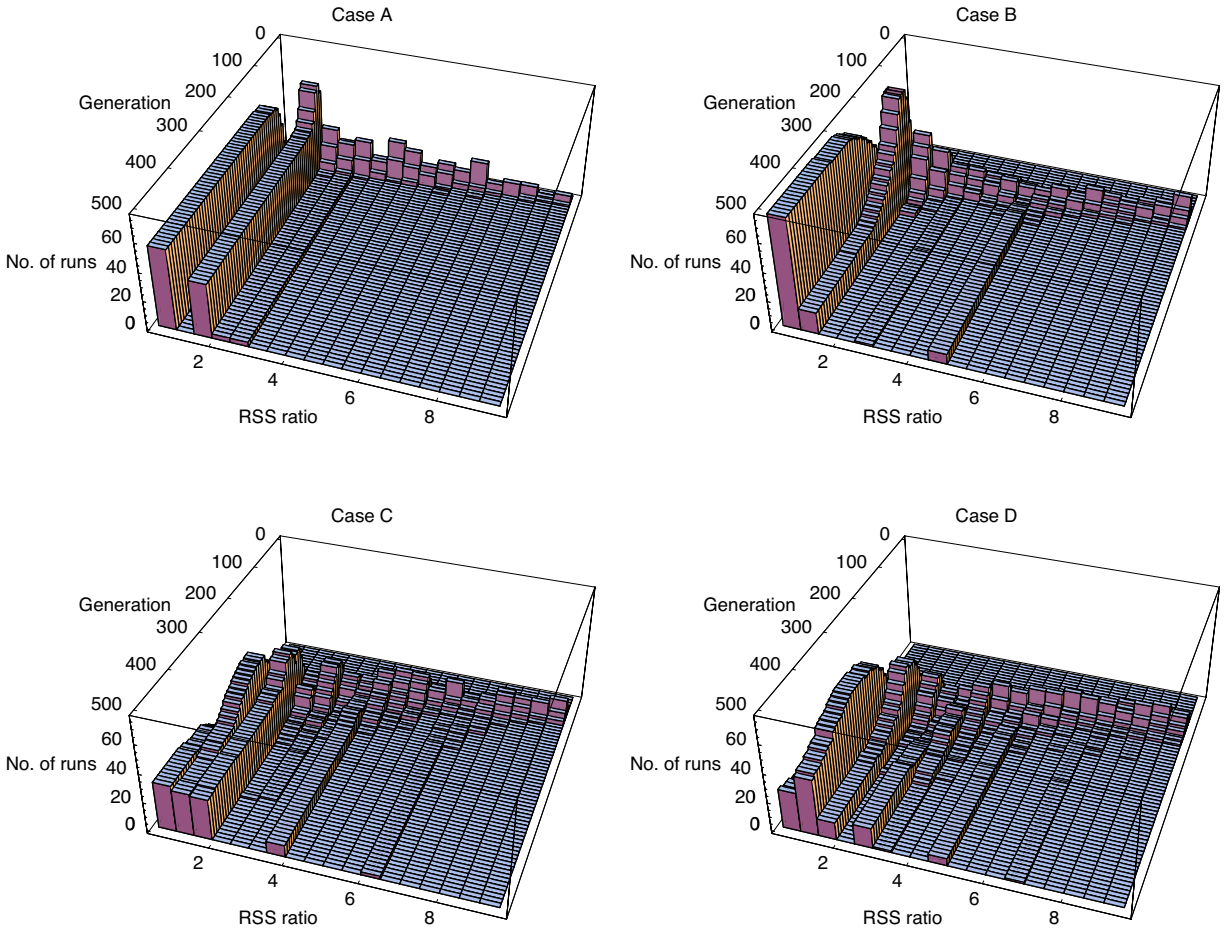

Fig. 5. History of 100 randomly initialized optimization runs using the CMA-ES. The number of runs converging at the global minimum is indicated by the leftmost bar. The number of RSS evaluations is calculated by multiplying the generation number by 200

the chance of hitting the global optimum but require a larger number of objective function evaluations. Peak finding algorithms could detect both the proper number (a problem that we have completely left aside) and position of spectral components and provide an improved initialization. But irrespective of whether an automatized analysis software will be realized, the CMA-ES is an elegant and highly competitive general purpose algorithm that is easy to implement. In our opinion, its integration into the standard astronomical data analysis packages will be thoroughly worthwhile and its widespread use will contribute to the further comprehension and improvement of such algorithms.

Acknowledgements. It is a pleasure to thank Nikolaus Hansen for proofreading the manuscript. This research has been supported by the Verbundforschung of the BMBF/DLR under Grant No. 50 OR 9911 1.

References

Dhillon, I. S. & Parlett, B. N. 2004, SIAM J. Matrix Anal. Appl., 25, 858

Hansen, N. & Kern, S. 2004, in Lect. Not. Comp. Sci., Vol. 3242, Parallel Problem Solving from Nature – PPSN VIII, 282

Hansen, N. & Ostermeier, A. 2001, Evol. Comput., 9, 159 (Paper A)

Hansen, N., Müller, S. D., & Koumoutsakos, P. 2003, Evol. Comput., 11, 1 (Paper B)

Ida, T., Ando, M., & Toraya, H. 2000, J. Appl. Cryst., 33, 1311

Matsumoto, M. & Nishimura, T. 1998, ACM Trans. Model. Comput. Simula., 8, 3

Press, W. H., Teukolsky, S. A., Vetterling, W. T., & Flannery, B. P. 2002, Numerical Recipes in C++ (Cambridge University Press)

Quast, R., Baade, R., & Reimers, D. 2002, A&A, 386, 796

Quast, R., Reimers, D., & Levshakov, S. A. 2004, A&A, 415, L7

Reimers, D., Baade, R., Quast, R., & Levshakov, S. A. 2003, A&A, 410, 785

Revised manuscript. The original version was published in A&A 386, 796–800 (2002)

Fine-structure diagnostics of neutral carbon toward HE 0515–4414⋆

R. Quast, R. Baade, and D. Reimers

Hamburger Sternwarte, Universität Hamburg, Gojenbergsweg 112, D-21029 Hamburg, Germany
e-mail: {rquast,rbaade,dreimers}@hs.uni-hamburg.de

Received 30 November 2001 / Accepted 5 March 2002 / Revised 6 December 2005

ABSTRACT

Aims. We study an ensemble of C I fine-structure QSO absorption lines with redshift 1.15 to infer the physical conditions in the absorbing medium and to test the temperature-redshift relation predicted by standard Friedmann cosmology.
Methods. We used the VLT UVES spectrograph to obtain high-resolution high signal-to-noise spectra of HE 0515–4414. The rate equation is established considering direct photoexcitation by the cosmic microwave background, UV pumping, and collisions with hydrogen atoms.
Results. The resonance lines are seen in two components with total column densities of $\log N = 13.76 \pm 0.02$ and $\log N = 13.33 \pm 0.01$. The upper limit on the local FUV energy density corresponds to the 60-fold Galactic radiation while the number density of hydrogen atoms may reach some 100 cm^{-3}. The cosmic microwave background is only a minor source of excitation. The population temperatures of the ground state fine-stucture levels of $T = 15.8$ and $T = 11.2$ K do not contradict the standard temperature-redshift relation.

Key words. cosmic microwave background – quasars: absorption lines – quasars: individual: HE 0515–4414

1. Introduction

The standard Friedmann cosmology predicts that the temperature of the cosmic microwave background radiation (CMBR) increases linearly with the redshift z as

$$T_{\rm CMBR}(z) = T_{\rm CMBR}(0)\,(1+z). \quad (1)$$

The present-day CMBR temperature has been ascertained by the Cosmic Background Explorer FIRAS instrument to be $T_{\rm CMBR}(0) = 2.725$ K (Mather et al. 1999). In recent years several attempts have been made to infer the CMBR temperature at higher redshifts from the relative population of C^0 (and C^+) fine-structure levels observed in damped Ly α (DLA) systems (Ge et al. 1997, 2001; Roth & Bauer 1999; Srianand et al. 2000). The principal problem in this inference is the presence of additional sources of excitation. In particular, collisional excitation and fluorescence induced by the local FUV radiation field are competing processes. A recent study of Silva & Viegas (2002) shows the possibility to assess the physical conditions in QSO absorbers from the observation of fine-structure absorption lines.

This study provides a fine-structure diagnostics of C I toward the notably bright QSO HE 0515–4414 ($z = 1.73$, $B = 15.0$) discovered by the Hamburg/ESO Survey (Reimers et al. 1998). The observed fine-structure absorption lines (and a large number of additional metal lines) are associated with a DLA system at redshift $z = 1.15$ (de la Varga et al. 2000). We infer the physical conditions in the DLA system and demonstrate that the CMBR is only a minor source of the observed fine-structure excitation.

Send offprint requests to: R. Quast

⋆ Based on observations made with ESO Telescopes at the La Silla or Paranal Observatories under programme ID 066.A-0212.

2. Observations

The QSO HE 0515–4414 was observed during ten nights between October 7, 2000 and January 3, 2001, using the UV-Visual Echelle Spectrograph (UVES) installed at the second VLT Unit Telescope (Kueyen). Thirteen exposures were made in the dichroic mode using standard settings for the central wavelenghts of 3460/4370 Å in the blue, and 5800/8600 Å in the red. The CCDs were read out in fast mode without binning. Individual exposure times were 3600 and 4500 s, under photometric to clear sky and seeing conditions ranging from 0.47 to 0.70 arcsec. The slit width was 0.8 arcsec providing a spectral resolution of about 55 000 in the blue and slightly less in the red. The raw data frames were reduced at the ESO Quality Control Garching using the UVES pipeline Data Reduction Software (DRS) described in Ballester et al. (2000). Finally, the individual vacuum-barycentric corrected spectra were co-added resulting in an effective signal-to-noise ratio typically better than 100 (up to 130 for the parts of the spectrum considered in this study).

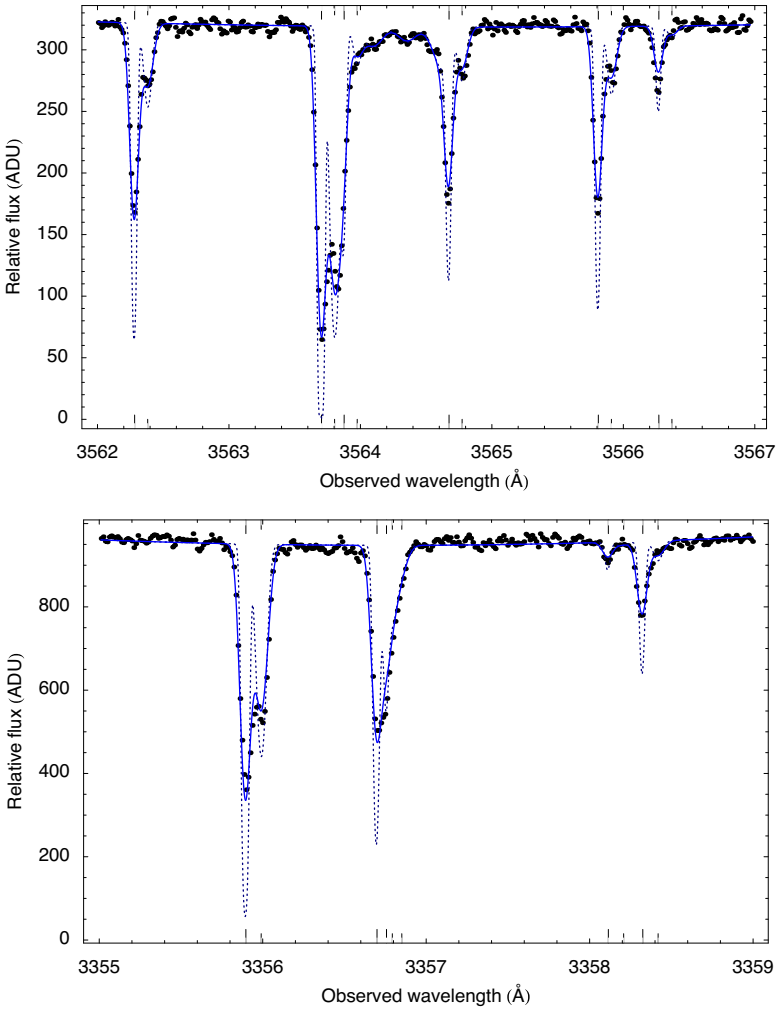

Fig. 1. Parts of the spectrum showing the lines of the multiplets 2 (top panel) and 3 (bottom panel) in C I. The fat dots represent the observed flux. The solid and dashed curves represent our optimized model and its deconvolution, respectively. The long (short) vertical tick marks indicate the major (minor) absorption component in each composite profile. The effective signal-to-noise ratio between the $^3P_1$–$^3P_1$ and $^3P_1$–$^3P_0$ lines (top panel) is about 130. The standard error provided with the reduced flux data is about twice the noise

3. Absorption line analysis

The observed spectral flux F is the convolution of the instrumental profile P with the product of the background continuum C and the absorption term:

$$F(\lambda) = \int P(\xi)C(\lambda - \xi)\, \mathrm{e}^{-\tau(\lambda-\xi)}\, \mathrm{d}\xi. \quad (2)$$

The instrumental profile is approximated by a normalized Gaussian defined by the spectral resolution of the instrument. The background continuum is locally approximated by a linear combination of Legendre polynomials of up to second order. Assuming pure Doppler broadening, the optical depth is modelled by a superposition of Gaussian functions:

$$\tau(\lambda) = \sum_i g_i(\lambda), \quad (3)$$

where

$$g_i(\lambda) = \frac{e^2}{4\epsilon_0 mc} \frac{N_i f_i \lambda_i}{\sqrt{\pi} b_i} \exp\left[-\left(\frac{c}{b_i} \frac{\lambda/(1+z_i) - \lambda_i}{\lambda_i}\right)^2\right] \quad (4)$$

and λ_i, f_i, z_i, b_i and N_i denote the rest wavelength, the oscillator strength, the redshift, the line broadening velocity and the column density of a single line, respectively. Each C I absorption component is modelled by a superposition of Doppler profiles with identical redshifts and widths. In addition, the particular lines originating on the same fine-structure level are restricted to have identical column densities. This simultaneous fine-structure treatment ensures the physical consistency of our analysis. The weak absorption features between the $^3P_2$–$^3P_2$ and $^3P_1$–$^3P_1$ lines seen in Fig. 1 are modelled by a superposition of three artificial Doppler profiles.

Our model is defined by 24 strongly correlated parameters: six parameters to model the background continuum, 17 parameters to model the optical depth, and the spectral resolution of the instrument. In order to find the optimal set of parameter values, we minimize the χ^2 statistic following an adaptive evolution strategy recently proposed by Hansen & Ostermeier (2001). The atomic line data used in this analysis are listed in Table 1.

4. Results and discussion

4.1. Model parameters

The optimized values and formal confidence limits of the model parameters for both C I absorption components are listed in Table 2. The total column density is $\log N = 13.76 \pm 0.02$

Table 1. Atomic data for the radiative transitions of the multiplets 2 and 3 in C I. The vacuum wavelengths λ and oscillator strengths f are excerpted from Morton (2003)

Mult.	Transition		λ (Å)	f
2	$2s^2 2p^2$–$2s^2 2p\,3s$	$^3P_1$–$^3P_2$	1656.2672	0.0589
		$^3P_0$–$^3P_1$	1656.9283	0.139
		$^3P_2$–$^3P_2$	1657.0082	0.104
		$^3P_1$–$^3P_1$	1657.3792	0.0356
		$^3P_1$–$^3P_0$	1657.9068	0.0473
		$^3P_2$–$^3P_1$	1658.1212	0.0356
3	$2s^2 2p^2$–$2s\,2p^3$	$^3P_0$–$^3D_1$	1560.3092	0.0719
		$^3P_1$–$^3D_2$	1560.6822	0.0539
		$^3P_1$–$^3D_1$	1560.7090	0.0180
		$^3P_2$–$^3D_2$	1561.3402	0.0108
		$^3P_2$–$^3D_1$	1561.3667	0.0007
		$^3P_2$–$^3D_3$	1561.4384	0.0603

Table 2. Optimized values and formal 68.3 percent confidence limits of the model parameters for both C I absorption components. The redshift z is accurate to the last digit

Level	z	b (km s^{-1})	$\log N$ (cm^{-2})
$^3P_0$	1.150787	2.01 ± 0.09	13.49 ± 0.03
$^3P_1$			13.32 ± 0.01
$^3P_2$			12.73 ± 0.02
$^3P_0$	1.150850	3.50 ± 0.21	13.17 ± 0.01
$^3P_1$			12.73 ± 0.02
$^3P_2$			12.07 ± 0.08

for the major, and $\log N = 13.33 \pm 0.01$ for the minor component. These values are consistent with the total column density $\log N = 13.90 \pm 0.04$ reported by de la Varga et al. (2000) for the nonseparated components.

Figure 1 reveals a saturated narrow structure in the $^3P_0$ line profiles of the major absorption component. This problem can be tackled indirectly by correcting the apparent optical depth (Savage & Sembach 1991; Jenkins 1996), but the correction procedure is only established for synthetic data and may not be applicable in general. Instead, we tackle the problem of saturated narrow structure directly by testing our analytical procedure with synthetic data similar to the observed spectrum (Fig. A.1). The tests confirm that our analytical procedure correctly recovers the narrow structure in the $^3P_0$ line profiles if the saturation is moderate (Table A.1). The presupposition of stronger saturation gives rise to observed fine-structure populations being far away from statistical equilibrium.

The optimized value of the spectral resolution of the instrument $R = 55\,500 \pm 1200$ matches the spectral resolution of the individual exposures.

4.2. Physical conditions

The ground state of the carbon atom consists of the $2s^2 2p^2$ $^3P_{0,1,2}$ fine-structure triplet levels. In DLA systems, the excited levels of the ground state triplet are principally populated by three competing processes: direct photoexcitation by the CMBR, fluorescence induced by the local FUV radiation field, and collisional excitation by hydrogen atoms (Bahcall & Wolf 1968). Given the physical conditions, the relative population of fine-structure levels is determined by solving the system of statistical equilibrium equations. In order to calculate the solution, we use the PopRatio program package recently developed by Silva & Viegas (2001). The package provides a Fortran 90 source code and an up to date compilation of atomic data (including collisional transition rate coefficients) for C^0, C^+, O^0, Si^+, and Fe^+.

The rate equation is established assuming that the temperature of the CMBR satisfies the standard temperature-redshift relation and the local FUV input conforms to the scaled generic Galactic radiation field. The transition rates resulting from direct photoexcitation by the CMBR at redshift $z = 1.15$ are $R_{01} = 4.3 \times 10^{-9}$ s^{-1} and $R_{02} = 2.5 \times 10^{-18}$ s^{-1}, while fluorescence (the PopRatio package considers 108 UV transitions) induced by the Galactic interstellar FUV radiation field (Draine & Bertoldi 1996) yields pumping rates of $P_{01} = 6.3 \times 10^{-10}$ s^{-1} and $P_{02} = 5.0 \times 10^{-10}$ s^{-1}. Considering a kinetic temperature of $T_{\rm kin} = 100$ K, the collisional transition rate coefficients are $\gamma_{01} = 3.8 \times 10^{-10}$ cm^3 s^{-1} and $\gamma_{02} = 2.5 \times 10^{-10}$ cm^3 s^{-1}. Note that the optical pumping rates will exceed the direct photoexcitation rates if the local FUV input exceeds the typical Galactic interstellar radiation by a factor of seven.

If the absorbing medium is homogenous, the relative population of excited and ground fine-structure levels matches the corresponding column density ratios, $X_{1,2} = N_{1,2}/N_0$. Then, if the column densities $N_{0,1,2}$ are regarded as independent random observables with density functions $p_{0,1,2}(N_{0,1,2})$, $X_{1,2}$ are random observables with cumulative distribution functions

$$F(X_{1,2}) = \int_0^\infty \int_0^{N_0 X_{1,2}} p_0(N_0) p_{1,2}(N_{1,2})\, {\rm d}N_{1,2}\, {\rm d}N_0. \quad (5)$$

Deriving the cumulative distribution functions with respect to $X_{1,2}$ yields the density functions

$$p(X_{1,2}) = \int_0^\infty p_0(N_0) p_{1,2}(N_0 X_{1,2}) N_0\, {\rm d}N_0. \quad (6)$$

In order to infer the physical conditions in each observed C I absorber, we define $p_{0,1,2}(N_{0,1,2})$ by the requirement that $\log N_{0,1,2}$ are normally distributed with mean values and standard deviations matching the optimized values listed in Table 2. Then, we calculate the equilibrium population $X_{1,2}$ for a grid of physical conditions and evaluate the joint density function

$$p(X_1, X_2) = p(X_1) p(X_2). \quad (7)$$

Contour diagrams of the joint density functions obtained in this way are shown in Fig. 2, considering a kinetic temperature of $T_{\rm kin} = 100$ K. Figure 2 clearly demonstrates that the CMBR is only a minor source of the observed fine-structure excitation. Considering the 0.01 contour line (i.e. the boundary of the 99.7 percent confidence region if the distribution were normal), the upper limit on the FUV energy density in the major (minor) C I absorber is 60 (30) times the Galactic interstellar value. The upper limit on the H^0 number density is 125 cm^{-3} (55 cm^{-3}). The upper limit on the thermal pressure of $P/k = 12\,500$ cm^{-3} K (5500 cm^{-3} K) exceeds the typical pressure in Galactic interstellar C I absorbers (Jenkins & Tripp 2001) by a factor of four

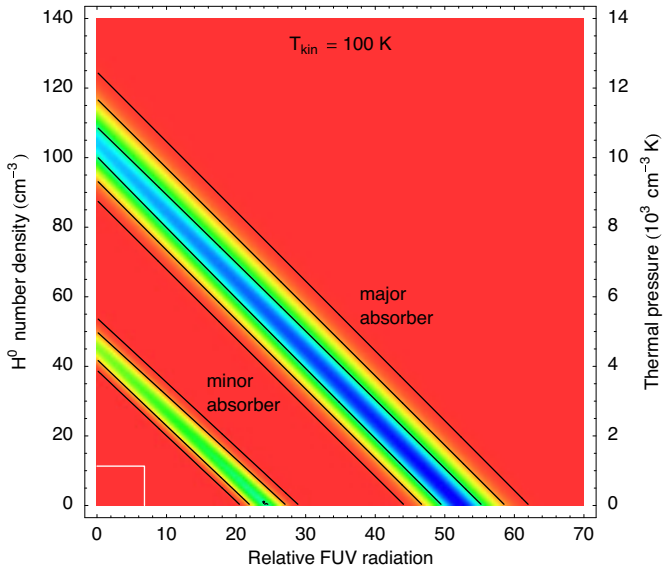

Fig. 2. Probability density of the physical conditions in the DLA system. The contour lines are drawn at 0.61, 0.14, and 0.01 of the maximum and would correspond to the boundaries of the 68.3, 95.4, and 99.7 percent confidence regions if the distributions were normal. The rectangle in the lower left corner marks the region where the CMBR is the principal source of the fine-structure excitation

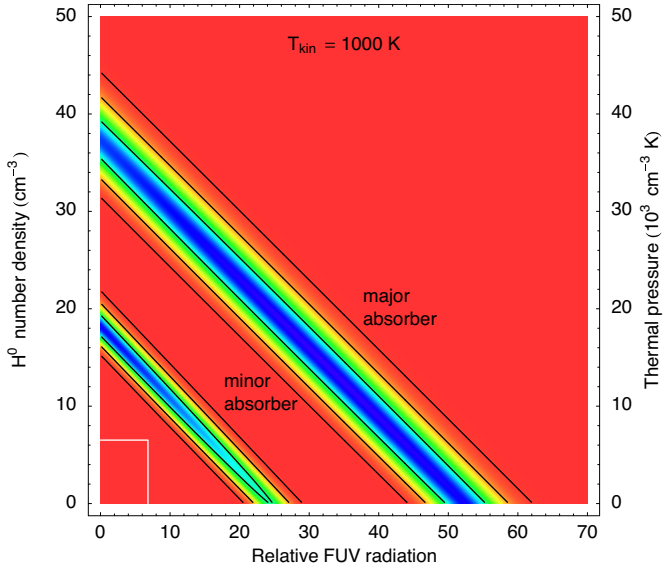

Fig. 3. The same as Fig. 2, but considering a ten times higher kinetic temperature. Note the different scale of the vertical axis

(two). A similar analysis considering a kinetic temperature of $T_{\rm kin}$ = 1000 K (see Fig. 3) yields upper limits of 44 cm^{-3} (22 cm^{-3}) and 44 000 cm^{-3} K (22 000 cm^{-3} K). If the CMBR is completely ignored in the analysis, the limits increase by less than 10 percent (Figs. B.1, B.2).

If we integrate the joint density function with respect to the H^0 number density and the relative FUV energy density, we obtain the marginal probability density of the kinetic temperature. The marginal density function cannot rule out any kinetic temperature in the range 10 K $\leq T_{\rm kin} \leq$ 1000 K at a confidence level higher than 95.4 percent, but indicates that in both C I absorbers kinetic temperatures of $T_{\rm kin} < 100$ K are more likely. Note that lower kinetic temperatures also result in physical conditions largely complying with the typical thermal pressure observed in Galactic interstellar C I absorbers (Fig. 4).

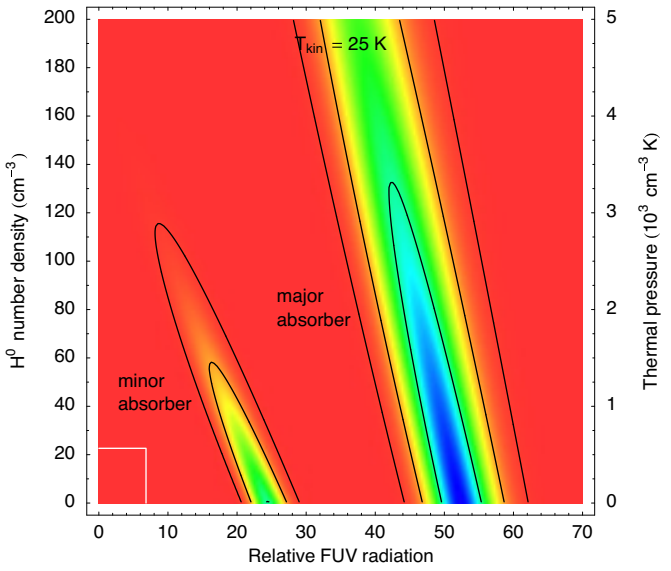

Fig. 4. The same as Fig. 2, but considering a four times lower kinetic temperature. Note the different scale of the vertical axis

Table 3. Observed excitation temperatures of the ground state fine-structure levels in C^0. The indices denote the J quantum numbers of the initial and final levels considered

Absorber	T_{01} (K)	T_{02} (K)	T_{12} (K)
Major	15.8 ± 0.8	18.6 ± 0.5	20.7 ± 0.6
Minor	11.2 ± 0.3	15.1 ± 0.6	19.1 ± 1.7

4.3. Excitation temperature

If the absorbing medium is homogenous, the excitation temperature is defined (via the Boltzmann equation) by the ratio of column densities

$$\frac{N_j}{N_i} = \frac{g_j}{g_i}\, {\rm e}^{-E_{ij}/(kT_{ij})}. \quad (8)$$

The energies of the first and second excited ground state fine-structure levels in C^0 relative to the ground level are E_{01} = 16.4 cm^{-1} and E_{02} = 43.4 cm^{-1}. Now considering the optimized column density values listed in Table 2, we obtain three different excitation temperatures for each C I absorber (see Table 3). These excitation temperatures are considerably higher than the CMBR temperature predicted by Eq. (1), $T_{\rm CMBR}(1.15) = 5.9$ K. The magnitude and diversity of the excitation temperatures reveals that the CMBR is not the principal source of the fine-structure excitation. Moreover, the excitation temperatures in the minor absorber are systematically lower, indicating completely different physical conditions. The fine-structure excitation temperatures derived in this and in previous studies considering higher redshifts are compared in Fig. 5.

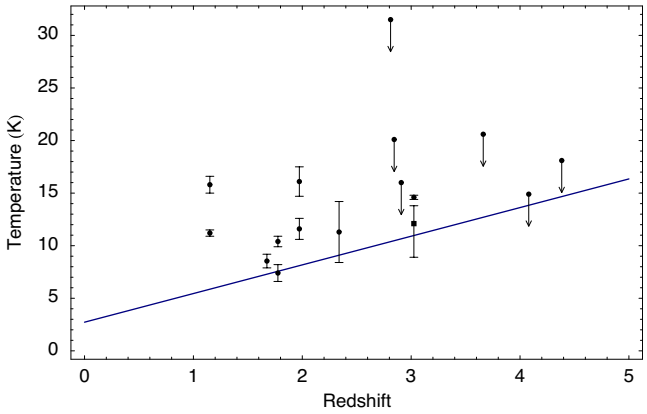

Fig. 5. Fine-structure excitation temperatures derived in this and in previous studies (Songaila et al. 1994; Lu et al. 1996; Ge et al. 1997; Roth & Bauer 1999; Srianand et al. 2000; Molaro et al. 2002). The square dot marks the CMBR temperature derived by Molaro et al. (2002), the solid line represents the prediction of the standard Friedmann cosmology

5. Conclusions

Our theoretical calculations of the relative population of the ground state fine-structure levels in C^0 clearly demonstrate that the CMBR is only a minor source of the observed fine-structure excitation. The ratios of observed column densities indicates that the absorbing medium is dense or exposed to intense FUV radiation. The upper limit on the local FUV energy density corresponds to the 60-fold Galactic radiation, while the number density of hydrogen atoms may reach some 100 cm^{-3}. Whether flourescence induced by local FUV radiation or collisional excitation by hydrogen atoms is the more important process cannot be concluded.

Besides, we observe absorption lines of molecular hydrogen associated with the DLA system. The observed rotational population is strongly inversed, indicating not only collisonal but also radiative excitation. Therefore, the kinetic temperature of the absorbing medium can only be determined in a multi-level population analysis. The analysis is in progress and might unravel the physical processes giving rise to the observed fine-structure population.

Acknowledgements. We kindly acknowledge A. I. Silva and S. M. Viegas for providing the PopRatio program package for the public. We also thank N. Hansen for giving further information on evolution strategies. This research has been supported by the Verbundforschung of the BMBF/DLR under Grant No. 50 OR 9911 1.

References

Bahcall, J. N. & Wolf, R. A. 1968, ApJ, 152, 701
Ballester, P., Modigliani, A., Boitquin, O., et al. 2000, ESO Mess., 101, 31
de la Varga, A., Reimers, D., Tytler, D., Barlow, T., & Burles, S. 2000, A&A, 363, 69
Draine, B. T. & Bertoldi, F. 1996, ApJ, 468, 269
Ge, J., Bechtold, J., & Black, J. H. 1997, ApJ, 474, 67
Ge, J., Bechtold, J., & Kulkarni, V. P. 2001, ApJ, 547, L1
Hansen, N. & Ostermeier, A. 2001, Evol. Comput., 9, 159
Jenkins, E. B. 1996, ApJ, 471, 292
Jenkins, E. B. & Tripp, T. M. 2001, ApJS, 137, 297
Lu, L., Sargent, W. L. W., Barlow, T. A., Churchill, C. W., & Vogt, S. S. 1996, ApJS, 107, 475
Mather, J. C., Fixsen, D. J., Shafer, R. A., Mosier, C., & Wilkinson, D. T. 1999, ApJ, 512, 511
Molaro, P., Levshakov, S. A., Dessauges-Zavadsky, M., & D'Odorico, S. 2002, A&A, 381, L64
Morton, D. C. 2003, ApJS, 149, 205
Reimers, D., Hagen, H.-J., Rodriguez-Pascual, P., & Wisotzki, L. 1998, A&A, 334, 96
Roth, K. C. & Bauer, J. M. 1999, ApJ, 515, L57
Savage, B. D. & Sembach, K. A. 1991, ApJ, 379, 245
Silva, A. I. & Viegas, S. M. 2001, Comput. Phys. Commun., 136, 319
Silva, A. I. & Viegas, S. M. 2002, MNRAS., 329, 135
Songaila, A., Cowie, L. L., Hogan, C. J., & Rugers, M. 1994, Nature, 368, 599
Srianand, R., Petijean, P., & Ledoux, C. 2000, Nature, 408, 931

Online Material

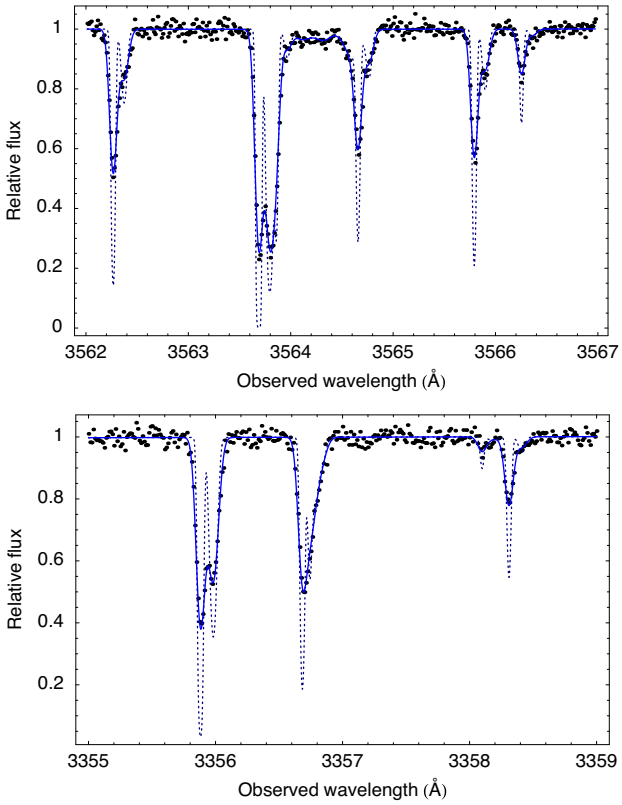

Fig. A.1. Synthetic data similar to the observed spectrum. As a precaution, the simulated spectral resolution (50 000) and the effective signal-to-noise ratio (50) are less than in the observed spectrum

Table A.1. Parametrization of the sythetic spectra shown in Fig. A.1. Optimized parameter values are indicated in parentheses

Level	z	b (km s^{-1})	log N (cm^{-2})
$^3P_0$	1.150780 (0)	1.80 (1.89 ± 0.06)	13.60 (13.58 ± 0.02)
$^3P_1$			13.40 (13.40 ± 0.01)
$^3P_2$			12.90 (12.91 ± 0.01)
$^3P_0$	1.150844 (5)	3.20 (3.12 ± 0.12)	13.30 (13.29 ± 0.01)
$^3P_1$			12.80 (12.79 ± 0.02)
$^3P_2$			12.20 (12.07 ± 0.05)

Appendix A: Recovering saturated narrow lines

In general, results based on the decomposition of saturated narrow lines are to be interpreted with caution. Nevertheless, the application of the analysis technique described in Sect. 3 to synthetic data similar to the observed spectrum (see Fig. A.1) results in the correct recovery of the saturated narrow lines, demonstrating that the saturated narrow structure in the observed spectrum is not problematic (see Table A.1).

Appendix B: Ignoring the CMBR

The observed fine-structure excitation can be explained even if the CMBR is ignored completely. Figures B.1 and B.2 demonstrate that the physical conditions are virtually unaffected by the CMBR.

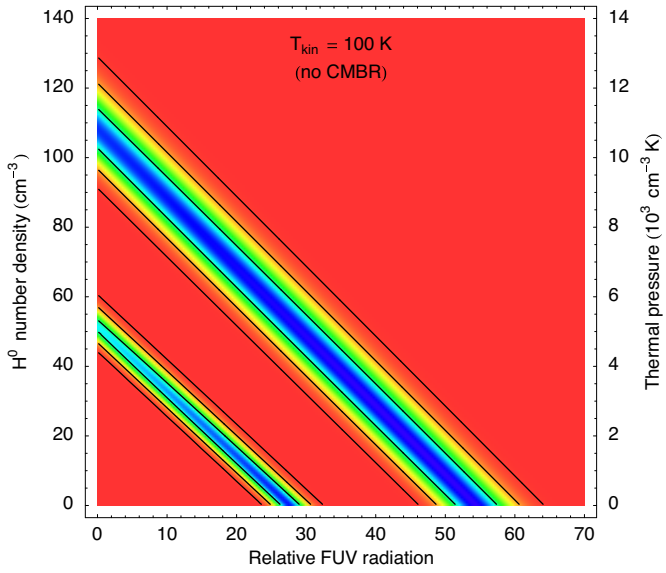

Fig. B.1. The same as Fig. 2, but ignoring the presence of the CMBR

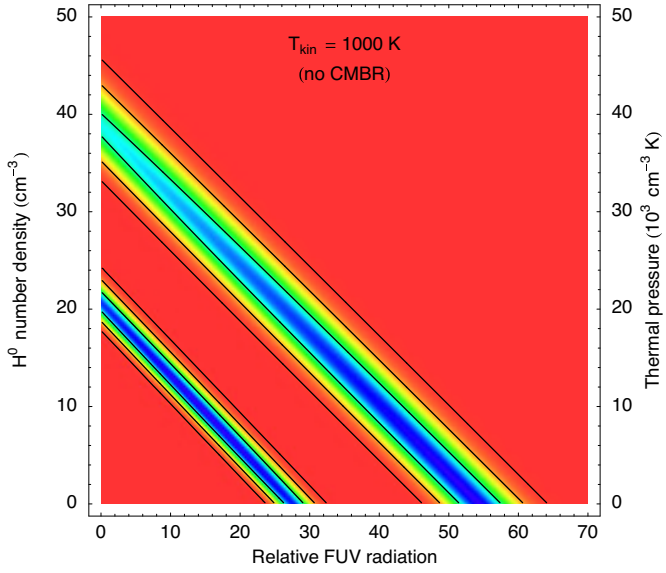

Fig. B.2. The same as Fig. 3, but ignoring the presence of the CMBR

Appendix C: The rate equation

The following remarks describe the way the PopRatio package establishes the rate equation. The rates of processes involving free states such as ionization or recombination are assumed to be much lower than the rates of processes involving only bound states and all transitions are assumed to be optically thin.

C.1. Radiative transition rates

Considering two atomic energy levels $E_i < E_j$ with multiplicities g_i and g_j, there are three different radiative processes connecting the two levels:

1. An atom in the higher level j may undergo a spontaneous transition to the lower level i while emitting a photon of energy $h\nu_{ij}$. The probability of this occurring in unit time

is defined by the Einstein coefficient A_{ji}. If n_j denotes the number density of atoms in level j, the expected number of spontaneous transitions from level j to level i per unit time and volume is $n_j A_{ji}$.

2. In the presence of radiation of energy density U, an atom in the higher level j may undergo stimulated emission to the lower level i. The corresponding transition rate is $B_{ji}U(\nu_{ij})$ with
$$B_{ji} = \frac{c^3}{8\pi h\nu_{ij}^3} A_{ji} \tag{C.1}$$
giving rise to another $n_j B_{ji} U(\nu_{ij})$ downward transitions per unit time and volume.
3. In the presence of radiation of energy density U, an atom in the lower level i may jump to the higher level j while absorbing a photon of energy $h\nu_{ij}$. The corresponding transition rate is $B_{ij}U(\nu_{ij})$, where
$$B_{ij} = \frac{g_j}{g_i} B_{ji}. \tag{C.2}$$
If n_i denotes the number density of atoms in level i, the expected number of transitions from level i to level j per unit time and volume is $n_i B_{ij} U(\nu_{ij})$.

C.2. Collisional transition rates

Considering an atom moving in a group of field particles with number density n, the probability per unit time that the atom undergoes a transition from level i to level j as the result of a collision with a field particle is $C_{ij} = n\gamma_{ij}$. The collisional rate coefficient γ_{ij} is calculated as

$$\gamma_{ij} = \int \boldsymbol{u} \cdot \boldsymbol{\sigma}_{ij}(\boldsymbol{u}) f(\boldsymbol{u})\, \mathrm{d}\boldsymbol{u}, \tag{C.3}$$

where $f(\boldsymbol{u})$ is the velocity distribution function for the group of field particles and $\boldsymbol{\sigma}_{ij}(\boldsymbol{u})$ is the cross section of a single field particle. In the interstellar or intergalactic medium, the transfer of translational kinetic energy is easily dominated by elastic collisonal processes and the calculation of γ_{ij} is basically simplified by the fact that the velocity distributions of atoms, electrons, and molecules are closely Maxwellian, with a single kinetic temperature T applicable to all these components. Consequently, the collisional rate coefficient γ_{ij} and its reverse γ_{ji} are related by the principle of detailed balance resulting in

$$g_i \gamma_{ij} = g_j \gamma_{ji}\, \mathrm{e}^{-(E_j - E_i)/(kT)}. \tag{C.4}$$

The PopRatio package provides an up to date compilation of transition rate coefficients for collisions of C^0, C^+, O^0, Si^+, and Fe^+ with electrons, protons, atomic and molecular hydrogen, and helium.

C.3. Statistical equilibrium

Cumulating the transition rates resulting from collisions with all kinds of field particles $C_{ij} = \sum_k n_k (\gamma_{ij})_k$ and defining $R_{ij} = A_{ij} + B_{ij} U(\nu_{ij})$ with $A_{ij} \equiv 0$ if $E_i < E_j$, the equation of statistical equilibrium for level i reads

$$\sum_{j \neq i} n_j \left(R_{ji} + C_{ji} \right) - n_i \sum_{j \neq i} \left(R_{ij} + C_{ij} \right) = 0. \tag{C.5}$$

In the case of flourescence, a photo-excited atom cascades back through a variety of intermediate states, reaching states which eventually cannot be populated by direct upward radiative transitions from the ground state. In this situation the relevant energy levels may be divided into two sets, lower levels $\mathbb{L}^-$ and upper levels $\mathbb{L}^+$. By definition, the downward radiative transitions from the upper levels to one or more of the lower levels occur so rapidly that the population of the upper levels relative to the lower levels at any one time is negligibly small. In addition, the retention period in each upper level is so short that collisional transitions out of each such level can be ignored. Consequently, considering only the population of the lower levels reduces the equation of statistical equilibrium for level $i \in \mathbb{L}^-$ to

$$\sum_{\substack{j \in \mathbb{L}^- \\ j \neq i}} n_j \left(R_{ji} + P_{ji} + C_{ji} \right) - n_i \sum_{\substack{j \in \mathbb{L}^- \\ j \neq i}} \left(R_{ij} + P_{ij} + C_{ij} \right) = 0, \tag{C.6}$$

where $P_{ij} = \sum_{k \in \mathbb{L}^+} R_{ik} \epsilon_{kj}$ defines the indirect transition rate from the lower level i to the lower level j. The quantity ϵ_{kj} is the fraction of downward transition cascades from the upper level k that first of all lower levels populate the level j. In the absence of radiative cascading among intermediate upper levels ϵ_{kj} simply is the branching ratio, $\epsilon_{kj} = R_{kj} / \sum_{i \in \mathbb{L}^-} R_{ki}$. Defining

$$Z_{ii} = -\sum_{j \neq i} \left(R_{ij} + P_{ij} + C_{ij} \right), \quad Z_{ij} = R_{ji} + P_{ji} + C_{ji}, \tag{C.7}$$

Eq. (C.6) provides a homogenous set of linear equations

$$\begin{pmatrix} \vdots & & \vdots & \\ \cdots & Z_{ii} & \cdots & Z_{ij} & \cdots \\ \vdots & & \vdots & \\ \cdots & Z_{ji} & \cdots & Z_{jj} & \cdots \\ \vdots & & \vdots & \end{pmatrix} \begin{pmatrix} \vdots \\ n_i \\ \vdots \\ n_j \\ \vdots \end{pmatrix} = 0, \quad i, j \in \mathbb{L}^- \tag{C.8}$$

which can be solved in general by means of standard methods such as singular value decomposition.

Submitted manuscript. Article reference number AA/2005/4773

An unusual sub-damped Ly α system revisited[⋆,⋆⋆]

R. Quast, D. Reimers, and R. Baade

Hamburger Sternwarte, Universität Hamburg, Gojenbergsweg 112, D-21029 Hamburg, Germany
e-mail: {rquast,dreimers,rbaade}@hs.uni-hamburg.de

Received 24 December 2005

ABSTRACT

Aims. We examine the ionization, abundances, and differential dust depletion of metals, the kinematic structure, and the physical conditions in the molecular hydrogen-bearing sub-damped Ly α system toward HE 0515-4414.
Methods. We used the STIS and VLT UVES spectrographs to obtain high-resolution recordings of the damped Ly α profile and numerous associated metal lines. Observed element abundances are corrected with respect to dust depletion effects.
Results. The sub-damped Ly α absorber at redshift $z = 1.15$ is unusual in several aspects. The velocity interval of associated metal lines extends for 700 km s^{-1}. In addition, two peripheral H I components with $N_{\rm H\,I} = 10^{15}$ and 10^{17} cm^{-2} are detected at distances of, respectively, 530 and 240 km s^{-1} from the $N_{\rm H\,I} = 8\times10^{19}$ cm^{-2} main component. For the peripheral components, the column density ratios of observed Al II, Fe II, and H I lines indicate that the absorbing material is ionized. Most of the 31 associated metal line components are formed within the peripheral H II regions, only components 20–31 are associated with the main absorber and correspond to predominantly neutral gas. The bimodal kinematic distribution of metal line components suggests two interacting absorbers. For components 23–28 the observed abundance ratios of refractory elements to Zn range from Galactic warm disk $[{\rm Si/Zn}]_{\rm g} = -0.40\pm0.06$, $[{\rm Fe/Zn}]_{\rm g} = -1.10\pm0.05$ to halo-like and essentially undepleted patterns. The dust-corrected metal abundances indicate the nucleosynthetic odd-even effect and might imply an anomalous depletion of Si relative to Fe for two components, but otherwise do correspond to solar ratios. The intrinsic average metallicity is almost solar $[{\rm Fe/H}]_{\rm m} = -0.08 \pm 0.19$, whereas the uncorrected average is $[{\rm Zn/H}]_{\rm g} = -0.38 \pm 0.04$. The ion abundances in the periphery conform with solar element composition.
Conclusions. The unambiguous detection of H II gas as well as the large variation in dust depletion for this sight line raises the question whether in future studies of damped Ly α systems ionization and depletion effects have to be considered in further detail. Ionization effects, e.g., may pretend the enrichment of α elements. An empirical recipe to detect H II regions is provided.

Key words. cosmology: observations - galaxies: abundances - galaxies: interactions – intergalactic medium – quasars: absorption lines – quasars: individual: HE 0515–4414

1. Introduction

The study of QSO absorption lines provides vital information on the nucleosynthetic history of the universe by complementing the compositional analysis of stars and interstellar space in local galaxies with element abundances at higher redshift. In particular, interests are focused on extragalactic structures termed damped Ly α (DLA) systems, essentially comprised of neutral hydrogen with column densities $N_{\rm H\,I} \geq 2 \times 10^{20}$ atoms cm^{-2} (for a review see Wolfe et al. 2005). Absorbers in the sub-DLA range with column densities $N_{\rm H\,I} \geq 10^{19}$ atoms cm^{-2} might be mainly neutral when the ionizing background is reduced (Péroux et al. 2002, 2003). The aim of these examinations is to establish accurate element abundances for the aggregations of neutral gas that are examples of interstellar environments in the high-redshift universe. Since the measurement of metal column densities is straightforward, the only problem is their correct interpretation.

The true nature of DLA systems is unknown and the underlying population, being constituted of hierarchical structures with different morphologies, chemical enrichment histories, and physical environments, is multifarious. The diversity is attested by the disparate values obtained for metal abundances at any given redshift.

The metallicity of DLA systems is not correlated with their column density. Though there exist high column density DLA absorbers with high metallicity in the foreground of the star forming hosts of gamma-ray bursts (Watson et al. 2005), corresponding absorbers are not detected toward QSOs. The cosmic mean metallicity of DLA absorbers increases with cosmic time (Prochaska et al. 2003; Kulkarni et al. 2005; Rao et al. 2005), but is an order of magnitude lower than predicted by cosmic star formation history (see the discussion of the missing met-

Send offprint requests to: R. Quast

⋆ Based on observations made with ESO Telescopes at the La Silla or Paranal Observatories under programme ID 066.A-0212.

⋆⋆ Based on observations made with the NASA/ESA Hubble Space Telescope, obtained from the data archive at the Space Telescope Institute. STScI is operated by the association of Universities for Research in Astronomy, Inc. under the NASA contract NAS 5-26555.

als problem by Wolfe et al. 2005). The solution to this problem is a matter of debate. Conclusive evidence of enriched material ejected from DLA absorbers into the intergalactic medium or of active star formation restricted to compact regions is missing. The latter possibility is closely linked to the physical properties of the interstellar medium and its molecular content (Wolfe et al. 2003a,b). Molecular gas is uncommon in DLA absorbers. If found, the fraction of molecular hydrogen, usually between 10^{-6} and 10^{-2}, is not correlated with the column density of atomic hydrogen (Ledoux et al. 2003).

Since the spectroscopic analysis is restricted to the gaseous phase of the absorbing medium, observed element abundances are potentially distorted by dust removing atoms in varying amounts, depending on their affinity to the solid state. In particular high-metallicity and molecule-bearing absorbers are affected by dust (Petijean et al. 2002; Ledoux et al. 2003). Depletions are largely lower than in the Galactic halo, but increase with metallicity (Vladilo 2004). In practice, the observed element abundances are corrected ad hoc, using Galactic interstellar depletion patterns as reference (Vladilo 2002a,b). Another aspect of dust is the possibility that DLA absorbers may elude detection because the background QSOs are obscured (Fall & Pei 1993). The selection effects are complicated since obscurement is counteracted, but not compensated, by amplification due to gravitational lensing (Smette et al. 1997). The effect of dust is subject of several studies (Murphy & Liske 2004; Quast et al. 2004; Akerman et al. 2005; Smette et al. 2005; Vladilo & Péroux 2005; Wild et al. 2005). A further difficulty are ionization effects. Examples of DLA-associated metal line components formed within mainly ionized material are given by Prochaska et al. (2002) and Dessauges-Zavadsky et al. (2006).

The column density distribution and kinematic structure of absorbers provide important constraints on hierarchical structuring (e.g. Cen et al. 2003; Nagamine et al. 2004) and immediate insight into processes of galaxy formation (Wolfe & Prochaska 2000). The extended multicomponent velocity structure and characteristic asymmetry of DLA-associated metal lines is consistent with galaxy formation models in hierarchic cold dark matter cosmologies, and reproducible by the hydrodynamical simulation of rotation, random motion, infall, and merging of irregular protogalactic clumps hosted by collapsed dark matter halos (Haehnelt et al. 1998). The velocity structure of sub-DLA absorbers compares to that of the higher column density systems (Péroux et al. 2003), which is unexpected since semianalytic galaxy formation models (Maller et al. 2001, 2003) predict markedly different kinematic properties. The absorption velocity intervals of both sub-DLA and DLA absorbers typically extend for 100 km s^{-1}. More extended systems tend to higher metallicities and lower column densities (Wolfe & Prochaska 1998). In particular the latter property is unexpected and difficult to interprete in terms of rotating disks models. The most extended systems, however, are probably due to interacting or merging galaxies (Petijean et al. 2002; Richter et al. 2005).

In this study we revisit the $z = 1.15$ sub-DLA system toward HE 0515–4414 (Reimers et al. 1998; de la Varga et al. 2000). The main components of associated metal lines exhibit excited neutral carbon and molecular hydrogen (Quast et al. 2002; Reimers et al. 2003). Most outstanding, the absorption velocity interval extends for 700 km s^{-1}. Based on refined spectroscopy, we examine the ionization, abundances, and differential dust depletion of metals, the kinematic structure, and the physical conditions in this unusual absorption line system. Its extended velocity spread facilitates the component-wise comparison of H I and associated metal lines. The comparison reveals that more than half of the metal line components are formed within H II regions.

Table 1. Spectra obtained with UVES

Date	Obs.	Exp. (s)	Mode	Arm	Wav. (Å)
2000-10-07	101818	4500	DI2	blue	3460
		4499		red	8600
2000-11-16	101822	4500	DI1	blue	3460
		4499		red	5800
2000-11-17	101821	4500	DI1	blue	3460
		4499		red	5800
2000-11-18	101820	4500	DI1	blue	3460
		4499		red	5800
2000-12-15	101812	3600	DI2	blue	4370
		3599		red	8600
	101813	3600	DI2	blue	4370
		3600		red	8600
	101814	3600	DI2	blue	4370
		3599		red	8600
2000-12-16	101811	3600	DI2	blue	4370
		3600		red	8600
2000-12-21	101810	3600	DI2	blue	4370
		3599		red	8600
	101815	3600	DI2	blue	4370
		3599		red	8600
2000-12-23	101817	4500	DI2	blue	3460
		4500		red	8600
2000-12-24	101819	4500	DI1	blue	3460
		4500		red	5800
2001-01-02	101816	4500	DI2	blue	3460
		4500		red	8600

2. Observations

Ranging from the NUV to the end of the visual, the observations cover the sub-damped profile at 2615 Å (Fig. 1) and numerous associated metal lines (Fig. 2).

2.1. UV-visual spectroscopy

HE 0515–4414 was observed during ten nights between October 7, 2000 and January 3, 2001, using the UV-Visual Echelle Spectrograph (UVES) installed at the second VLT Unit Telescope (Kueyen). Thirteen exposures were made in the dichroic mode using standard settings for the central wavelenghts of 3460/4370 Å in the blue, and 5800/8600 Å in the red (Table 1). The CCDs were read out in fast mode without binning. Individual exposure times were 3600 and 4500 s, under photometric to clear sky and seeing conditions ranging from 0.47 to 0.70 arcsec. The slit width was 0.8 arcsec pro-

viding a spectral resolution of about 55 000 in the blue and slightly less in the red. The raw data frames were reduced at the ESO Quality Control Garching using the UVES pipeline Data Reduction Software. Finally, the individual vacuum-barycentric corrected spectra were combined resulting in an effective signal-to-noise ratio per pixel of 90–140.

2.2. NUV spectroscopy

The UV-visual recordings were supplemented by spectra obtained with the Space Telescope Imaging Spectrograph (STIS) during three orbits between January 31 and February 1, 2000, ranging from 2300 to 3100 Å. The total exposure time was 31 500 s, while the instrument was operating in the medium resolution NUV mode (E230M) with the entrance aperture of $0\farcs2 \times 0\farcs2$ providing a spectral resolution of about 30 000. The raw spectra were reduced at the Space Telescope Science Institute using the STIS pipeline software completed by an additional interorder background correction. The combined spectra show an effective signal-to-noise ratio per pixel of 5–10.

3. Line profile analysis

There are several basically different techniques for the analysis of QSO absorption lines: the classical line profile decomposition, the apparent optical depth method (Savage & Sembach 1991), and Monte Carlo inversion (Levshakov et al. 2000). While the classical profile decomposition postulates discrete homogenous absorbers with Gaussian (i.e. thermal or microturbulent) particle velocity distributions, the apparent optical depth technique allows the very direct interpretation of observed spectra without the need to consider the velocity structure of spectral lines as long as the absorption is optically thin or sufficiently resolved. Otherwise, the apparent optical depth is not representative and additional operations are required to recover the correct column density (Jenkins 1996). The corrective procedure, however, is only approved for synthetic spectra with Gaussian velocity distributions underlying the individual components. Monte Carlo inversion considers random velocity and density fields along the sight line, but requires photoionization calculations to connect the random fields to the observed absorption that are too time-consuming for DLA systems.

Since we consider many blended or optically thick lines, we prefer the classical decomposition technique for the analysis and use the apparent optical depth method to supplement the diagnostics. Throughout the analysis we use the atomic data compiled by Morton (2003).

3.1. Line profile decomposition

The general problem of line profile decomposition in QSO spectra and its solution by means of evolutionary forward modelling is described in detail by Quast et al. (2005). For the specific purpose of measuring accurate metal column densities we introduce several additional constraints:

1. Each metal line component is modelled by a superposition of Doppler profiles positioned at the same radial velocity. This procedure helps to recover the velocity structure of the instrumentally blurred line ensembles and ensures the calculation of elemental abundances for concentric velocity intervals.
2. For any component all lines corresponding to the same atomic or ionic species are modelled by Doppler profiles exhibiting the same broadening velocity and column density. With respect to their broadening velocities all Cr II, Mn II, Fe II, Ni II, and Zn II lines are modelled as if corresponding to the same ionic species. The same treatment is applied to Al II and Al III lines.
3. Unresolved blends or otherwise asymmetric lines are modelled by a single component.
4. Weak absorption features otherwise unconfirmed are ignored.

All metal line ensembles are decomposed simultaneously while the local background continuum is approximated by an optimized linear combination of Legendre polynomials extending to the nearest absorption-free regions. The metal line recordings of STIS are too noisy and too contaminated with Lyman forest lines to be considered in the decomposition. The STIS echelle order showing the sub-damped profile is decomposed using pseudo-Voigt profiles (Ida et al. 2000). The profile is well defined by its Lorentzian part and can be distinguished from even a curved background continuum due to its symmetry. Note that the blue damping wing is blended with further H I components which are modelled by two profiles of the same width and are positioned in accord with the main associated metal line components (Fig. 1).

3.2. Apparent optical depth analysis

The apparent optical depth method is only applied to the weaker transitions of a given atomic or ionic species to avoid narrow saturation. The spectra are normalized using the optimized continuum approximation obtained from the line profile decomposition. The normalized flux is averaged using a moving window of 10 $\mathrm{km\,s^{-1}}$. Low apparent optical depths $\tau_a \leq 0.01$ are clipped.

4. Results and discussion

In this section we present the optimized profile decomposition and examine the ionization, chemical composition and dust content, kinematic structure, and physical conditions in the absorbing medium.

4.1. Profile decomposition

The optimized decomposition of the sub-damped Ly α profile and associated metal lines is depicted in Figs. 1–4. The corresponding line parameters are listed in Tables 2 and 3. Since only the metal line components 20–31 are associated with the sub-damped profile, components 1–19 and 20–31 are termed peripheral and main components, respectively. In particular, components 23 and 24 correspond to the neutral carbon and

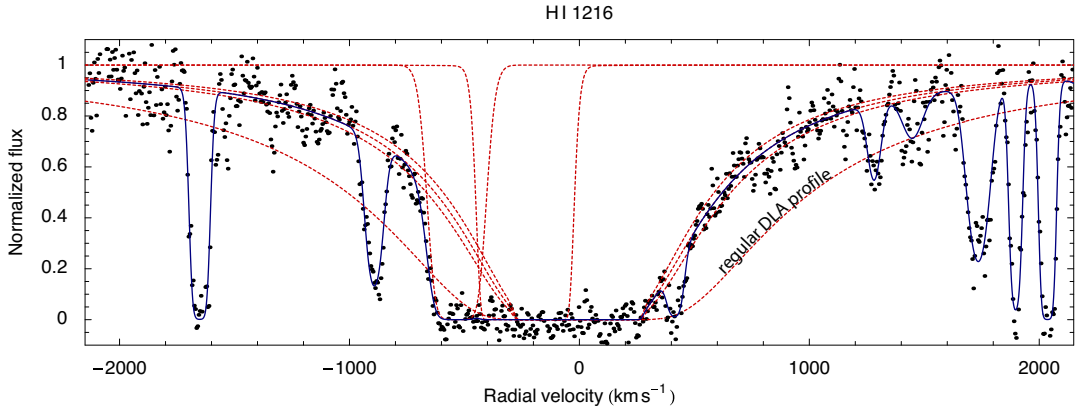

Fig. 1. STIS echelle order showing the sub-damped H I profile with redshift $z = 1.15$. The solid curve indicates the optimized profile decomposition of the spectrum, while the dashed curves mark individual line profiles. The blue damping wing is blended with further components associated with numerous metal lines (Fig. 2). The origin of the radial velocity axis corresponds to the redshift $z = 1.15080$

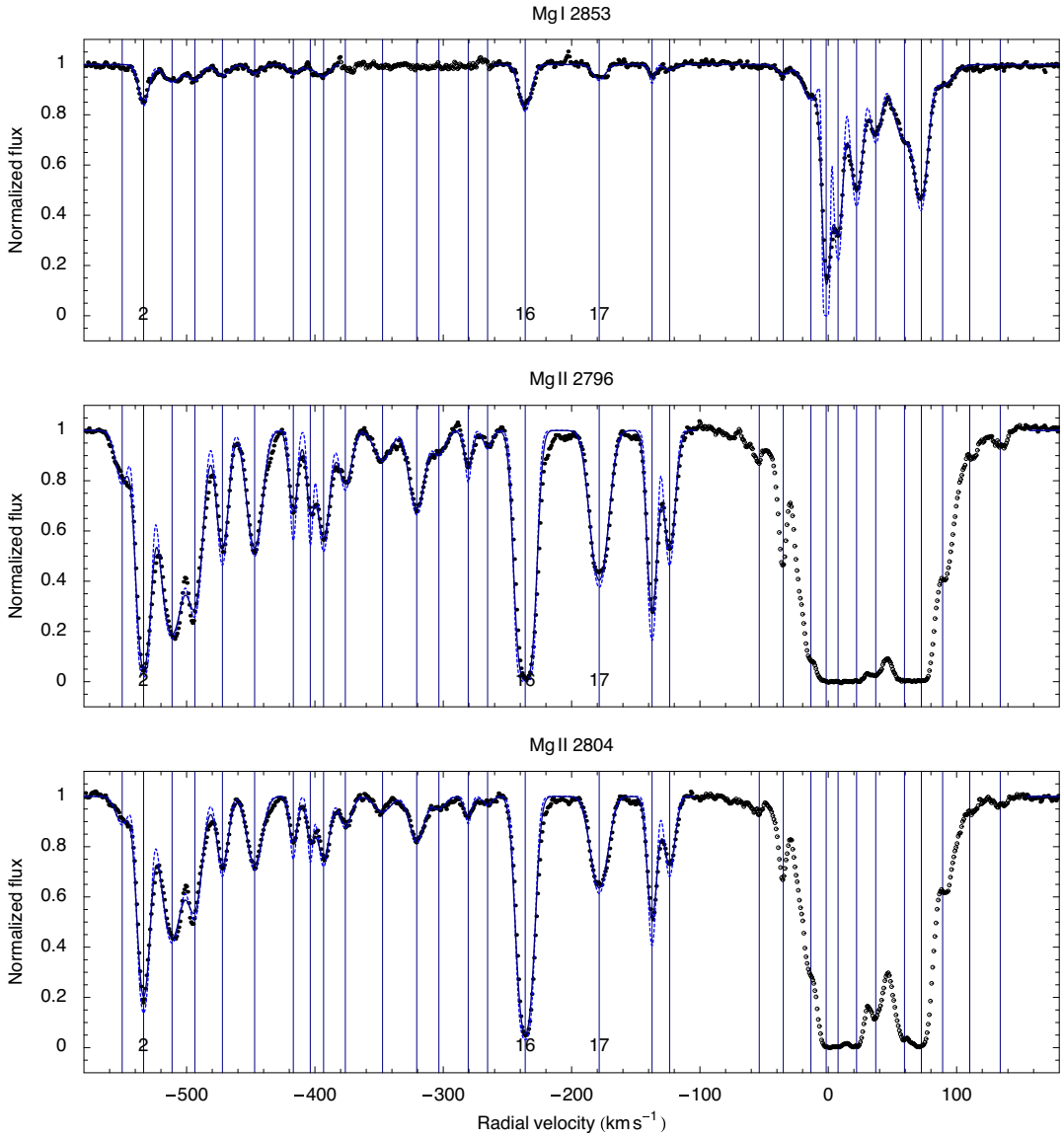

Fig. 2. Metal lines associated with the sub-damped profile shown in Fig. 1. The dashed and solid curves indicate the optimized profile decomposition and its instrumental convolution. Individual components are marked by vertical lines. Data represented by empty circles are ignored in the profile decomposition. Components 3, 16, and 17 are probably unresolved blends. This figure is continued in the Online Material

Table 2. Optimized decomposition of the sub-damped profile shown in Fig. 1. The listed numbers correspond to a straight continuum, for a curved continuum the errors increase. The origin of the radial velocity (RV) scale corresponds to the redshift $z = 1.15080$

Transition	RV (km s^{-1})	b (km s^{-1})	log N (cm^{-2})
H I 1216	−533.51	82.74 ± 7.23	14.98 ± 0.13
H I 1216	−236.14	82.74 ± 7.23	16.84 ± 0.92
H I 1216	−3.19 ± 11.14	75.17 ± 5.84	19.89 ± 0.03

H_2-bearing components considered by Quast et al. (2002) and Reimers et al. (2003).

4.1.1. Peripheral components 1–19

The decomposition of the peripheral components is defined by the structure of Mg I, Mg II, Si II, and Fe II lines. Part of the Si II profile is ignored due to contamination by Lyman forest lines. The weakest components with 10^{11} metal ions cm^{-2} are indicated by the Mg II lines, whereas the components exceeding 10^{13} ions cm^{-2} are saturated for Mg II, but well defined for Fe II. Nonetheless, the decomposition is uncertain in detail, since components 3, 16, and 17 are probably unresolved blends. The ambiguities, however, do not affect the chemical abundance analysis.

For some components the Fe II lines are narrower than those corresponding to lighter elements as if thermally broadened. The constraints on the decomposition of Fe II, however, are much stronger than those on the rest of lines. The evidence of thermal broadening is therefore not conclusive.

4.1.2. Main components 20–31

The decomposition of the main components is well constrained by the structure of Mg I, Si II, Ca II and Fe II lines. The Mg II lines are saturated, with column densities exceeding 2×10^{13} ions cm^{-2}. The Al II line is ignored because it is blended with a lower-redshift Mg II system at $z = 0.28$.[1] Though the blended line ensemble can be disentangled, the optimized column densities calculated for components 23 and 24 are not reliable since the superimposed narrow Mg II absorption is saturated. The Si II λ1527 line is saturated for components 23 and 24, but the optically thin Si II λ1808 absorption compensates the lack of information. The red part of the Zn II λ2026 line is blended with the blue part of Mg I λ2026, but due to the distinct Mg I λ2853 absorption both ensembles can be restored. Similarly, the red part of the Cr II λ2062 line is blended with the blue part of Zn II 2063, but Cr II λ2056 and the blue part of Zn II λ2026 are unperturbed.

For the H_2-bearing components 23 and 24 the broadening velocity is correlated with the ionization potential of the absorbing species as if the ionizing radiation was spatially fluctuating. The lines corresponding to species with lower first ionization potential than hydrogen (C I, Mg I and Ca II) are systematically less broadened than the Si II and Fe II lines, indicating different spatial origins. This systematic difference is well known from the study of Galactic molecular gas (Spitzer & Jenkins 1975, Fig. 2). Indeed, the detection of Si I, S I, and Fe I lines with low broadening velocities (Table 3) may indicate an embedded layer of cold neutral gas.

[1] We cannot confirm the detection of Mn II lines associated with this DLA system candidate (de la Varga et al. 2000).

4.2. Ionization

For most elements, the singly ionized state predominates in the neutral interstellar medium because the first ionization potential is lower, whereas the second is higher than the hydrogen ionization threshold. Exceptions to this rule are N, O, and Ar, where the first ionization potential exceeds the threshold, and Ca, where even the second ionization potential is lower. Since for interstellar abundance studies the total amount of an element is usually assumed to be equal to the amount existing in the predominant stage of ionization, substantial errors are made if the absorbing medium is a mixture of H I and H II regions.

4.2.1. Peripheral components

Immediate evidence of ionized gas is provided by the detection of C IV lines (Fig. 2) and the recording of Si III and Si IV lines with STIS (see Fig. 5 provided in the Online Material). For all high-ion lines apparent column densities of 10^{13} cm^{-2} are attained. Except for the broad C IV lines, the velocity structures of low- and high-ion profiles are similar, suggesting a common spatial origin. In particular for components 2–4 the apparent column densities of different Si ions compare, clearly indicating an H II region. The apparent optical depths of the Si III and Si IV lines decreases for components 7–16, whereas the optical depth of Si II peaks at component 16. The optically thick Si III profile between components 19 and 20 indicates ionization, but an absorption within this velocity interval is not confirmed by the rest of metal lines.

Further evidence of ionized gas is provided by the column density ratios of Al II, Al III, Fe II lines. For components 2–4, 6, 12, 16, and 18 the apparent abundance of Al relative to Fe is a factor of 4–30 higher than expected for a neutral medium with solar chemical composition (Fig. 6). The apparent enrichment of Al cannot be explained by the presence of dust because the expected depletion of Al into grains is typically an order of magnitude higher than that of Fe (Spitzer & Jenkins 1975). On the other hand, Al is produced with α-elements which are known to experience a nucleosynthetic history different from that of Fe. For instance, in Galactic thick disk stars the abundance ratio of Al to Fe is found to be enhanced by a factor of 2–4 relative to the solar value (Prochaska et al. 2000). Nonetheless, the apparent enrichment of Al is correlated with the column density ratio of Al III to Al II lines, indicating ionization rather than nucleosynthetic effects (Fig. 6). This indication is absolutely confirmed by another argument: for components 2–4 the total column density of Fe II lines of about 5×10^{12} cm^{-2} implies a column density exceeding 10^{17} hydrogen atoms cm^{-2} if the medium were mainly neutral. Dust depletion or subsolar abundances would result in even higher values. In marked con-

Table 3. Optimized decomposition of the metal lines shown in Figs. 2 and 3. This list is abridged for convenience, the complete table is available in the Online Material

No.	Transitions		RV (km s^{-1})	b (km s^{-1})	log N (cm^{-2})
23	Mg I	2026, 2853	−1.61 ± 0.03	2.16 ± 0.05	12.41 ± 0.03
23	Al II	1671	−1.61	3.05	13.86 ± 0.17
23	Al III	1855, 1863	−1.61	3.05	11.50 ± 0.06
23	Si I	2515	−1.61 ± 0.03	2.17 ± 2.10	11.34 ± 0.08
23	Si II	1527, 1808	−1.61 ± 0.03	3.05 ± 0.09	14.28 ± 0.03
23	S I	1807	−1.61 ± 0.03	1.56 ± 1.12	12.18 ± 0.05
23	Ca II	3935	−1.61 ± 0.03	2.15 ± 0.10	12.12 ± 0.02
23	Cr II	2056, 2062	−1.61 ± 0.03	2.97 ± 0.05	11.84 ± 0.06
23	Mn II	2577, 2594, 2606	−1.61 ± 0.03	2.97 ± 0.05	11.51 ± 0.03
23	Fe I	2484, 2524	−1.61 ± 0.03	0.48 ± 0.18	11.30 ± 0.06
23	Fe II	1608, 2344, 2374, 2383, 2587, 2600	−1.61 ± 0.03	2.97 ± 0.05	13.51 ± 0.01
23	Ni II	1710, 1742, 1752	−1.61 ± 0.03	2.97 ± 0.05	12.48 ± 0.04
23	Zn II	2026, 2063	−1.61 ± 0.03	2.97 ± 0.05	11.79 ± 0.02
24	Mg I	2026, 2853	7.63 ± 0.06	4.09 ± 0.12	11.90 ± 0.01
24	Al II	1671	7.63	5.36	12.82 ± 0.04
24	Al III	1855, 1863	7.63	5.36	11.72 ± 0.05
24	Si II	1527, 1808	7.63 ± 0.06	5.36 ± 0.25	14.16 ± 0.04
24	Ca II	3935	7.63 ± 0.06	3.17 ± 0.17	11.78 ± 0.01
24	Cr II	2056, 2062	7.63 ± 0.06	4.92 ± 0.13	11.61 ± 0.14
24	Mn II	2577, 2594, 2606	7.63 ± 0.06	4.92 ± 0.13	11.36 ± 0.03
24	Fe II	1608, 2344, 2374, 2383, 2587, 2600	7.63 ± 0.06	4.92 ± 0.13	13.36 ± 0.01
24	Ni II	1710, 1742, 1752	7.63 ± 0.06	4.92 ± 0.13	12.33 ± 0.06
24	Zn II	2026, 2063	7.63 ± 0.06	4.92 ± 0.13	11.59 ± 0.03
28	Mg I	2026, 2853	72.54 ± 0.06	6.03 ± 0.15	11.77 ± 0.01
28	Al II	1671	72.54	6.14 ± 0.15	12.57 ± 0.02
28	Al III	1855, 1863	72.54	6.14 ± 0.15	11.17 ± 0.13
28	Si II	1527, 1808	72.54 ± 0.06	6.45 ± 0.18	13.75 ± 0.02
28	Ca II	3935	72.54 ± 0.06	5.52 ± 0.13	12.08 ± 0.01
28	Cr II	2056, 2062	72.54 ± 0.06	5.81 ± 0.09	11.92 ± 0.06
28	Mn II	2577, 2594, 2606	72.54 ± 0.06	5.81 ± 0.09	11.34 ± 0.03
28	Fe II	1608, 2344, 2374, 2383, 2587, 2600	72.54 ± 0.06	5.81 ± 0.09	13.51 ± 0.01
28	Ni II	1710, 1742, 1752	72.54 ± 0.06	5.81 ± 0.09	12.32 ± 0.06
28	Zn II	2026, 2063	72.54 ± 0.06	5.81 ± 0.09	10.72 ± 0.11

trast, the observed column density is two orders of magnitude lower, providing direct observational evidence of high ionization. The same arguments applies to component 16.

Additional confidence is provided by photoionization simulations. For the calculations we consider a plane-parallel slab of gas that is irradiated by the cosmic UV background of QSOs and galaxies (Madau et al. 1999).[2] We further assume a column density of 10^{16} hydrogen atoms cm^{-2} and solar chemical composition. The photoionization models are defined by the total hydrogen density $n_{\rm H}$ and the dimensionless ionization parameter

$$U = \frac{n_\gamma}{n_{\rm H}}, \qquad (1)$$

where

$$n_\gamma = \frac{4\pi}{c} \int_{\nu_{\rm L}}^{\infty} \frac{J(\nu)}{h\nu}\, {\rm d}\nu \qquad (2)$$

is the number density of hydrogen-ionizing photons striking the illuminated face of the slab. For instance, for a total hydrogen density of $n_{\rm H} = 10^{-1}$ particles cm^{-3} the cosmic UV background with $4\pi J_{\nu_{\rm L}} = 8.6 \times 10^{-21}$ erg cm^{-2} corresponds to an ionization parameter of $U = 2 \times 10^{-4}$. Figure 7 demonstrates that the observed column density ratios are well reproduced, if U falls between 10^{-4} and 10^{-3}. The degree of ionization for this range of U is higher than 90 percent. Similar results are obtained for column densities of 10^{17} and 10^{18} hydrogen atoms cm^{-2} and column density ratios corresponding to component 16.

In summary, there is conclusive evidence that the peripheral metal line components are formed within H II regions. The proof of ionized gas is facilitated by the extreme extent of the H I absorption velocity interval, revealing individual H I components. Figure 6 provides an empirical method to identify H II regions when individual H I components are not detectable.

[2] The photoionization simulations have been carried out with version 05.07 of Cloudy, last described by Ferland et al. (1998). The cosmic UV background at redshift 1.15 has been calculated using lookup tables provided by F. Haardt.

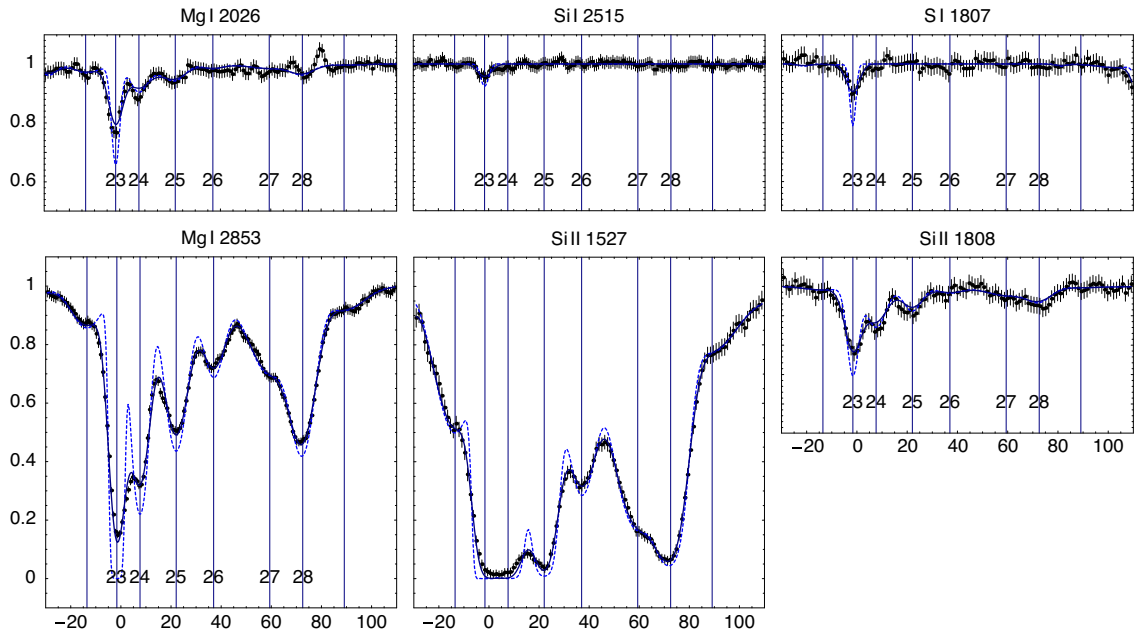

Fig. 3. Close-up of associated metal lines. Individual components are labeled by numbers 23-28

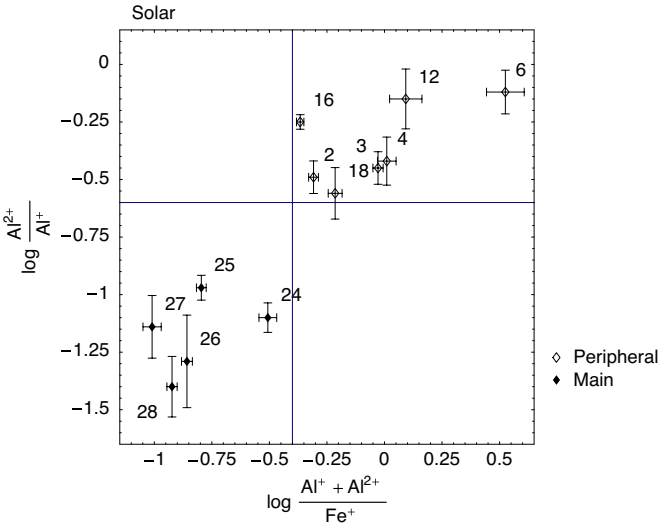

Fig. 6. Empirical diagram of ionization vs apparent nucleosynthetic enrichment of Al relative to Fe. Since the peripheral and main components, which are formed within H II and H I regions, respectively, are well separated, the diagram can be used to distinguish mainly ionized and neutral gas in general

4.2.2. Main components

The presence of ionized gas within the main absorber is not as evident as for the periphery. The Si III profile is optically thick, suggesting an apparent column density possibly exceeding 10^{13} ions cm^{-2} for components 20–28, but most of the absorption is due to Lyman forest lines (see the preceding subsection). While the stronger Si IV profile is blended into the Lyman forest, the weaker Si IV profile may confirm the Si III absorption for components 27–31. Conclusive evidence of ionized gas is provided by the C IV and Al III lines. The velocity structure of the C IV line, with an apparent column density of up to 2×10^{12} ions cm^{-2}, is weak and without noticeable substructure in the domain of components 22–26, indicating that ionized and neutral gas are not intermixed. In contrast, the Al III profiles indicate a homogenous distribution of high- and low-ions for components 23–25. The column density ratio of Al III to Al II lines is less than 1/10 for all components (Fig. 6).

According to simple photoionization calculations an ionization of the molecular regions due to the cosmic UV background is ruled out (Fig. 8). However, some fractional ionization due to stellar sources is conceivable. The comparison with photoionization simulations considering both interstellar radiation and the formation of molecules and dust requires an accurate recording of H_2 lines that is not available. Our simplest attempts assuming Galactic environmental conditions have yielded inconsistent results, reproducing the ionic ratios of iron and sillicon as well as the relative population of neutral carbon fine-structure levels, but overpredicting the amount of molecular hydrogen and underpredicting the Ca II absorption by more than one order of magnitude.

4.3. Metal abundances and dust depletion

Besides ionization and nucleosynthetic effects, the chemical composition analysis of interstellar environments is hampered by dust grains removing an unknown amount of atoms from the gaseous phase (Spitzer & Jenkins 1975; Savage & Sembach 1996). The accepted procedure to unravel these effects is to compare the abundance of refractory and volatile elements X, Y for which the photospheric abundance ratio (X/Y) is constant in stars over a wide range of metallicities. In that case an observed deviation from the stellar ratios is unlikely to have a nucleosynthetic origin. Even though the existence of a stellar proxy for interstellar abundances is questionable (Sofia & Meyer 2001) the Sun is used as a standard of reference for the total, i.e. gas plus dust, interstellar composition. For given observed column

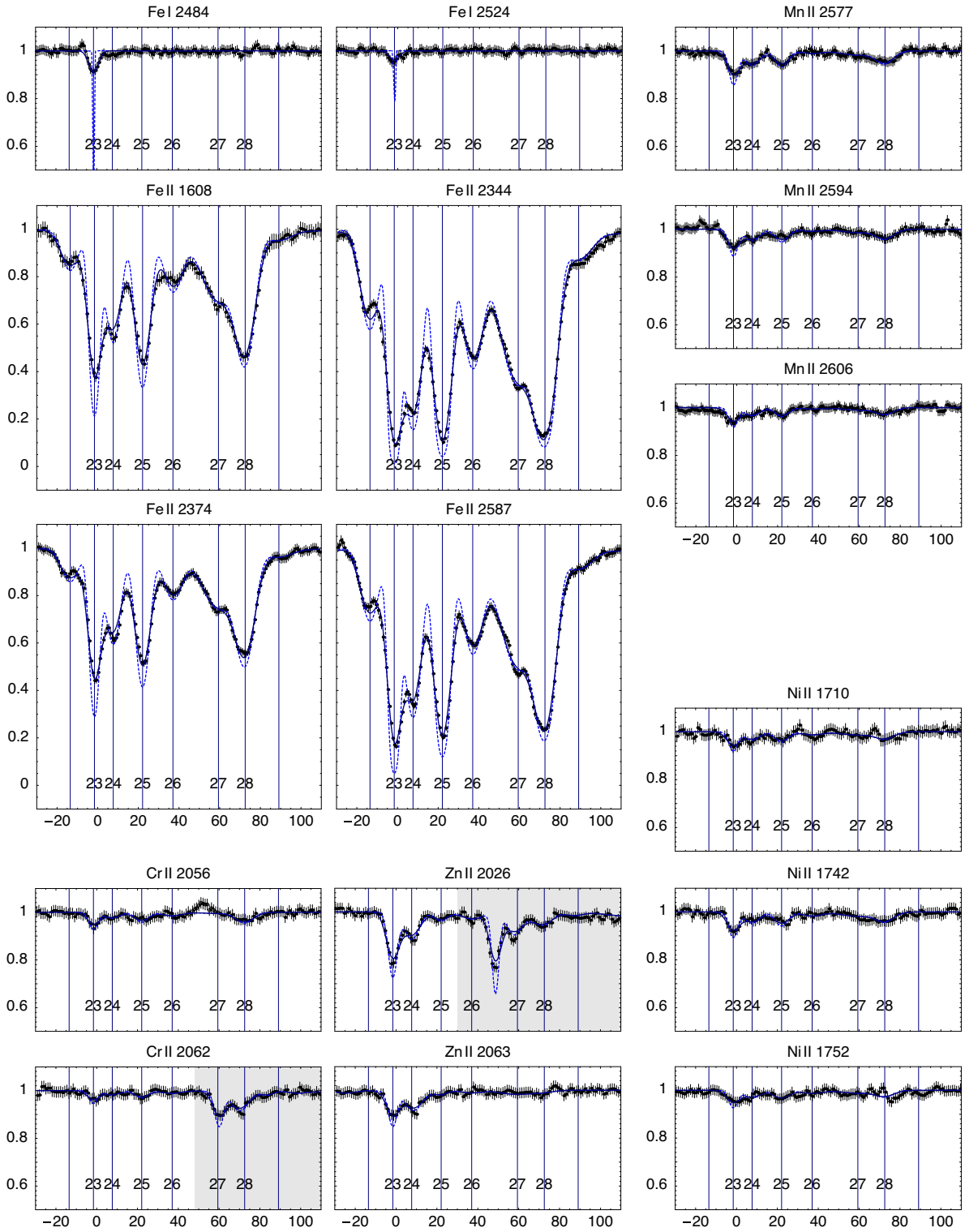

Fig. 3. continued. The shadings mark the main components of the Mg I λ2026 and Zn II λ2063 lines

densities N_X and N_Y the relative abundance of elements X and Y is expressed as

$$[X/Y] = \log(N_X/N_Y) - \log(X/Y)_\odot. \quad (3)$$

Element abundances relative to hydrogen are termed absolute abundances. For chemical composition analysis, we use the metal abundances in meteorites (Anders & Grevesse 1989) as a standard of reference.

4.3.1. Peripheral components

Since the peripheral components are formed within H II regions, the element abundances cannot be determined directly.

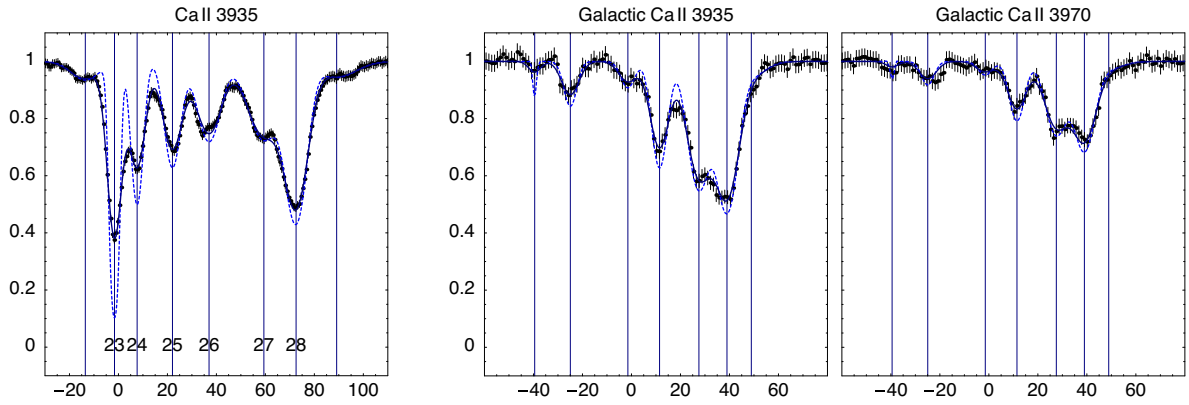

Fig. 4. Associated Ca II lines compared with the corresponding interstellar absorption in the Galactic halo along the same line-of-sight. No Ca II absorption is detected for the peripheral components

The observed ion abundances, however, are supersolar and photoionization calculations conform with the idea that both absolute and relative metal abundances are solar (Fig. 7).

4.3.2. Main components

For the main components photoionization calculations suggest that the absorbing material is predominantly neutral and ionization effects are negligible, i.e. all elements are accurately represented by the predominant ions. For the chemical composition analysis and the proper unravelling of dust depletion and nucleosynthetic effects the detection of volatile elements is essential. The only volatile element detected in the predominant ionization stage with accurate column density measurements for several main components is Zn. For other volatile elements like N and O also detected in the predominant ionization stage, the absorption is saturated and largely blended with Lyman forest lines (Fig. 5). Even though the Zn II absorption is weak, the individual column densities are well defined because the positional and broadening parameters of the decomposed Zn II profiles are tied to those of the Fe II lines.

Gas-phase abundances The observed abundances of refractory elements relative to Zn for components 23–28 are illustrated in Fig. 9. For components 23 and 24 the underabundance of the iron group elements Cr, Mn, Fe and Ni relative to Zn is comparable to that in the Galactic warm disk, whereas the mild and even vanishing depletion for components 25 and 28 is not found in Galactic interstellar space (Spitzer & Jenkins 1975; Savage & Sembach 1996). The relative abundances found for components 26 and 27 rather resemble those of the Galactic halo. If Zn is indeed undepleted and traces Fe as found by Nissen et al. (2004), the pattern of relative abundances directly reflects the differential depletion of chemical elements into dust grains. This idea gains indirect support by the detection of H_2 absorption lines associated with components 23 and 24, since molecules are essentially formed on the surface of dust grains (Cazaux et al. 2005; Williams 2005). For all components showing evidence of dust grains, the depletion of Si is stronger than in the Galactic warm disk, but weaker than in the cold disk. For all but the H_2-bearing components Mn is systematically underabundant when compared to the rest of iron group elements. The synthesis of Mn, however, is expected to be suppressed due to the nuclear odd-even effect. The average metallicity for components 23–28 is [Zn/H] = -0.38 ± 0.04.

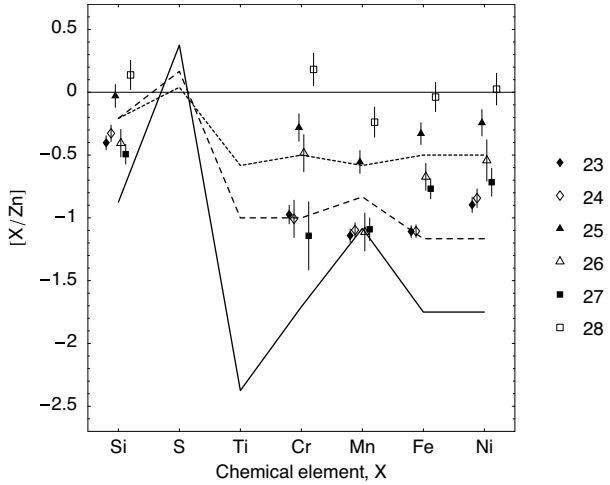

Fig. 9. Gas-phase abundance ratios (relative to solar ratios) for the main components 23–28 compared with those in the Galactic interstellar medium (dotted line: warm halo gas; dashed line: warm disk gas; solid line: cold disk gas; Welty et al. 2001). If the volatile element Zn is undepleted, the abundance ratios reflect the differential depletion of chemical elements into dust grains. Note that Cr, Mn, Fe, and Ni are strongly depleted for the H_2-bearing components 23 and 24, but essentially undepleted for component 28

The apparent underabundance of Fe (and Si) relative to Zn cannot be the result of ionization effects caused by the cosmic UV background since these would pretend an enhanced abundance (Fig. 8). Therefore, the interpretation of the observed underabundance as evidence of depletion into dust grains cannot be questioned without admitting very unusual nucleosynthetic effects. On the other hand, if the observed underabundance of Fe (and Si) relative to Zn is the net result of dust depletion and ionization effects, the true depletion might be even stronger than illustrated in Fig. 9. Nonetheless, the abundance gradient among components 23–28 may partially be brought by ionization effects.

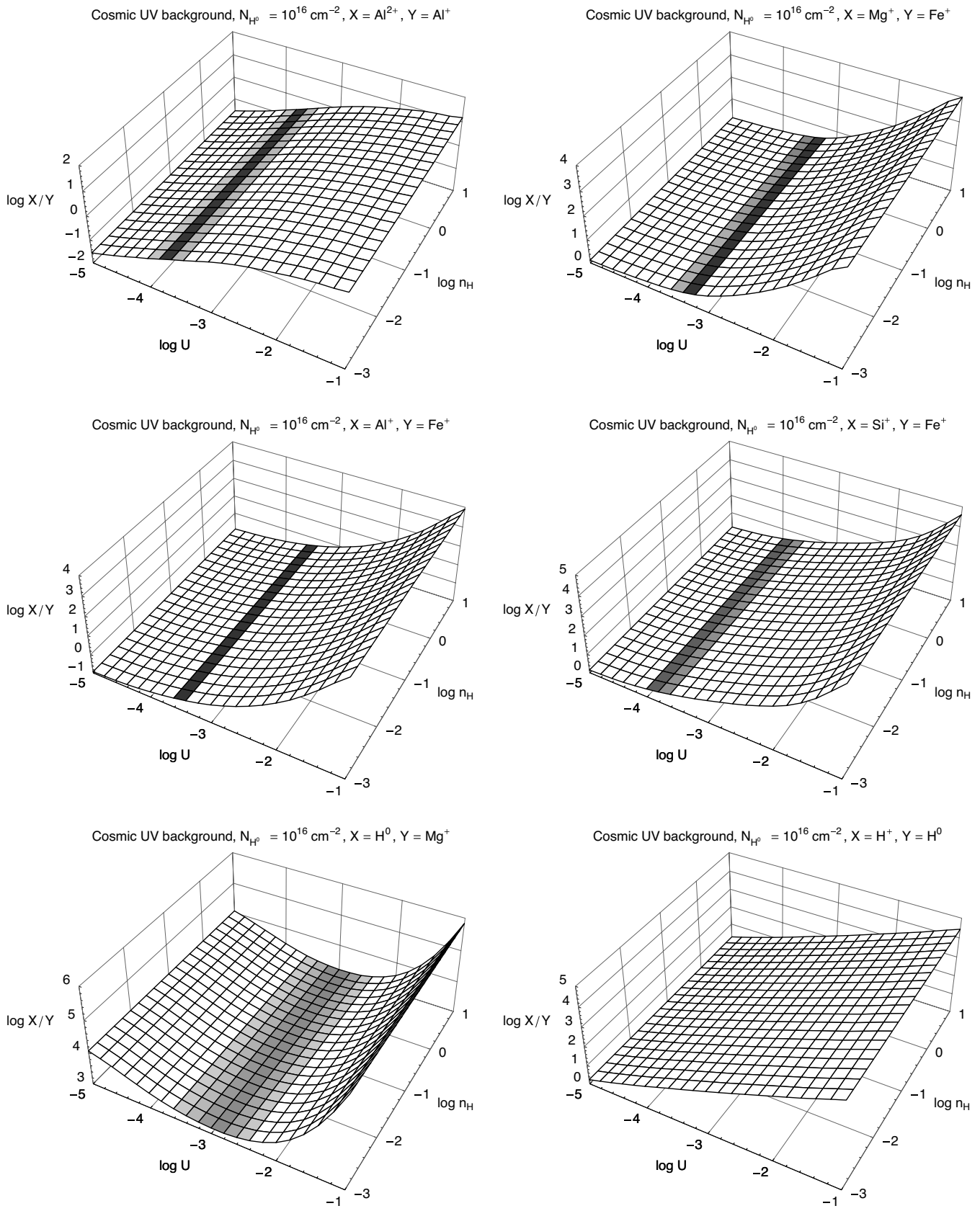

Fig. 7. Photoionization simulations considering a plane-parallel slab of gas with column density of 10^{16} hydrogen atoms cm^{-2} and solar chemical composition. The abscissas mark the ionization parameter U and the total hydrogen density $n_{\rm H}$. Shaded cells indicate consistency with the observed column density ratios for component 2, unshaded cells mark contradiction at more than 99.7 percent significance. For the medium corresponding to component 2 where $U > 10^{-4}$ the predicted degree of ionization exceeds 90 percent. Note that the observed column density ratios will pretend an enrichment of α-elements if ionization effecs are ignored

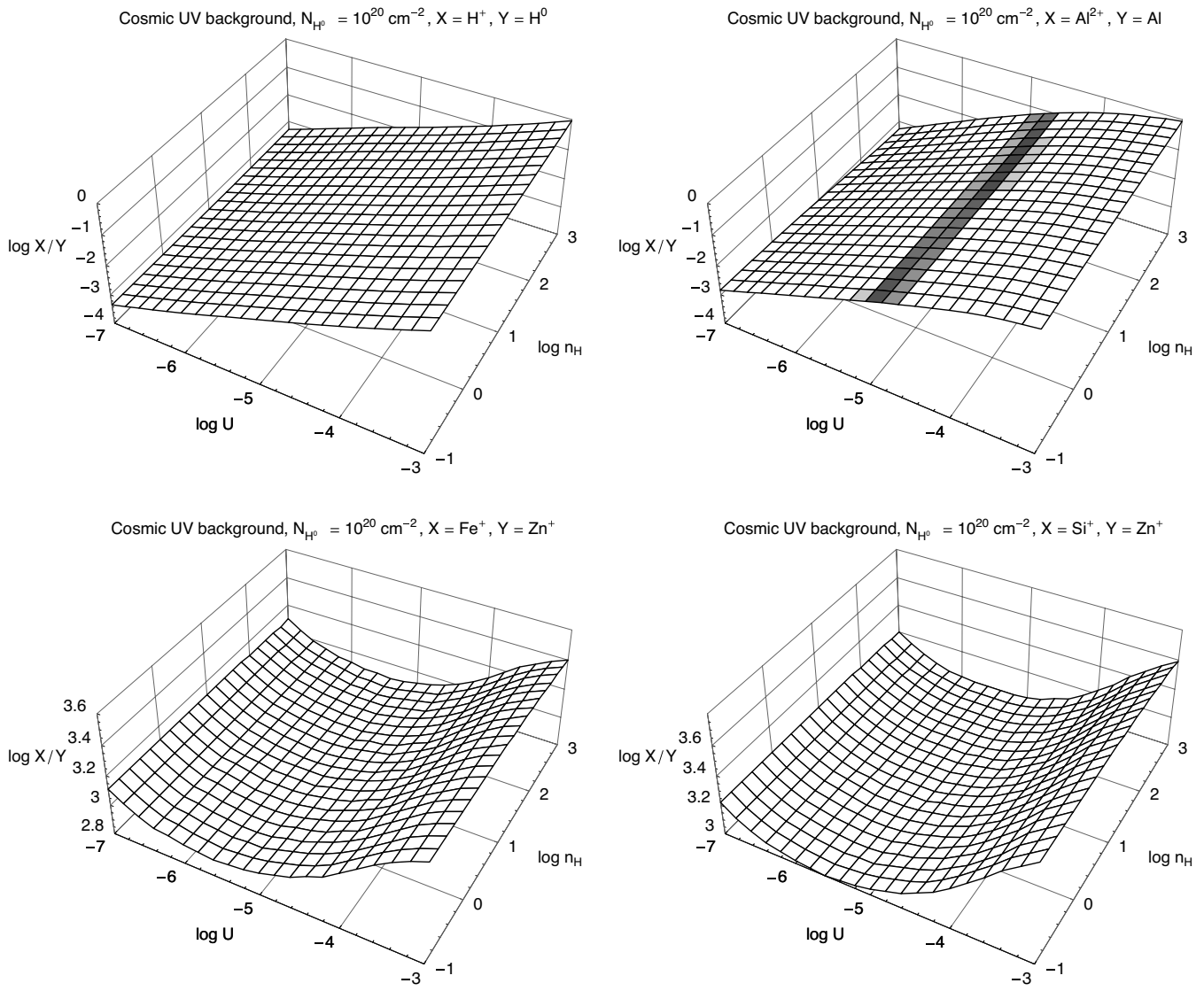

Fig. 8. The same as Fig. 7 but a plane parallel slab with column density of 10^{20} hydrogen atoms cm^{-2} is considered. *Top:* For a total hydrogen density of 10^{-1} particles cm^{-3} the cosmic UV background corresponds to an ionization parameter of $U = 2 \times 10^{-4}$. For denser regions like molecular gas the same ionizing background corresponds to $U < 10^{-4}$, implying that at most 10 percent of the hydrogen is ionized. This argument is confirmed by the observed column density ratio of Al ions (illustrated by the shading for component 24, but also see Fig. 6). *Bottom:* The minimum of the predicted ratio of Fe and Zn ion abundances corresponds to the case where both elements almost completely reside in the first ionization stage and the abundance ratio of ions is almost equal to the (solar) abundance ratio of elements. Note that ionization effects cannot pretend a depletion of Fe relative to Zn. The situation for Si and Zn is similar

In summary, there is decisive evidence of Galaxy-like differential depletion of elements into dust grains, with a significant gradient from component to component as if the sight line is intersecting different interstellar environments comparable to the Galactic disk and halo. Another such example may be the DLA system toward the gravitationally lensed QSO HE 0512–3329, where different element abundances are detected along two lines of sight (Lopez et al. 2005). Further examples are given by Dessauges-Zavadsky et al. (2006).

Dust correction Based on the presumption that the chemical composition of dust is defined by the physical state and the chemical composition of the medium, Vladilo (2002a,b) has worked out an analytic relation between the dust depletion patterns for interstellar environments of different types. Though generalizing former approaches where the dust composition is assumed to be constant, his new approach still implies that the dust composition does not depend on the history of the medium, a condition that is not strictly satisfied since the formation of dust and ices involves irreversible processes (Vidali et al. 2005).

For any interstellar environments i, j and constant sensitivity of the chemical composition of dust to variations in the dust-to-metal ratio ρ and the chemical composition of the medium, the fractions of the generic and reference elements X, Y contained in dust grains are related by

$$f_{X,j} = \rho^{\eta_X+1} 10^{[X/Y]_{\mathrm{m},j}\,(\epsilon_X-1)} f_{X,i}. \quad (4)$$

The subscript 'm' indicates reference to all atoms in the medium, i.e. in the gaseous and the solid phase. The exponents η_X, ϵ_X define the response of the relative abundance of X in the solid phase to the variation of the fraction of Y contained in dust, and the relative abundance of X in the medium, respectively (Vladilo 2002a,b).

Equation (4) is capable of reproducing the Galactic interstellar depletion patterns $\delta_X = \log(1 - f_X)$ with a varying dust-to-metal ratio

$$\rho = \frac{f_{Y,j}}{f_{Y,i}} \tag{5}$$

and a single set of empirical constants $(f_{X,i}, \eta_X)$.[3] The depletion patterns in the interstellar medium of the SMC can be reproduced with the same set of constants, if the relative element abundances are allowed to deviate from solar values. From the theoretical point of view, the dust-corrected element abundances of high-redshift DLA systems show better consistency with galactic chemical evolution models than the plain observations (Calura et al. 2003).

An explicit relation between observed and intrinsic absolute abundances is obtained by using Eq. (4) to express the fraction of X contained in the gaseous phase of medium j:

$$\frac{10^{[X/\mathrm{H}]_{\mathrm{g},j}}}{10^{[X/\mathrm{H}]_{\mathrm{m},j}}} = 1 - \rho^{\eta_X+1} 10^{[X/Y]_{\mathrm{m},j}\,(\epsilon_X-1)} f_{X,i}, \tag{6}$$

where the subscript 'g' indicates reference atoms in the gaseous phase. The parameters $f_{X,i}$ and η_X can be calculated from Galactic interstellar depletion patterns (Vladilo 2002a,b), whereas the dust-to-gas ratio ρ is an implicit function of the observed and intrinsic abundance ratios

$$\rho - \frac{10^{[X/Y]_{\mathrm{m},j}\,\epsilon_X} f_{X,i}}{10^{[X/Y]_{\mathrm{g},j}} f_{Y,i}} \rho^{\eta_X+1} + \frac{10^{[X/Y]_{\mathrm{m},j}} - 10^{[X/Y]_{\mathrm{g},j}}}{10^{[X/Y]_{\mathrm{g},j}} f_{Y,i}} = 0, \tag{7}$$

which is obtained by dividing Eq. (6) by the corresponding equation for $X = Y$. The intrinsic abundance ratio $[X/Y]_{\mathrm{m},j}$ and the exponent ϵ_X are unknown parameters. For the latter only two extreme cases are considered where the relative element abundances in the solid phase and the medium are mutually independent, $\epsilon_X = 0$, or directly proportional, $\epsilon_X = 1$. Superlinear response $\epsilon_X > 1$ is ignored. For the intrinsic abundance ratio $[X/Y]_{\mathrm{m},j}$ an element $X = Z$ ideally tracing the reference element Y is required.

Given the observed abundance ratios $10^{[X/Y]_{\mathrm{g},j}}$ and an educated guess of $[Z/Y]_{\mathrm{m},j}$, the dust-to-metal ratio ρ is defined by Eq.(7). The rest of intrinsic abundance ratios $[X/Y]_{\mathrm{m},j}$ for elements $X \neq Z$ implicitly follows from

$$10^{[X/Y]_{\mathrm{m},j}} - \rho^{\eta_X+1} f_{X,i}\, 10^{[X/Y]_{\mathrm{m},j}\,\epsilon_X} + (\rho f_{Y,i} - 1)\, 10^{[X/Y]_{\mathrm{g},j}} = 0. \tag{8}$$

The roots of Eqs. (7, 8) can be calculated with simple bisectioning and the statistical errors of all quantities involved in the calculation, i.e. observed column densities, meteoritic element abundances, $f_{X,i}$, η_X, can be propagated by means of Monte Carlo methods. The intrinsic absolute element abundances $[X/\mathrm{H}]_{\mathrm{m},j}$ follow from Eq. (6). The dust-to-gas ratio is given by

$$\kappa = \rho\, 10^{[Y/\mathrm{H}]_{\mathrm{m},j}}. \tag{9}$$

For the corrective procedure we choose Y = Fe since the Fe II lines provide the most reliable column densities. The most suitable element for calculating the dust-to-metal ratio is Z = Zn. The rest of elements with known parameters $f_{X,i}, \eta_X$ are either too affine to the solid state, or have an interstellar enrichment history too different from that of Fe to make an assumption about the intrinsic abundance ratio. If Zn proves a tracer of Si as suggested by Wolfe et al. (2005), the combination Y = Si and Z = Zn will be an eligible option. For the present case, however, this option results in implausible dust-to-metal ratios throughout exceeding those in the Galactic cold disk. Following Vladilo (2004), we consider six different model cases labeled with A0, A1, B0, B1, E0, and E1. The capital letter indicates the intrinsic abundance of Zn relative to Fe, assumed solar for cases A and B, and enhanced for case E, $[\mathrm{Zn/Fe}]_{\mathrm{m},j} = 0.1$. For cases A and E the fraction of Zn assumed to be contained in interstellar dust is $f_{\mathrm{Zn},i} = 0.59$, for case B the assumed depletion is lower, $f_{\mathrm{Zn},i} = 0.30$. The number to the right of the capital letter directly represents the value of the exponent ϵ_X. Zinc might be no precise tracer of iron since its exact nucleosynthetic origin is unknown, but the average photospheric abundance ratios in Galactic disk and halo stars are approximately solar or slightly enhanced (Chen et al. 2004; Nissen et al. 2004) and substantiate the model specifications.

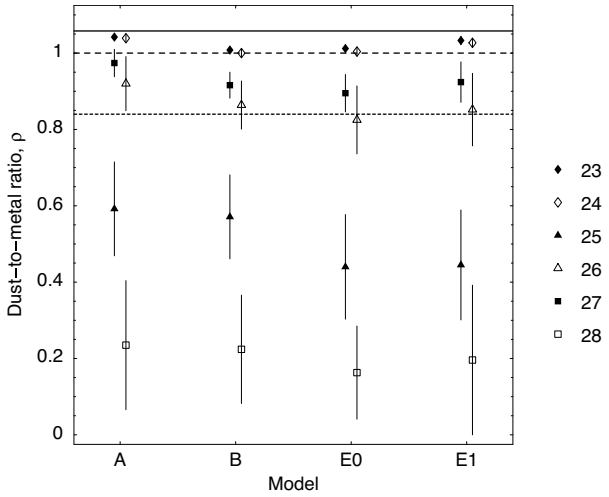

Fig. 10. Dust-to-metal ratio ρ for the main components 23-28 compared with values typical for the Galactic interstellar medium (dotted line: warm halo gas; dashed line: warm disk gas; solid line: cold disk gas; Vladilo 2002b). The results for models A and B do not depend on the exponent ϵ_X

Dust-to-metal ratio The calculated dust-to-metal ratios and correponding fractions of Fe contained in dust are presented in Fig. 10 and Table 4, respectively. If there is a one-to-one correspondence between the physical state of the interstellar environment and the dust-to-metal ratio, Fig. 10 illustrates the

[3] For the Galaxy, the exponent ϵ_X is irrelevant since the interstellar element abundances are assumed to be solar.

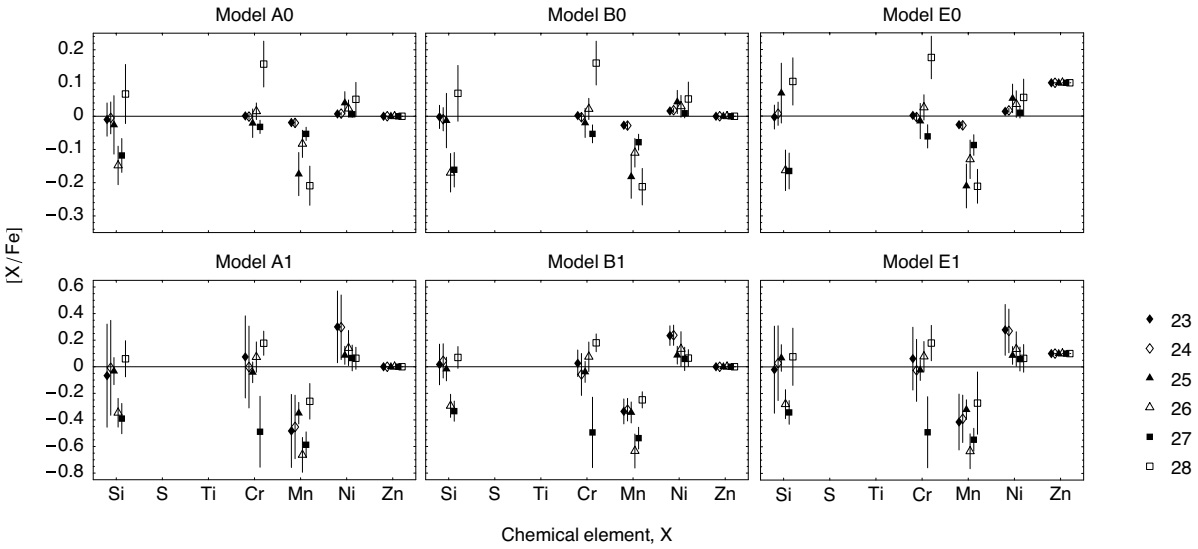

Fig. 11. Intrinsic abundance ratios (relative to solar ratios) for the main components 23-28

multiphase structure of the absorbing medium. Though such diversified structure is characteristic for the interstellar medium in the Galaxy and the Magellanic Clouds (Savage & Sembach 1996; Welty et al. 1997, 1999, 2001) it is usually not attributed to DLA systems (Prochaska 2003). The dust-to-metal ratio for the H_2-bearing components 23 and 24 exceeds the ratio of the warm Galactic disk, for some models the ratio aproaches the ratio found in the cold disk. For components 26 and 27 the dust-to-metal ratio compares to that in the intermediate warm Galactic disk and halo, whereas for the the rest of components the dust-to-metal ratio is typical of higher-redshift DLA systems (Vladilo 2004). These basic results conform with the observed depletion pattern (Fig. 9) and are independent of the adopted model, in particular unaffected by the choice of $[\mathrm{Zn/Fe}]_{\mathrm{m},j}$.

Intrinsic abundances and dust-to-gas ratio The calculated intrinsic abundance ratios are presented in Fig. 11. For all models the intrinsic abundance ratios conform with solar values, apart from three exceptions:

1. The mean intrinsic abundance of Ni relative to Fe is slightly enhanced. Similar offsets are also found for Galactic thick disk stars (Prochaska et al. 2000).
2. The intrinsic abundance of Mn is reduced. The reduction is most distinct for the less dust-containing components 25–28 and for models where the relative element abundances in dust and in the medium scale directly, i.e. $\eta_X = 1$. Similar underabundances, usually attributed to the nuclear odd-even effect, are found for Galactic thick disk stars (Prochaska et al. 2000) as well as DLA systems (Dessauges-Zavadsky et al. 2006).
3. For the intermediate components 26 and 27 the intrinsic abundance of Si relative to Fe is always subsolar, in marked contrast to the expected nucleosynthetic enrichment of α-elements and to element abundances found for Galactic stars. For these components, the dust-corrective procedure may have overestimated (underestimated) the fraction of Fe (Si) contained in dust.

Since only the total column density of hydrogen atoms contained in the main absorber is known, Eq. (6) cannot be used to calculate the intrinsic absolute abundances for individual components. Nonetheless, by cumulating the individual dust-corrected column densities $N_{Y,\mathrm{m}} = \sum_j N_{Y,j}/(1 - f_{Y,j})$, we can calculate an average intrinsic metallicity $[Y/\mathrm{H}]_{\mathrm{m}}$. Inserting the calculated fractions of Fe contained in dust (Table 5) yields an almost solar intrinsic metallicity of $[\mathrm{Fe/H}]_{\mathrm{m}} = -0.08 \pm 0.19$. Assuming that the observed H I absorption is only constituted by components 23–24, the dust-to-metal ratio of $\rho = 1.02 \pm 0.02$ and the intrinsic metallicity of $[\mathrm{Fe/H}]_{\mathrm{m}} = -0.20 \pm 0.21$ give an average dust-to-gas ratio of $\kappa = 0.64 \pm 0.31$.

4.4. Kinematic structure

With an absorption velocity interval extending for 700 km s^{-1} the kinematic distribution of associated metal line components is quite unique. Only the $z = 1.97$ DLA system toward QSO 0013–004 shows an even more extended spread (Petijean et al. 2002). The $z = 2.19$ sub-DLA system toward HE 0001–2340 has a comparable neutral hydrogen column density, but a less extended absorption velocity interval of 400 km s^{-1} and much lower metallicity (Richter et al. 2005). Rotating disks models (Prochaska & Wolfe 1997) and simulations of merging protogalactic clumps (Haehnelt et al. 1998) do explain the characteristic kinematic features like asymmetric edge-leading line profiles, but fail to reproduce absorption intervals exceeding 250 km s^{-1}. Large absorption intervals have therefore been associated with interacting or merging galaxies producing extended tidal filaments like the Antennae (e.g. Wilson et al. 2000; Zhang et al. 2001). Another viable scenario is a line-of-sight intecepting a cluster of galaxies. The kinematic distribution of metal line components associated with the present sub-DLA system (Fig. 2) indeed supports the idea that two different absorbers are involved.

Table 4. Fractions of Fe contained in dust, $f_{\mathrm{Fe},j}$, for the main components 23-28 and different models. The results for models A and B do not depend on the exponent ϵ_X

No.	A	B	E0	E1	Mean
23	0.98 ± 0.01	0.95 ± 0.01	0.95 ± 0.01	0.97 ± 0.01	0.96 ± 0.02
24	0.98 ± 0.01	0.94 ± 0.01	0.94 ± 0.01	0.96 ± 0.01	0.96 ± 0.02
25	0.56 ± 0.12	0.54 ± 0.10	0.41 ± 0.13	0.42 ± 0.14	0.48 ± 0.08
26	0.86 ± 0.07	0.81 ± 0.06	0.77 ± 0.08	0.80 ± 0.09	0.81 ± 0.04
27	0.92 ± 0.03	0.86 ± 0.03	0.84 ± 0.05	0.87 ± 0.05	0.87 ± 0.03
28	0.22 ± 0.16	0.21 ± 0.13	0.15 ± 0.11	0.18 ± 0.18	0.19 ± 0.03

Table 5. Cumulative dust-corrected column density of Fe contained in the main absorber, $\log N_{\mathrm{Fe,m}}$ (cm^{-2})

No.	A	B	E0	E1	Mean
23–24	15.44 ± 0.18	15.00 ± 0.04	15.03 ± 0.05	15.28 ± 0.14	15.19 ± 0.21
23–28	15.54 ± 0.17	15.15 ± 0.03	15.16 ± 0.04	15.39 ± 0.18	15.31 ± 0.19

4.4.1. Peripheral components

The peripheral components can be discerned into inner and an outer parts where the kinematic characteristics are markedly different. The velocity structure of the outer part constituted by components 1–15 is characterized by a number density of components, with an average of one component every 20 $\mathrm{km\,s^{-1}}$. The dominating substructure is edge-leading, but the remaining features appear randomly distributed. In contrast, the inner part defined by components 16–19 is characterized by four well separated components, with an average of one component every 40 $\mathrm{km\,s^{-1}}$, and some absorption-free parts.

4.4.2. Main components

The main structure is characterized by the highest frequency of peaks, with an average of one peak every 15 $\mathrm{km\,s^{-1}}$. Two substructures may be recognized, both edge-leading for the less refractory elements like Mg and Si, but rather unordered otherwise.

Particularly instructive is the comparison of extragalactic Ca II absorption lines with those originating in the Galactic halo (Bowen 1991). First ignoring components 23 and 24, the redshifted and the Galactic line profiles are remarkably similar (Fig. 4), indicating that components 25–28 correspond to halo-like structures. Further developing this analogy, the narrow structures 23 and 24 not present in the absorption by the Galactic halo may be interpreted as signature of disk-like agglomeration, a picture which conforms with the observed depletion of elements into dust (Figs. 9, 10).

4.5. Physical conditions

The physical conditions in DLA absorbers like the number density and kinetic temperature of hydrogen atoms and the local microwave and FUV radiation can be inferred from the diagnostics of fine-structure absorption lines (Bahcall & Wolf 1968; Silva & Viegas 2002). For the present absorber the analysis of excited C I lines associated with the H_2 bearing components 23 and 24 provides an upper limit on the FUV input (Quast et al. 2002). The study of H_2 lines predicts a radiation input exceeding the Galactic interstellar energy density by more than an order of magnitude and a number density greater than 100 hydrogen atoms cm^{-2} (Reimers et al. 2003; Hirashita & Ferrara 2005).

Assuming an FUV input equal to the scaled generic Galactic radiation field (Draine & Bertoldi 1996), but otherwise repeating the statistical equilibrium calculations of Quast et al. (2002), we note that both an intense radiation field and a number density exceeding 100 hydrogen atoms cm^{-2} only conform with the observed population of fine-structure levels, if the kinetic temperature is about $T_{\mathrm{kin}} = 25$ K, which is at variance with the population temperature of 80 K inferred from the lower rotational H_2 levels (Reimers et al. 2003). On the other hand, if the population of lower and higher rotational H_2 levels is in thermal equilibrium with $T_{\mathrm{kin}} = 400$ K, the number density of hydrogen atoms can only exceed 60 cm^{-2} if the local and Galactic interstellar radiation are comparable (Fig. 12). The present spectroscopy of H_2 lines, however, is too inadequate to provide reliable results. Besides, the spatial distributions of carbon atoms and hydrogen molecules may not be identical, allowing different kinetic temperatures for both constituents (Spitzer & Jenkins 1975).

5. Summary and conclusions

Based on high-resolution spectra obtained with STIS and the VLT UVES we have presented a reanalysis of the chemical composition, kinematic structure, and physical conditions of the H_2-bearing sub-DLA system toward HE 0515–4414. The sub-damped system is unusual in several aspects:

1. The velocity interval of associated metal lines extends for 700 $\mathrm{km\,s^{-1}}$. The distribution of metal line components is bimodal, indicating the presence of two interacting absorbers.
2. Two peripheral H I components with $N_{\mathrm{H\,I}} = 10^{15}$ and 10^{17} cm^{-2} are detected at distances of, respectively, 530 and 240 $\mathrm{km\,s^{-1}}$ from the $N_{\mathrm{H\,I}} = 8\times10^{19}$ cm^{-2} main component. For the peripheral components, the column densities of H I

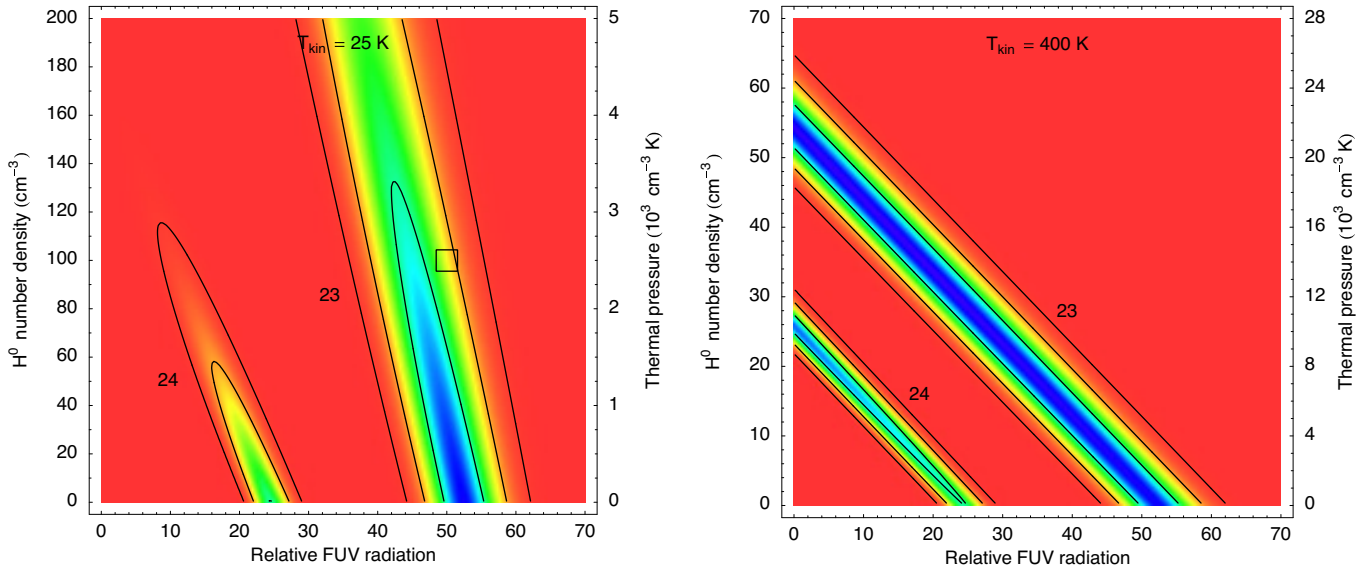

Fig. 12. Physical conditions for the H_2-bearing components 23 and 24 inferred from the observed population of C^0 fine-structure levels. Contour lines are drawn at 0.61, 0.14, and 0.01 of the maximum probability density and would correspond to the boundaries of the 68.3, 95.4, and 99.7 percent confidence regions if the distributions were normal. Two extreme cases are considered for the kinetic gas temperature. *Left:* The high number density of hydrogen atoms and the intense FUV radiation found by Hirashita & Ferrara (2005, marked by an empty square) require a low kinetic temperature. *Right:* If the population of lower and higher rotational H_2 levels is in thermal equilibrium with $T_{\rm kin}$ = 400 K, either an intense FUV field or a high number density is ruled out

and associated Al II, Al III, and Fe II lines provide direct observational evidence of H II regions.

3. The metal line components associated with the peripheral H I lines are formed within H II regions, only components 20–31 are associated with the main absorber and correspond to predominantly neutral gas.
4. For the main components 23–28 the observed abundance ratios of refractory elements Si, Cr, Mn Fe, Ni to Zn show a distinct gradient along the sight line. The differential depletion of refractory elements ranges from Galactic warm disk to halo-like and essentially undepleted patterns. The variation in the dust-to-metal ratio indicates the multiphase structure of the absorbing medium. The dust-corrected metal abundances show the nucleosynthetic odd-even effect and might imply an anomalous depletion of Si relative to Fe, but otherwise do correspond to solar abundance ratios. The intrinsic average metallicity is almost solar, $[{\rm Fe/H}]_{\rm m} = -0.08 \pm 0.19$, whereas the uncorrected average is $[{\rm Zn/H}]_{\rm g} = -0.38 \pm 0.04$. For the H_2-bearing components 23 and 24 the dust-to-metal and dust-to-gas ratios (relative to Galactic warm disk ratios) are $\rho = 1.02 \pm 0.02$ and $\kappa = 0.64 \pm 0.31$, respectively. The ion abundances in the periphery conform with solar element composition.
5. The diagnostics of fine-structure lines is not conclusive. Adequate recordings of the H_2 lines are needed to provide reliable results.

The presence of H II regions might have consequences for the DLA abundance diagnostics in general. If any metal line components are connected with H II rather than H I regions, the usual averaging of element abundances is incorrect. In particular, ionization effects can pretend an enrichment of α elements. We have obtained a diagnostic diagram (Fig. 6) which allows to detect H II region-like ionization conditions from empirical Al II, Al III, and Fe II column densities. If both $N_{\rm Al\,III}/N_{\rm Al\,II} > 0.25$ and $N_{\rm Al}/N_{\rm Fe\,II} > 0.40$, the absorbing material is largely ionized. In this context, it is interesting to note that high column densities can be attained by the interception of relatively compact regions. For the present case Reimers et al. (2003) have already pointed out that the absorption path length contributed by the H_2-bearing components 23 and 24 is less than 1 lyr when the number density of hydrogen atoms is about 100 $\rm cm^{-3}$.

Our analysis shows that sub-DLA systems can exhibit solar metallicities. If the highest-metallicity sub-DLA absorbers prove to be regular DLA absorbers having consumed large amounts of neutral hydrogen due to massive star formation, their detection is important. Modern surveys of DLA systems setting the cut-off below the traditional column density limit may provide interesting insights.

Acknowledgements. It is a pleasure to thank Francesco Haardt for providing us with machine readable lookup tables of the cosmic UV background. This research has been supported by the Verbundforschung of the BMBF/DLR under Grant No. 50 OR 9911 1 and by the DFG under Re 353/48.

References

Akerman, C. J., Ellison, S. L., Pettini, M., & Steidel, C. C. 2005, A&A, 440, 449
Anders, E. & Grevesse, N. 1989, Geochim. Cosmochim. Acta, 53, 197
Bahcall, J. N. & Wolf, R. A. 1968, ApJ, 152, 701
Bowen, D. V. 1991, MNRAS, 251, 649
Calura, F., Matteucci, F., & Vladilo, G. 2003, MNRAS, 340, 59
Cazaux, S., Caselli, P., Tielens, A. G. G. M., Le Bourlot, J., & Walmsley, M. 2005, J. Phys. Conf. Ser., 6, 155

Cen, R., Ostriker, J. P., Prochaska, J. X., & Wolfe, A. M. 2003, ApJ, 598, 741
Chen, Y. Q., Nissen, P. E., & Zhao, G. 2004, A&A, 425, 697
de la Varga, A., Reimers, D., Tytler, D., Barlow, T., & Burles, S. 2000, A&A, 363, 69
Dessauges-Zavadsky, M., Prochaska, J. X., D'Odorico, S., Calura, F., & Matteucci, F. 2006, A&A, 445, 93
Draine, B. T. & Bertoldi, F. 1996, ApJ, 468, 269
Fall, S. M. & Pei, Y. C. 1993, ApJ, 402, 479
Ferland, G. J., Korista, K. T., Verner, D. A., et al. 1998, PASP, 110, 761
Haehnelt, M. G., Steinmetz, M., & Rauch, M. 1998, ApJ, 495, 647
Hirashita, H. & Ferrara, A. 2005, MNRAS, 356, 1529
Ida, T., Ando, M., & Toraya, H. 2000, J. Appl. Cryst., 33, 1311
Jenkins, E. B. 1996, ApJ, 471, 292
Kulkarni, V. P., Fall, S. M., Lauroesch, J. T., et al. 2005, ApJ, 618, 68
Ledoux, C., Petijean, P., & Srianand, R. 2003, MNRAS, 346, 209
Levshakov, S. A., Agafonova, I. I., & Kegel, W. H. 2000, A&A, 360, 833
Lopez, S., Reimers, D., Gregg, M. D., et al. 2005, ApJ, 626, 767
Madau, P., Haardt, F., & Rees, M. J. 1999, ApJ, 514, 648
Maller, A. H., Prochaska, J. X., Sommerville, R. S., & Primack, J. R. 2001, MNRAS, 326, 1475
Maller, A. H., Prochaska, J. X., Sommerville, R. S., & Primack, J. R. 2003, MNRAS, 343, 268
Morton, D. C. 2003, ApJS, 149, 205
Murphy, M. T. & Liske, J. 2004, MNRAS, 354
Nagamine, K., Springel, V., & Hernquist, L. 2004, MNRAS, 348, 421
Nissen, P. E., Chen, Y. Q., Asplund, M., & Pettiini, M. 2004, A&A, 415, 993
Péroux, C., Dessauges-Zavadsky, M., Kim, T.-S., McMahon, R. G., & D'Odorico, S. 2002, Astrophys. Space Sci., 281, 543
Péroux, C., Dessauges-Zavadsky, M., D'Odorico, S., Kim, T.-S., & McMahon, R. G. 2003, MNRAS, 345, 480
Petijean, P., Srianand, R., & Ledoux, C. 2002, MNRAS, 332, 383
Prochaska, J. X. 2003, ApJ, 582, 49
Prochaska, J. X. & Wolfe, A. M. 1997, ApJ, 487, 73
Prochaska, J. X., Naumov, S. O., Carney, B. W., McWilliam, A., & Wolfe, A. M. 2000, AJ, 120, 2513
Prochaska, J. X., Howk, J. C., O'Meara, J. M., et al. 2002, ApJ, 571, 693
Prochaska, J. X., Gawiser, E., Wolfe, A. M., Castro, S., & Djorgovski, S. G. 2003, ApJ, 595, L9
Quast, R., Baade, R., & Reimers, D. 2002, A&A, 386, 796
Quast, R., Reimers, D., Smette, A., et al. 2004, in Proceedings of the 22nd Texas Symposium on Relativistic Astrophysics at Stanford University (SLAC-R-752), 1416
Quast, R., Baade, R., & Reimers, D. 2005, A&A, 431, 1167
Rao, S. M., Prochaska, J. X., Howk, J. C., & Wolfe, A. M. 2005, AJ, 129, 9
Reimers, D., Hagen, H.-J., Rodriguez-Pascual, P., & Wisotzki, L. 1998, A&A, 334, 96
Reimers, D., Baade, R., Quast, R., & Levshakov, S. A. 2003, A&A, 410, 785
Richter, P., Ledoux, C., Petitjean, P., & Bergeron, J. 2005, A&A, 440, 819
Savage, B. D. & Sembach, K. A. 1991, ApJ, 379, 245
Savage, B. D. & Sembach, K. A. 1996, ARA&A, 34, 279
Silva, A. I. & Viegas, S. M. 2002, MNRAS, 329, 135
Smette, A., Cleaskens, J.-F., & Surdej, J. 1997, New Astronomy, 2, 53
Smette, A., Wisotzki, L., Ledoux, C., et al. 2005, in Proc. IAU, Vol. 1, Probing Galaxies through Quasar Absorption Lines, 475–477
Sofia, U. J. & Meyer, D. M. 2001, ApJ, 554, L221
Spitzer, L. & Jenkins, E. B. 1975, ARA&A, 13, 133
Vidali, G., Roser, J., Manicó, G., et al. 2005, J. Phys. Conf. Ser., 6, 36
Vladilo, G. 2002a, ApJ, 569, 295
Vladilo, G. 2002b, A&A, 391, 407
Vladilo, G. 2004, A&A, 421, 479
Vladilo, G. & Péroux, C. 2005, A&A, 444, 461
Watson, D., Fynbo, J. P. U., Ledoux, C., et al. 2005, ApJ, submitted
Welty, D. E., Lauroesch, J. T., Blades, J. C., Hobbs, L. M., & York, D. G. 1997, ApJ, 489, 672
Welty, D. E., Frisch, P. C., Sonneborn, G., & York, D. G. 1999, ApJ, 512, 636
Welty, D. E., Lauroesch, J. T., Blades, J. C., Hobbs, L. M., & York, D. G. 2001, ApJ, 554, L75
Wild, V., Hewett, P. C., & Pettini, M. 2005, MNRAS, in press
Williams, D. A. 2005, J. Phys. Conf. Ser., 6, 1
Wilson, C. D., Scoville, N., Madden, S. C., & Charmandaris, V. 2000, ApJ, 542, 120
Wolfe, A. M. & Prochaska, J. X. 1998, ApJ, 494, L15
Wolfe, A. M. & Prochaska, J. X. 2000, ApJ, 545, 591
Wolfe, A. M., Prochaska, J. X., & Gawiser, E. 2003a, ApJ, 593, 215
Wolfe, A. M., Gawiser, E., & Prochaska, J. X. 2003b, ApJ, 593, 235
Wolfe, A. M., Gawiser, E., & Prochaska, J. X. 2005, ARA&A, 43, 861
Zhang, Q., Fall, S. M., & Whitmore, B. C. 2001, ApJ, 561, 727

Online Material

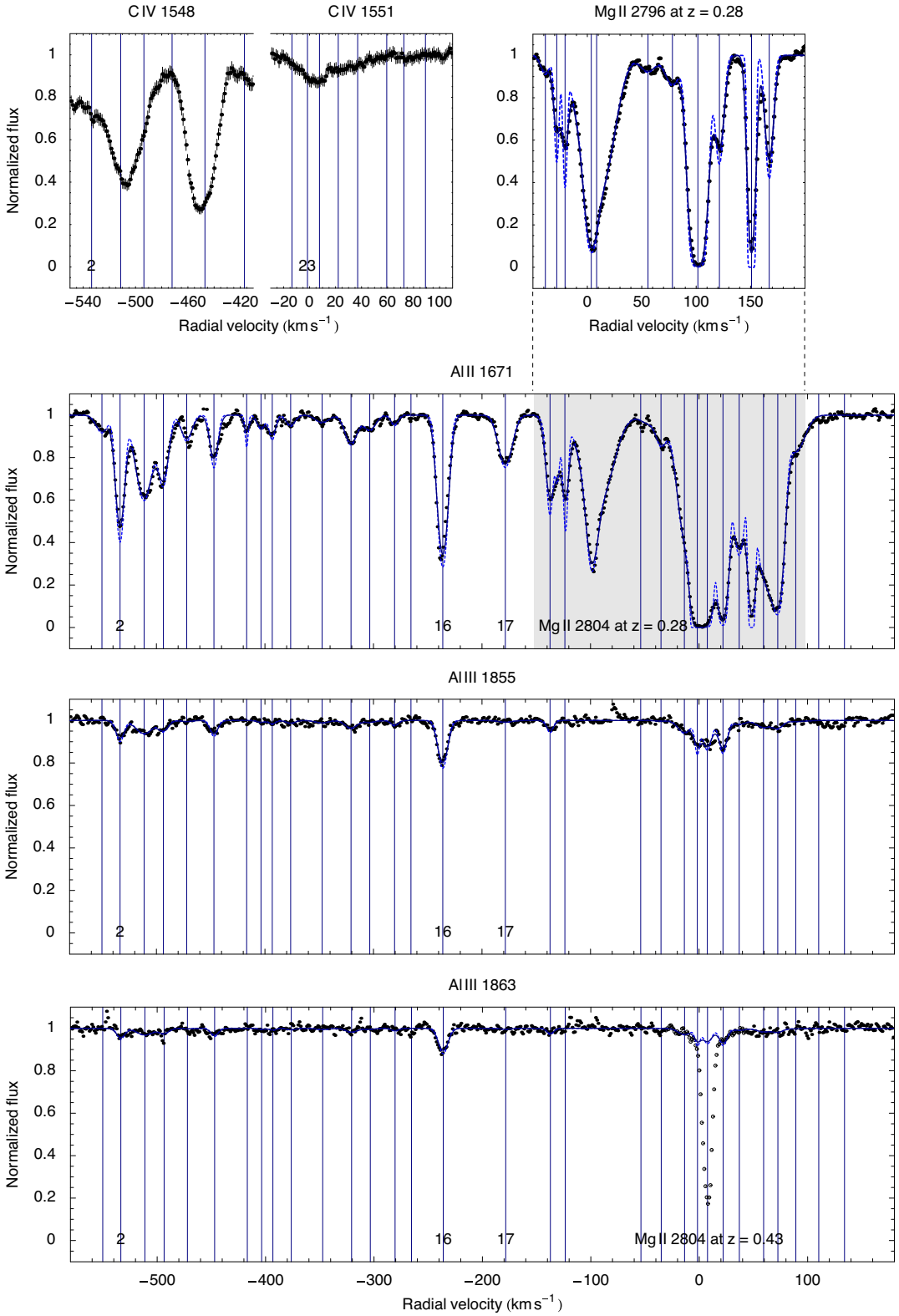

Fig. 2. continued. Note that the Al II profile is blended with an Mg II ensemble at redshift $z = 0.28$. Blended parts of the C IV profiles are omitted for convenience

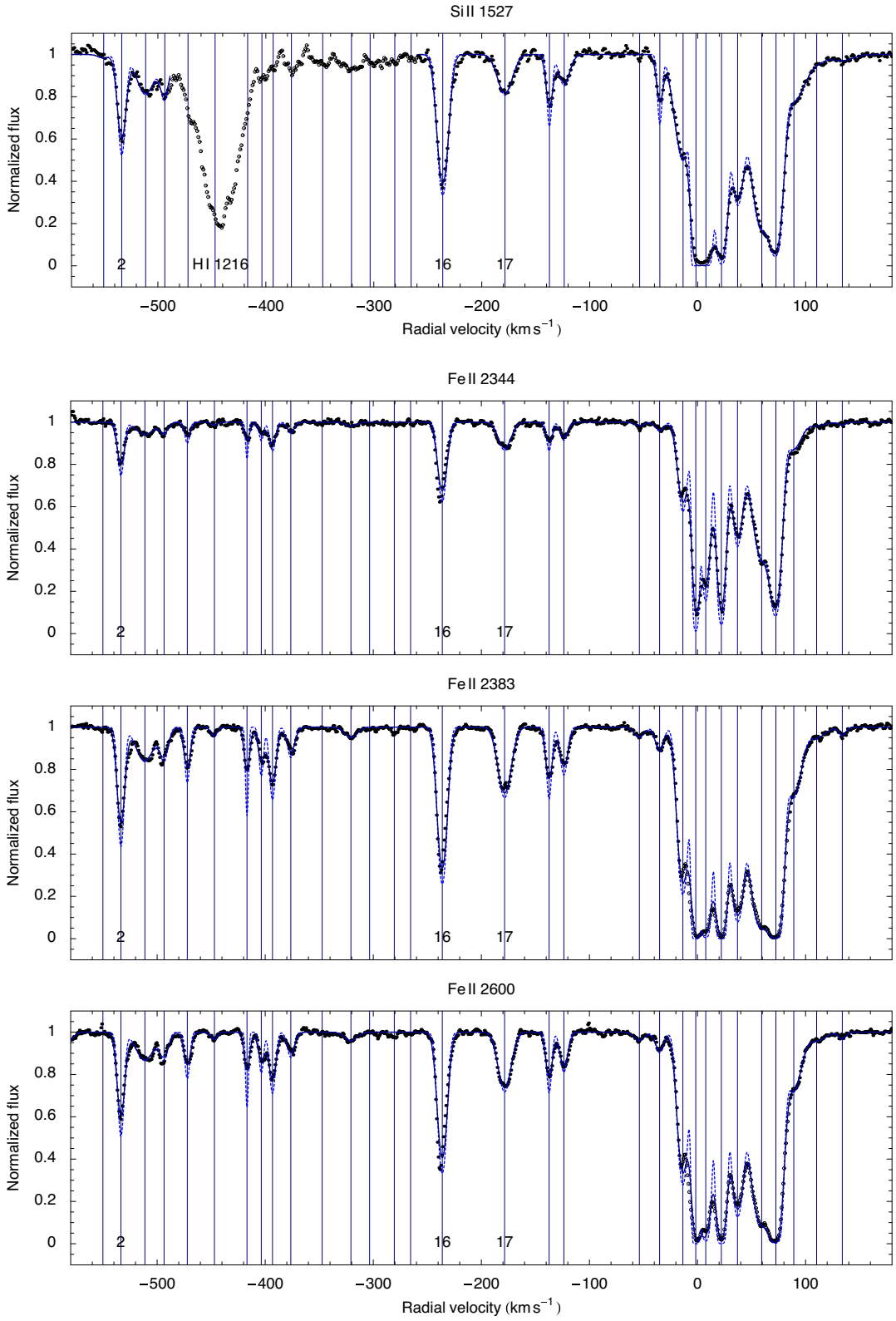

Fig. 2. continued.

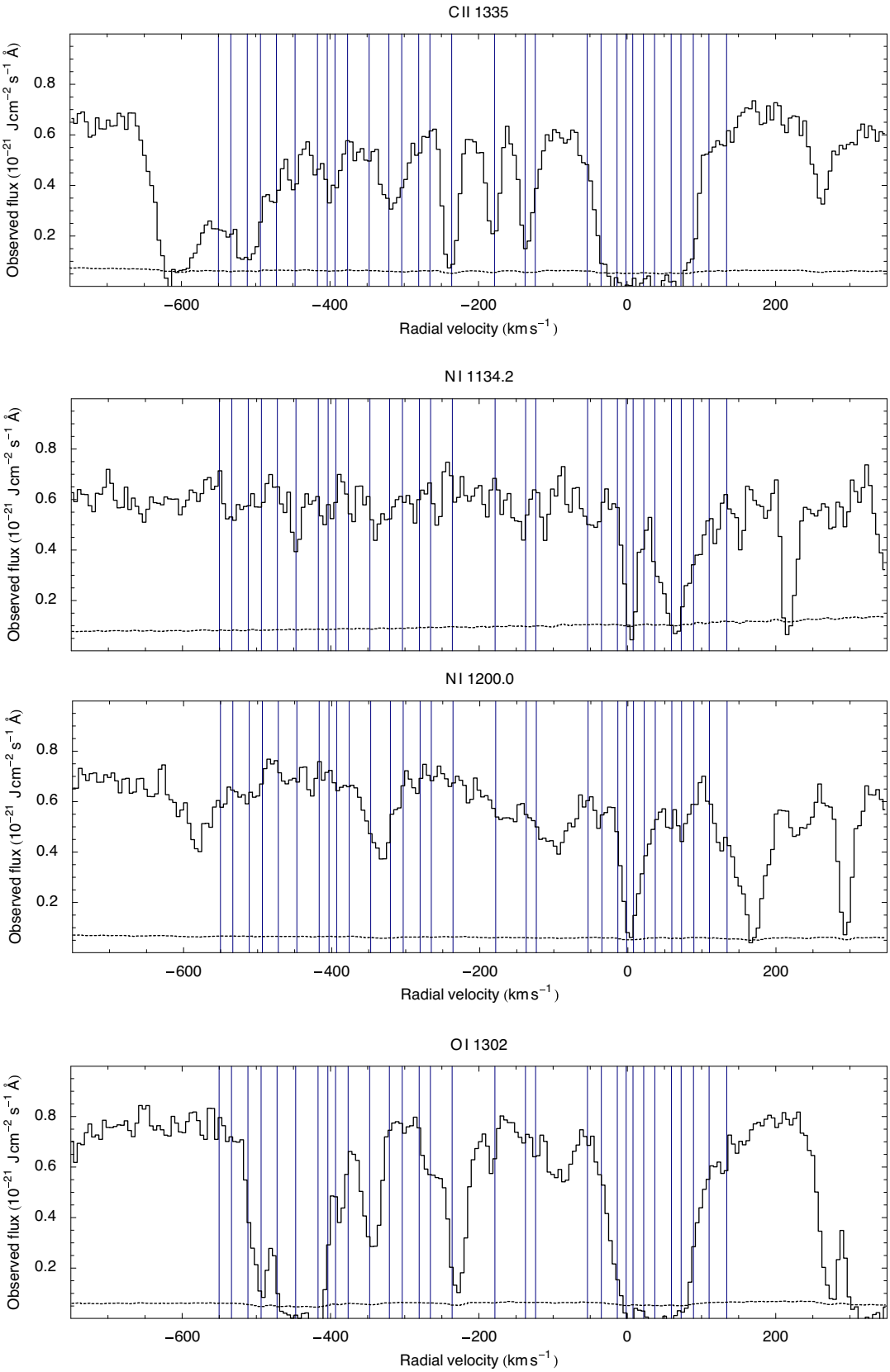

Fig. 5. Associated metal lines recorded with the STIS spectrograph. The solid and dashed lines mark the observed flux and its standard deviation, respectively. Positions of associated metal lines found with UVES are indicated by vertical lines. Note that many lines are blended within the Lyman forest

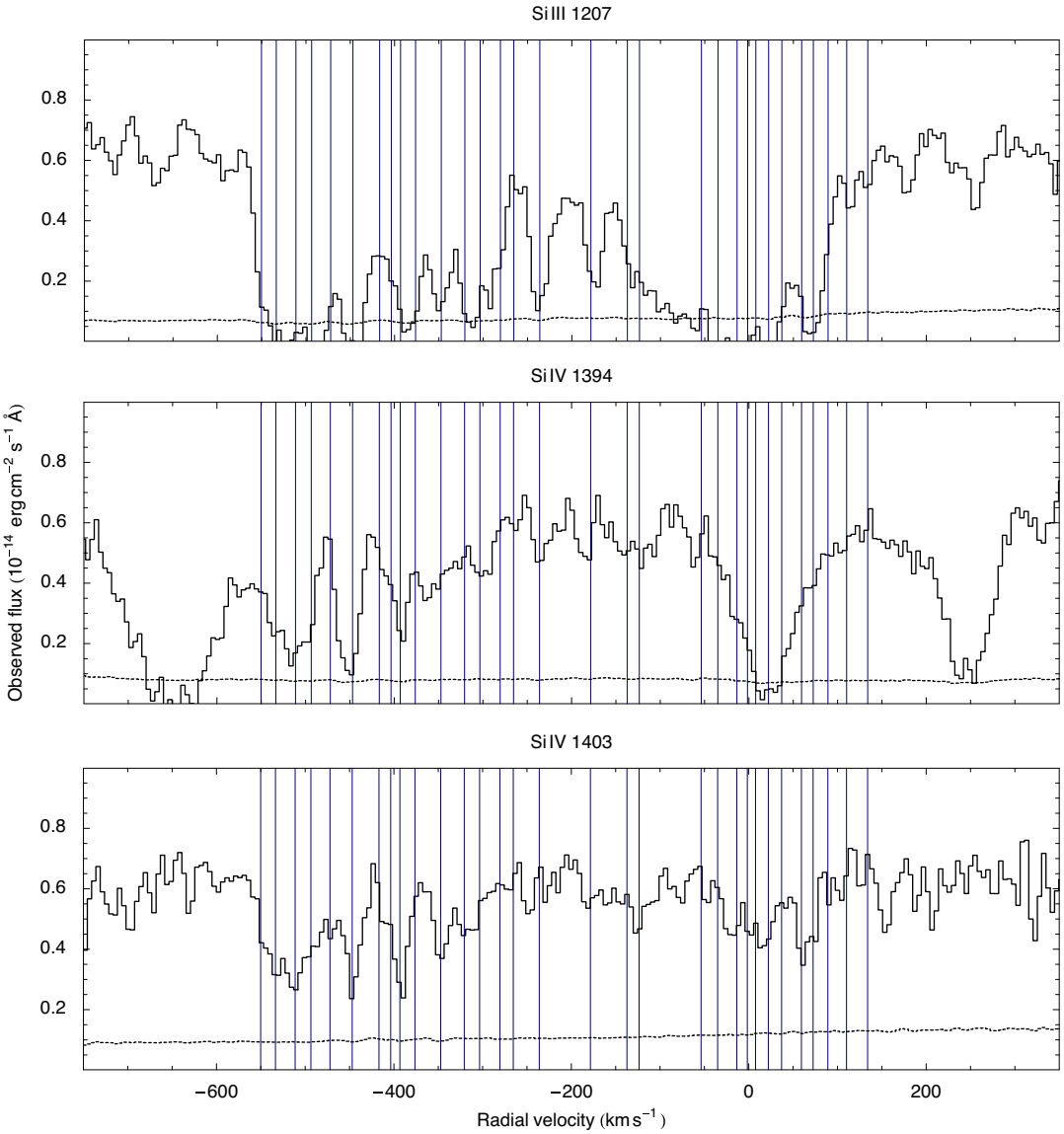

Fig. 5. continued.

Table 3. Optimized decomposition of the metal lines shown in Figs. 2 and 3

No.	Transitions		RV (km s^{-1})	b (km s^{-1})	log N (cm^{-2})
1	Mg II	2796, 2804	−550.20 ± 0.15	6.59 ± 0.25	11.79 ± 0.02
1	Al II	1671	−550.20	7.26 ± 1.39	11.17 ± 0.08
1	Si II	1527, 1808	−550.20 ± 0.15	6.59 ± 0.25	11.61 ± 0.30
2	Mg I	2026, 2853	−533.51 ± 0.03	5.21 ± 0.34	11.08 ± 0.02
2	Mg II	2796, 2804	−533.51 ± 0.03	5.12 ± 0.05	12.90 ± 0.01
2	Al II	1671	−533.5	4.79 ± 0.25	12.00 ± 0.01
2	Al III	1855, 1863	−533.5	4.79 ± 0.25	11.51 ± 0.07
2	Si II	1527, 1808	−533.51 ± 0.03	4.45 ± 0.37	12.97 ± 0.03
2	Fe II	1608, 2344, 2374, 2383, 2587, 2600	−533.51 ± 0.03	3.73 ± 0.10	12.43 ± 0.01
3	Mg I	2026, 2853	−511.33 ± 0.07	9.24 ± 0.75	10.94 ± 0.04
3	Mg II	2796, 2804	−511.33 ± 0.07	9.96 ± 0.14	12.83 ± 0.01
3	Al II	1671	−511.33	10.03 ± 0.45	12.08 ± 0.01
3	Al III	1855, 1863	−511.33	10.03 ± 0.45	11.63 ± 0.07
3	Si II	1527, 1808	−511.33 ± 0.07	11.20 ± 1.53	12.89 ± 0.05
3	Fe II	1608, 2344, 2374, 2383, 2587, 2600	−511.33 ± 0.07	11.06 ± 0.33	12.24 ± 0.01
4	Mg I	2026, 2853	−493.59 ± 0.08	6.86 ± 0.85	10.76 ± 0.05
4	Mg II	2796, 2804	−493.59 ± 0.08	6.80 ± 0.12	12.53 ± 0.01
4	Al II	1671	−493.59	6.00 ± 0.46	11.73 ± 0.03
4	Al III	1855, 1863	−493.59	6.00 ± 0.46	11.31 ± 0.10
4	Si II	1527, 1808	−493.59 ± 0.08	5.43 ± 1.36	12.61 ± 0.08
4	Fe II	1608, 2344, 2374, 2383, 2587, 2600	−493.59 ± 0.08	5.06 ± 0.29	11.86 ± 0.02
5	Mg I	2026, 2853	−472.09 ± 0.06	6.88 ± 0.81	10.62 ± 0.05
5	Mg II	2796, 2804	−472.09 ± 0.06	5.24 ± 0.13	12.19 ± 0.01
5	Al II	1671	−472.09	6.36 ± 0.91	11.29 ± 0.06
5	Al III	1855, 1863	−472.09	6.36 ± 0.91	10.36 ± 0.69
5	Fe II	1608, 2344, 2374, 2383, 2587, 2600	−472.09 ± 0.06	3.12 ± 0.19	11.92 ± 0.02
6	Mg I	2026, 2853	−447.00 ± 0.08	6.54 ± 0.87	10.50 ± 0.06
6	Mg II	2796, 2804	−447.00 ± 0.08	7.30 ± 0.13	12.29 ± 0.01
6	Al II	1671	−447.00	4.46 ± 0.44	11.47 ± 0.03
6	Al III	1855, 1863	−447.00	4.46 ± 0.44	11.35 ± 0.09
6	Fe II	1608, 2344, 2374, 2383, 2587, 2600	−447.00 ± 0.08	3.81 ± 1.21	11.19 ± 0.07
7	Mg I	2026, 2853	−416.85 ± 0.06	5.00 ± 1.18	10.43 ± 0.08
7	Mg II	2796, 2804	−416.85 ± 0.06	3.29 ± 0.17	11.87 ± 0.01
7	Al II	1671	−416.85	1.88 ± 1.45	10.85 ± 0.10
7	Fe II	1608, 2344, 2374, 2383, 2587, 2600	−416.85 ± 0.06	1.72 ± 0.20	11.91 ± 0.02
8	Mg II	2796, 2804	−403.63 ± 0.09	2.63 ± 0.22	11.78 ± 0.02
8	Al II	1671	−403.63	4.68 ± 1.96	10.87 ± 0.12
8	Al III	1855, 1863	−403.63	4.68 ± 1.96	10.48 ± 0.27
8	Fe II	1608, 2344, 2374, 2383, 2587, 2600	−403.63 ± 0.09	2.82 ± 0.34	11.81 ± 0.02
9	Mg I	2026, 2853	−393.26 ± 0.08	6.02 ± 0.93	10.58 ± 0.07
9	Mg II	2796, 2804	−393.26 ± 0.08	5.56 ± 0.21	12.15 ± 0.01
9	Al II	1671	−393.26	3.81 ± 1.33	11.04 ± 0.08
9	Al III	1855, 1863	−393.26	3.81 ± 1.33	10.66 ± 0.30
9	Fe II	1608, 2344, 2374, 2383, 2587, 2600	−393.26 ± 0.08	3.63 ± 0.19	12.13 ± 0.01
10	Mg II	2796, 2804	−376.31 ± 0.13	6.02 ± 0.26	11.80 ± 0.02
10	Al II	1671	−376.31	5.41 ± 1.72	10.83 ± 0.12
10	Al III	1855, 1863	−376.31	5.41 ± 1.72	10.70 ± 0.30
10	Fe II	1608, 2344, 2374, 2383, 2587, 2600	−376.31 ± 0.13	4.37 ± 0.24	11.77 ± 0.02

Table 3. continued.

No.	Transitions		RV (km s^{-1})	b (km s^{-1})	log N (cm^{-2})
11	Mg II	2796, 2804	−347.31 ± 0.23	8.56 ± 0.38	11.64 ± 0.02
11	Al II	1671	−347.31	8.36 ± 4.21	10.85 ± 0.15
11	Al III	1855, 1863	−347.31	8.36 ± 4.21	10.80 ± 0.37
12	Mg II	2796, 2804	−320.68 ± 0.11	7.41 ± 0.22	12.07 ± 0.01
12	Al II	1671	−320.68	7.41 ± 0.95	11.41 ± 0.05
12	Al III	1855, 1863	−320.68	7.41 ± 0.95	11.26 ± 0.12
12	Fe II	1608, 2344, 2374, 2383, 2587, 2600	−320.68 ± 0.11	7.80 ± 0.70	11.55 ± 0.04
13	Mg II	2796, 2804	−303.41 ± 0.32	6.59 ± 0.43	11.44 ± 0.03
13	Al II	1671	−303.41	7.34 ± 1.39	11.11 ± 0.09
13	Al III	1855, 1863	−303.41 ± 0.32	7.34 ± 1.39	10.64 ± 0.30
14	Mg II	2796, 2804	−280.56 ± 0.15	3.19 ± 0.31	11.46 ± 0.02
14	Al II	1671	−280.56	4.45 ± 1.37	10.73 ± 0.11
14	Al III	1855, 1863	−280.56	4.45 ± 1.37	10.87 ± 0.20
15	Mg II	2796, 2804	−265.46 ± 0.38	4.31 ± 0.71	11.11 ± 0.05
16	Mg I	2026, 2853	−236.14 ± 0.02	6.04 ± 0.26	11.20 ± 0.02
16	Mg II	2796, 2804	−236.14 ± 0.02	6.25 ± 0.04	13.23 ± 0.01
16	Al II	1671	−236.14	5.72 ± 0.15	12.22 ± 0.01
16	Al III	1855, 1863	−236.14	5.72 ± 0.15	11.97 ± 0.03
16	Si II	1527, 1808	−236.14 ± 0.02	5.95 ± 0.17	13.33 ± 0.01
16	Fe II	1608, 2344, 2374, 2383, 2587, 2600	−236.14 ± 0.02	5.09 ± 0.06	12.78 ± 0.01
17	Mg I	2026, 2853	−178.49 ± 0.05	6.60 ± 0.57	10.74 ± 0.04
17	Mg II	2796, 2804	−178.49 ± 0.05	8.44 ± 0.09	12.51 ± 0.01
17	Al II	1671	−178.49	8.28 ± 0.47	11.73 ± 0.02
17	Al III	1855, 1863	−178.49	8.28 ± 0.47	10.66 ± 0.30
17	Si II	1527, 1808	−178.49 ± 0.05	9.04 ± 0.47	12.80 ± 0.03
17	Fe II	1608, 2344, 2374, 2383, 2587, 2600	−178.49 ± 0.05	7.77 ± 0.13	12.44 ± 0.01
18	Mg I	2026, 2853	−137.31 ± 0.04	2.74 ± 0.86	10.44 ± 0.06
18	Mg II	2796, 2804	−137.31 ± 0.04	3.89 ± 0.08	12.44 ± 0.01
18	Al II	1671	−137.31	3.96 ± 0.36	11.74 ± 0.02
18	Al III	1855, 1863	−137.31	3.96 ± 0.36	11.18 ± 0.11
18	Si II	1527, 1808	−137.31 ± 0.04	3.07 ± 0.35	12.62 ± 0.03
18	Fe II	1608, 2344, 2374, 2383, 2587, 2600	−137.31 ± 0.04	3.12 ± 0.16	12.06 ± 0.01
19	Mg I	2026, 2853	−123.63 ± 0.07	5.39 ± 3.06	10.20 ± 0.11
19	Mg II	2796, 2804	−123.63 ± 0.07	5.01 ± 0.13	12.18 ± 0.01
19	Al II	1671	−123.63	3.48 ± 0.75	11.41 ± 0.05
19	Si II	1527, 1808	−123.63 ± 0.07	6.55 ± 0.58	12.54 ± 0.05
19	Fe II	1608, 2344, 2374, 2383, 2587, 2600	−123.63 ± 0.07	4.49 ± 0.22	12.01 ± 0.02
20	Fe II	1608, 2344, 2374, 2383, 2587, 2600	−53.77 ± 0.52	6.38 ± 0.84	11.45 ± 0.05
21	Mg I	2026, 2853	−35.06 ± 0.16	6.32 ± 1.56	10.53 ± 0.07
21	Al II	1671	−35.06	6.19 ± 1.02	11.29 ± 0.06
21	Al III	1855, 1863	−35.06	6.19 ± 1.02	10.11 ± 1.37
21	Si II	1527, 1808	−35.06 ± 0.16	2.76 ± 0.38	12.56 ± 0.04
21	Fe II	1608, 2344, 2374, 2383, 2587, 2600	−35.06 ± 0.16	5.08 ± 0.45	11.75 ± 0.03
22	Mg I	2026, 2853	−13.53 ± 0.07	8.52 ± 0.51	11.23 ± 0.02
22	Al II	1671	−13.53	7.98 ± 0.37	12.16 ± 0.02
22	Al III	1855, 1863	−13.53	7.98 ± 0.37	11.50 ± 0.08
22	Si II	1527, 1808	−13.53 ± 0.07	9.97 ± 0.24	13.36 ± 0.01
22	Ca II	3935	−13.53 ± 0.07	7.89 ± 0.97	11.16 ± 0.04

Table 3. continued.

No.	Transitions		RV (km s^{-1})	b (km s^{-1})	log N (cm^{-2})
22	Fe II	1608, 2344, 2374, 2383, 2587, 2600	−13.53 ± 0.07	5.79 ± 0.10	12.90 ± 0.01
23	Mg I	2026, 2853	−1.61 ± 0.03	2.16 ± 0.05	12.41 ± 0.03
23	Al II	1671	−1.61	3.05	13.86 ± 0.17
23	Al III	1855, 1863	−1.61	3.05	11.50 ± 0.06
23	Si I	2515	−1.61 ± 0.03	2.17 ± 2.10	11.34 ± 0.08
23	Si II	1527, 1808	−1.61 ± 0.03	3.05 ± 0.09	14.28 ± 0.03
23	S I	1807	−1.61 ± 0.03	1.56 ± 1.12	12.18 ± 0.05
23	Ca II	3935	−1.61 ± 0.03	2.15 ± 0.10	12.12 ± 0.02
23	Cr II	2056, 2062	−1.61 ± 0.03	2.97 ± 0.05	11.84 ± 0.06
23	Mn II	2577, 2594, 2606	−1.61 ± 0.03	2.97 ± 0.05	11.51 ± 0.03
23	Fe I	2484, 2524	−1.61 ± 0.03	0.48 ± 0.18	11.30 ± 0.06
23	Fe II	1608, 2344, 2374, 2383, 2587, 2600	−1.61 ± 0.03	2.97 ± 0.05	13.51 ± 0.01
23	Ni II	1710, 1742, 1752	−1.61 ± 0.03	2.97 ± 0.05	12.48 ± 0.04
23	Zn II	2026, 2063	−1.61 ± 0.04	2.97 ± 0.05	11.79 ± 0.02
24	Mg I	2026, 2853	7.63 ± 0.06	4.09 ± 0.12	11.90 ± 0.01
24	Al II	1671	7.63	5.36	12.82 ± 0.04
24	Al III	1855, 1863	7.63	5.36	11.72 ± 0.05
24	Si II	1527, 1808	7.63 ± 0.06	5.36 ± 0.25	14.16 ± 0.04
24	Ca II	3935	7.63 ± 0.06	3.17 ± 0.17	11.78 ± 0.01
24	Cr II	2056, 2062	7.63 ± 0.06	4.92 ± 0.13	11.61 ± 0.14
24	Mn II	2577, 2594, 2606	7.63 ± 0.06	4.92 ± 0.13	11.36 ± 0.03
24	Fe II	1608, 2344, 2374, 2383, 2587, 2600	7.63 ± 0.06	4.92 ± 0.13	13.36 ± 0.01
24	Ni II	1710, 1742, 1752	7.63 ± 0.06	4.92 ± 0.13	12.33 ± 0.06
24	Zn II	2026, 2063	7.63 ± 0.06	4.92 ± 0.13	11.59 ± 0.03
25	Mg I	2026, 2853	22.06 ± 0.03	5.68 ± 0.14	11.78 ± 0.01
25	Al II	1671	22.06	4.85 ± 0.20	12.69 ± 0.02
25	Al III	1855, 1863	22.06	4.85 ± 0.20	11.72 ± 0.05
25	Si II	1527, 1808	22.06 ± 0.03	4.99 ± 0.23	13.89 ± 0.03
25	Ca II	3935	22.06 ± 0.03	4.37 ± 0.21	11.74 ± 0.01
25	Cr II	2056, 2062	22.06 ± 0.03	4.29 ± 0.06	11.77 ± 0.07
25	Mn II	2577, 2594, 2606	22.06 ± 0.03	4.29 ± 0.06	11.34 ± 0.03
25	Fe II	1608, 2344, 2374, 2383, 2587, 2600	22.06 ± 0.03	4.29 ± 0.06	13.53 ± 0.01
25	Ni II	1710, 1742, 1752	22.06 ± 0.03	4.29 ± 0.06	12.37 ± 0.06
25	Zn II	2026, 2063	22.06 ± 0.03	4.29 ± 0.06	11.03 ± 0.08
26	Mg I	2026, 2853	36.99 ± 0.07	5.68 ± 0.23	11.43 ± 0.02
26	Al II	1671	37.00	7.33 ± 0.43	12.26 ± 0.02
26	Al III	1855, 1863	37.00	7.33 ± 0.43	10.97 ± 0.20
26	Si II	1527, 1808	37.00 ± 0.07	7.26 ± 0.39	13.47 ± 0.02
26	Ca II	3935	37.00 ± 0.07	6.22 ± 0.22	11.75 ± 0.01
26	Cr II	2056, 2062	37.00 ± 0.07	6.32 ± 0.14	11.52 ± 0.10
26	Mn II	2577, 2594, 2606	37.00 ± 0.07	6.32 ± 0.14	10.73 ± 0.11
26	Fe II	1608, 2344, 2374, 2383, 2587, 2600	37.00 ± 0.07	6.32 ± 0.14	13.14 ± 0.01
26	Ni II	1710, 1742, 1752	37.00 ± 0.07	6.32 ± 0.14	12.02 ± 0.12
26	Zn II	2026, 2063	37.00 ± 0.07	6.32 ± 0.14	10.98 ± 0.10
27	Mg I	2026, 2853	59.39 ± 0.19	11.53 ± 0.40	11.72 ± 0.02
27	Al II	1671	59.39	8.71 ± 1.12	12.43 ± 0.04
27	Al III	1855, 1863	59.39	8.71 ± 1.12	11.29 ± 0.13
27	Si II	1527, 1808	59.39 ± 0.19	10.96 ± 0.50	13.81 ± 0.01
27	Ca II	3935	59.39 ± 0.19	8.53 ± 0.33	11.87 ± 0.02
27	Cr II	2056, 2062	59.39 ± 0.19	11.07 ± 0.28	11.29 ± 0.26
27	Mn II	2577, 2594, 2606	59.39 ± 0.19	11.07 ± 0.28	11.18 ± 0.05
27	Fe II	1608, 2344, 2374, 2383, 2587, 2600	59.39 ± 0.19	11.07 ± 0.28	13.47 ± 0.01
27	Ni II	1710, 1742, 1752	59.39 ± 0.19	11.07 ± 0.28	12.27 ± 0.08
27	Zn II	2026, 2063	59.39 ± 0.19	11.07 ± 0.28	11.41 ± 0.07

Table 3. continued.

No.	Transitions		RV (km s^{-1})	b (km s^{-1})	log N (cm^{-2})
28	Mg I	2026, 2853	72.54 ± 0.06	6.03 ± 0.15	11.77 ± 0.01
28	Al II	1671	72.54	6.14 ± 0.15	12.57 ± 0.02
28	Al III	1855, 1863	72.54	6.14 ± 0.15	11.17 ± 0.13
28	Si II	1527, 1808	72.54 ± 0.06	6.45 ± 0.18	13.75 ± 0.02
28	Ca II	3935	72.54 ± 0.06	5.52 ± 0.13	12.08 ± 0.01
28	Cr II	2056, 2062	72.54 ± 0.06	5.81 ± 0.09	11.92 ± 0.06
28	Mn II	2577, 2594, 2606	72.54 ± 0.06	5.81 ± 0.09	11.34 ± 0.03
28	Fe II	1608, 2344, 2374, 2383, 2587, 2600	72.54 ± 0.06	5.81 ± 0.09	13.51 ± 0.01
28	Ni II	1710, 1742, 1752	72.54 ± 0.06	5.81 ± 0.09	12.32 ± 0.06
28	Zn II	2026, 2063	72.54 ± 0.06	5.81 ± 0.09	10.72 ± 0.11
29	Mg I	2026, 2853	89.11 ± 0.20	10.85 ± 0.75	11.08 ± 0.04
29	Al II	1671	89.11	11.24 ± 1.11	11.69 ± 0.04
29	Al III	1855, 1863	89.11	11.24 ± 1.11	10.59 ± 0.45
29	Si II	1527, 1808	89.11 ± 0.20	13.15 ± 1.35	13.04 ± 0.06
29	Ca II	3935	89.11 ± 0.20	10.89 ± 1.13	11.23 ± 0.05
29	Fe II	1608, 2344, 2374, 2383, 2587, 2600	89.11 ± 0.20	9.03 ± 0.49	12.50 ± 0.02
30	Si II	1527, 1808	110.24 ± 1.43	11.46 ± 5.77	12.12 ± 0.29
30	Fe II	1608, 2344, 2374, 2383, 2587, 2600	110.24 ± 1.43	10.94 ± 1.93	11.70 ± 0.08
31	Si II	1527, 1808	134.00 ± 0.58	13.30 ± 8.35	12.12 ± 0.31
31	Fe II	1608, 2344, 2374, 2383, 2587, 2600	134.00 ± 0.58	4.33 ± 1.22	11.22 ± 0.07

Revised manuscript. The original version was published in A&A 415, L7–L11 (2004)

Probing the variability of the fine-structure constant with the VLT UVES⋆

R. Quast[1], D. Reimers[1], and S. A. Levshakov[2]

[1] Hamburger Sternwarte, Universität Hamburg, Gojenbergsweg 112, D-21029 Hamburg, Germany
e-mail: {rquast,rbaade,dreimers}@hs.uni-hamburg.de
[2] Department of Theoretical Astrophysics, Ioffe Physico-Technical Institute, 194021 St. Petersburg, Russia
e-mail: lev@astro.ioffe.rssi.ru

Received 11 November 2003 / Accepted 22 December 2003 / Revised 6 December 2005

ABSTRACT

Aims. We study an ensemble of Fe II λ1608, λ2344, λ2374, λ2383, λ2587, and λ2600 QSO absorption lines with redshift 1.15 to assess the cosmological variability of the fine-structure constant α hypothesized by unification theories.
Methods. We used the VLT UVES spectrograph to obtain high-resolution high signal-to-noise spectra of HE 0515–4414. The variation of α is measured using both the standard many-multiplet method and an equivalent linear regression technique factoring in systematic errors.
Results. We obtain $\langle\Delta\alpha/\alpha\rangle = (0.1 \pm 1.7) \times 10^{-6}$ and $\langle\Delta\alpha/\alpha\rangle = (-0.4 \pm 1.9 \pm 2.7_{\rm sys}) \times 10^{-6}$ which are the most stringent bounds yet inferred from an individual QSO absorption line system. The null hypothesis $\langle\Delta\alpha/\alpha\rangle = 0$ is contradicted at a significance level of 9 percent, whereas the former measurements based on HIRES spectra resulting in $\langle\Delta\alpha/\alpha\rangle = -5.7 \times 10^{-6}$ are contradicted at 88 percent.

Key words. cosmology: observations – quasars: absorption lines – quasars: individual: HE 0515–4414

1. Introduction

Modern 10 m class telescopes equipped with instruments like the High-Resolution Echelle Spectrograph (HIRES) at the Keck Observatory or the UV-Visual Echelle Spectrograph (UVES) at the ESO Very Large Telescope (VLT) facilitate the accurate observation of QSO absorption (or emission) lines in order to study the hypothetical variability of fundamental physical constants like the fine-structure constant $\alpha = e^2/(4\pi\epsilon_0\hbar c)$ or the proton-electron mass ratio $\mu = m_{\rm p}/m_{\rm e}$. The interest in these studies is motivated by the unification theories incorporating varying fundamental constants (for a review see, e.g., Uzan 2003).

From the astronomical point of view the cosmological variability of the fine-structure constant is assessed as

$$\Delta\alpha/\alpha = (\alpha_z - \alpha_0)/\alpha_0, \quad (1)$$

where α_0 and α_z denote the values of the fine-structure constant in the laboratory and the specific absorption (or emission) line system at redshift z, respectively. While observational studies considering the fine-structure splitting of intergalactic alkali-doublet (AD) absorption lines (see, e.g., Levshakov 1994; Murphy et al. 2001b) or intrinsic QSO emission line doublets (Bahcall et al. 2004) provided robust upper bounds on $|\Delta\alpha/\alpha|$, recently Murphy et al. (2004, hereafter MFW04) have detected a non-zero expectation value $\langle\Delta\alpha/\alpha\rangle$ for a sample of 143 complex metal absorption systems identified in QSO spectra recorded with the HIRES spectrograph: $\langle\Delta\alpha/\alpha\rangle = (-5.7 \pm 1.1) \times 10^{-6}$ in the redshift range $0.2 < z < 4.2$. This remarkable statistical evidence for a cosmological variation of the fine-structure constant is achieved by means of the many-multiplet (MM) technique, which is a generalization of the AD method incorporating the multi-component profile decomposition of many transitions from different multiplets of different ionic species (Dzuba et al. 1999; Murphy et al. 2003, hereafter MWF03, and references therein).

While the MM technique considerably improves the formal accuracy, it also shows intrinsic deficiencies. Levshakov (2004) illustrates in detail that the prerequisite assumption that the spatial distribution is the same for all ionic species is not valid in typical intergalactic absorption systems. Consequently, it is more reliable to apply the MM technique to samples of absorption lines arising from solely one ionic species. Furthermore, in comparison to the AD calculations the incorporation of more transitions over a wider wavelength range results in a stronger susceptibility to systematic effects. Nevertheless, sources of error like wavelength miscalibration, spectrograph temperature variations, atmospheric dispersion, and isotopic or hyperfine-structure effects do demonstrably not explain the detected non-

Send offprint requests to: R. Quast

⋆ Based on observations made with ESO Telescopes at the La Silla or Paranal Observatories under programme ID 066.A-0212.

zero expectation value (Murphy et al. 2001a, 2003, 2004). The observational discrepancy grows since the radioactive decay rates of certain long-lived nuclei deduced from geophysical and meteoritic data provide a stringent bound, $\langle \Delta\alpha/\alpha \rangle = (8 \pm 8) \times 10^{-7}$, back to the epoch of Solar system formation, $z \leq 0.45$ (Olive et al. 2004).

In the optical spectroscopy, the most striking deficiency inherent to all decomposition techniques are non-linear inter-parameter correlations preventing the accurate optimization of the model parameters and possibly causing ambigous results. In fact, the spectral resolution attained in QSO observations at the 10 m class telescopes is still not sufficient to resolve the metal lines with an expected minimum thermal width of about 1 km s^{-1}. Clearly, in order to solve the profile decomposition problem spectral observations with the highest possible resolution and the highest possible signal-to-noise ratio are desirable.

In this study, we present exceptional high-resolution and high signal-to-noise spectra of the notably bright intermediate redshift QSO HE 0515–4414 (Reimers et al. 1998, $z = 1.73$, $B = 15.0$) obtained with the UVES spectrograph. The spectra exhibit a multi-component complex of metal absorption lines associated with a sub-damped Ly α (sub-DLA) system at redshift $z = 1.15$ (de la Varga et al. 2000; Quast et al. 2002; Reimers et al. 2003). We analyze a homogenous subsample of Fe II λ1608, λ2344, λ2374, λ2383, λ2587, and λ2600 absorption lines by means of the standard and the regression MM techniques to assess the cosmological variability of the fine-structure constant.

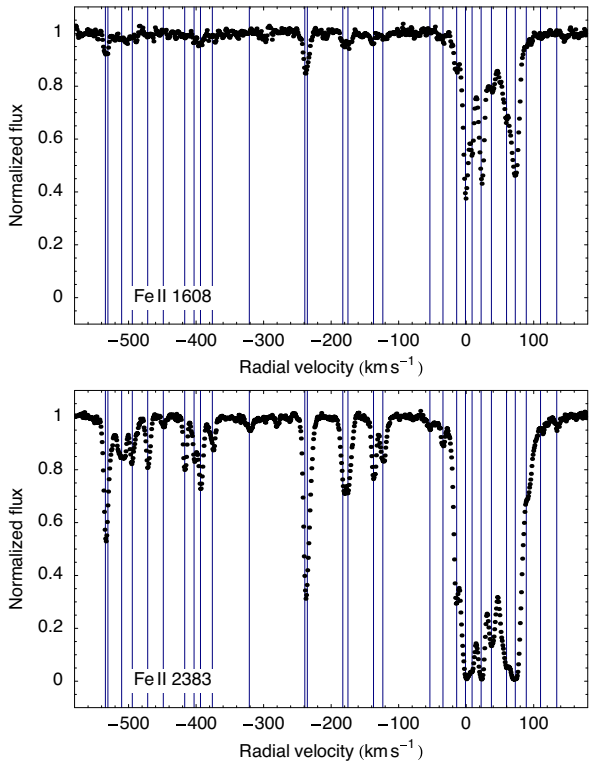

Fig. 1. Multi-component Fe II absorption complex at redshift $z = 1.15$. For convenience, only the transitions λ1608 and λ2383 are shown. Individual components are marked by vertical lines. Radial velocity zero corresponds to the redhsift $z = 1.1508$. A close-up ranging from -20 to 100 km s^{-1} is provided in Fig. 2

2. Observations

HE 0515–4414 was observed with UVES during ten nights between October 7, 2000 and January 3, 2001. Thirteen exposures were made in the dichroic mode using standard settings for the central wavelenghts of 3460/4370 Å in the blue, and 5800/8600 Å in the red. The CCDs were read out in fast mode without binning. Individual exposure times were 3600 and 4500 s, under photometric to clear sky and seeing conditions ranging from 0.47 to 0.70 arcsec. The slit width was 0.8 arcsec providing a spectral resolution of about 55 000 in the blue and slightly less in the red. The ThAr lamp exposures taken immediately after each science exposure provide an accurate calibration in wavelength. The standard deviation of the wavelength versus pixel dispersion solution is about 2.0 mÅ (2.5 mÅ) in the blue (red), resulting in an absolute accuracy of about 0.15 km s^{-1} in radial velocity space.

The raw data frames were reduced at the ESO Quality Control Garching using the UVES pipeline Data Reduction Software. The calibrated spectra were converted to vacuum wavelengths according to Edlén (1966) while the barycentric velocity correction was manually cross-checked using the ESO-Munich Image Data Analysis Software and the Image Reduction and Analysis Facility.

The individual vacuum-barycentric corrected spectra were manually cleaned from cosmic rays or pixel defects, rescaled to a common median flux level, and resampled to an equidistant wavelength grid by means of natural cubic spline interpolation. The combined spectra (Fig. 1) show an effective signal-to-noise ratio per pixel typically better than 100.

3. Analysis

3.1. The standard MM technique

The observed spectral flux $F(\lambda)$ is modelled as the product of the background continuum $C(\lambda)$ and the absorption term convoluted with the instrumental profile, i.e., $F(\lambda) = C(\lambda) \int P(\xi)\, \mathrm{e}^{-\tau(\lambda-\xi)}\, \mathrm{d}\xi$. While the background continuum is locally approximated by an optimized linear combination of Legendre polynomials of up to second order, the instrumental profile is modelled by a normalized Gaussian given by the the spectral resolution of the instrument. Assuming pure Doppler broadening, the optical depth $\tau(\lambda)$ is a superposition of Gaussian functions

$$g_i(\lambda) = \frac{e^2}{4\epsilon_0 mc} \frac{N_i f_i \lambda_i}{\sqrt{\pi} b_i} \exp\left[-\left(\frac{c}{b_i} \frac{\lambda - Z_i \lambda_{\alpha,i}}{Z_i \lambda_{\alpha,i}} \right)^2 \right], \quad (2)$$

where $Z_i = (1 + z_i)(1 + v_i/c)$ while $\lambda_{\alpha,i}$, f_i, z_i, v_i, b_i, and N_i denote, respectively, the systemic rest wavelength, the oscillator strength, the cosmological redshift, the radial velocity, the line broadening velocity, and the column density corresponding to the line i. The systemic rest wavenumber $\omega_{\alpha,i} = 1/\lambda_{\alpha,i}$ is parametrized as

$$\omega_{\alpha,i} = \omega_i + q_i\, (\Delta\alpha/\alpha)\, (2 + \Delta\alpha/\alpha), \quad (3)$$

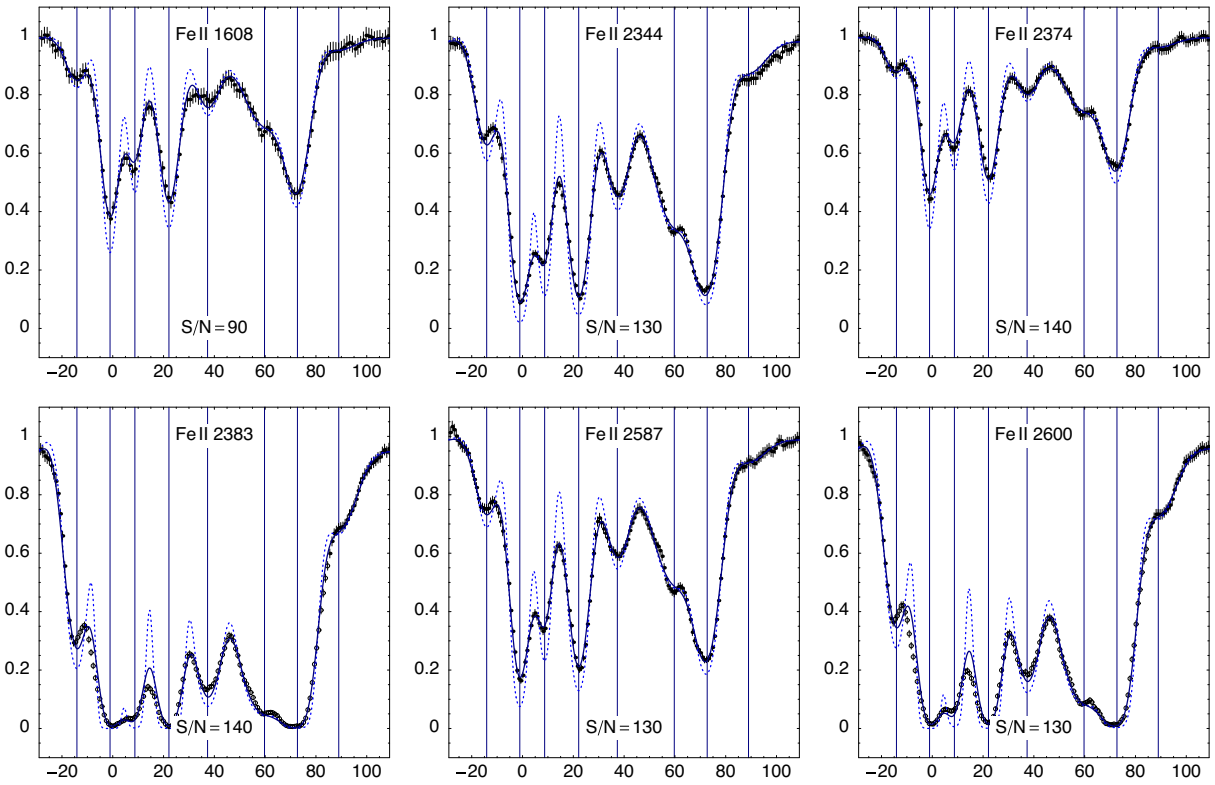

Fig. 2. Close-up of Fig. 1 showing the subset of line profiles associated with the central region of the sub-DLA system. The solid and dashed curves represent the optimized model and its deconvolution, respectively. The standard deviation of the normalized flux is indicated by vertical bars whereas the effective signal-to-noise ratio per pixel is stated explicitly. Data marked by empty circles are ignored in the optimization

where $\omega_i = 1/\lambda_i$ is the wavenumber in the laboratory and q_i is the relativistic correction coefficient (Dzuba et al. 2002).

Even though the sub-DLA system exhibits many additional metal absorption lines (Al II, Al III, Mg I, Mg II, Si II, Cr II, Ni II, and Zn II) typically incorporated in the standard MM analysis, we decide to apply this technique to the Fe II transitions only. The restriction to one ionic species avoids systematic effects if the spatial distribution is not the same for all species, and reduces systematic effects arising from isotopic line shifts. In addition, the set of Fe II transitions between λ1608 and λ2600 already provides a very sensitive combination for probing the variability of the fine-structure constant.

Each absorption component is modelled by a superposition of Doppler profiles with identical radial velocities, widths, and column densities. In addition, the value of $\Delta\alpha/\alpha$ is confined to be the same for all components. In order to find the optimal set of parameter values for both $\tau(\lambda)$ as well as $C(\lambda)$, the weighted sum of residual squares is minimized by means of an evolution strategy (ES) based on the concept of covariance matrix adaption (Hansen et al. 2003). We ignore the ensemble of Fe II λ2383 and λ2600 lines associated with the central region of the sub-DLA system since the profiles are saturated and are otherwise overemphasized in the optimization.

3.2. The regression MM (RMM) technique

The standard MM technique can conveniently be revised to avoid some of the deficiencies pointed out in Sect. 1. In effect, the revision is essentially similar to the method developed by Varshalovich & Levshakov (1993) in order to infer the cosmological variability of the proton-electron mass ratio μ from the analysis of molecular hydrogen absorption lines. Argueing by analogy (Levshakov 2004), for the regime $|\Delta\alpha/\alpha| \ll 1$ we obtain the linear approximation

$$z_i = z_\alpha + \kappa_\alpha Q_i, \tag{4}$$

where $z_i = \lambda_{\mathrm{obs,i}}/\lambda_i - 1$ and $Q_i = q_i/\omega_i$ denote the observed redshift and the sensitivity coefficient corresponding to the line i, while the slope parameter κ_α is given by

$$\kappa_\alpha = -2(1 + z_\alpha)\,(\Delta\alpha/\alpha). \tag{5}$$

If $\Delta\alpha/\alpha$ is non-zero, z_i and Q_i will be correlated and we will be able to estimate the slope κ_α and the intercept z_α from the linear regression analysis of the position of the line centroids in an absorption component. The accuracy of the regression analysis will be improved, if several absorption line samples are combined. In this case, the regression procedure can be generalized appropriately:

$$\zeta_i = (\Delta\alpha/\alpha)\,(Q_i - \bar{Q}), \tag{6}$$

where $\bar{Q}$ is the mean sensitivity coefficient of the sample and $\zeta_i = (\bar{z} - z_i)/[2(1 + \bar{z})]$ is the normalized redshift, with $\bar{z}$ denoting the mean redshift of an absorption component (in radial velocity space $\zeta_i = (\bar{v} - v_i)/[2(c + \bar{v})]$).

In order to determine the central position of several selected Fe II lines (see Sect. 4.2) we basically follow the same strategy

Table 1. Atomic data of the Fe II transitions between λ1608 and λ2600. The laboratory wavelengths λ, oscillator strengths f, and correction coefficients q are excerpted from Murphy et al. (2003, Table 2) and Dzuba et al. (2002, Table 1). The sensitivity coefficient Q is defined in Sect. 3.2. Estimiated errors are indicated in parentheses

Tr.	λ (Å)	f	q (cm^{-1})	Q
1608	1608.45080 (8)	0.058	−1300 (300)	−0.021 (5)
2344	2344.2130 (1)	0.114	1210 (150)	0.028 (4)
2374	2374.4603 (1)	0.0313	1590 (150)	0.038 (4)
2383	2382.7642 (1)	0.320	1460 (150)	0.035 (4)
2587	2586.6496 (1)	0.06918	1490 (150)	0.039 (4)
2600	2600.1725 (1)	0.23878	1330 (150)	0.035 (4)

as described in Sect. 3.1. The only differences are that we do not incorporate Eq. (3) and do not confine the radial velocities to be the same for the lines in the selected components. We point out explicitly that even though we apply a parametric profile decomposition technique to determine the position of the line centroids, the RMM analysis is not based on any specific modelling technique. In principle, the position of the line centroids can even be determined without doing any modelling at all (Levshakov 2004). Throughout the analysis we use the atomic line data listed in Table 1.

4. Results and discussion

4.1. Standard MM analysis

The optimized values of the model parameters and the standard deviations provided by the covariance matrix of the ES are listed in Table 2. The decomposition of the Fe II absorption complex is quite evident (see Figs. 1 and 2). This contrasts with the QSO absorption systems considered in former MM studies where many components are typically unresolved and many line profiles are saturated (see MWF03, Figs. 3 and 4). Clearly, the components with the most accurately defined line centroids (No. 1, 12, 20–24, 26) are the most important in the MM analysis. Expectedly, the adequate profile decomposition is reflected in the formal accuracy of the result: $\langle\Delta\alpha/\alpha\rangle_{\rm MM} = (0.1 \pm 1.7) \times 10^{-6}$ is the most stringent formal bound hitherto infered from an individual QSO absorption system. The best formal accuracy achieved in former MM analyses (see MWF03, Table 3) is exceeded by a factor of about three.

4.2. Regression MM analysis

The optimized central positions of the lines considered in the RMM analysis are listed in Table 3. We do not consider component No. 22 since the central positions of the lines in this component are strongly correlated with those in No. 21 and we ignore component No. 24 because the central position of the Fe II λ1608 line is not accurately defined. The regression line (Fig. 3) indicates no correlation between the relative displacement of the lines, ζ, and the sensitivity coefficient Q: $\langle\Delta\alpha/\alpha\rangle_{\rm RMM} = (-0.4 \pm 1.9 \pm 2.7_{\rm sys}) \times 10^{-6}$, where the statistical errors of ζ and the estimated errors of Q as well as the systematic uncertainties inherent to the wavelength calibration

Table 2. Standard MM analysis: optimized values and formal standard deviations of the radial velocities (RV), line broadening velocities b, and column densities N of the 29 components constituting the Fe II absorption complex. The optimized value of $\langle\Delta\alpha/\alpha\rangle$ is $\langle\Delta\alpha/\alpha\rangle_{\rm MM} = (0.1 \pm 1.7) \times 10^{-6}$. Radial velocity zero corresponds to the redshift $z = 1.1508$

No.	RV (km s^{-1})	b (km s^{-1})	log N (cm^{-2})
1	−534.35 ± 0.07	2.07 ± 0.16	12.29 ± 0.02
2	−530.62 ± 0.44	7.26 ± 0.41	12.06 ± 0.03
3	−510.27 ± 0.18	7.92 ± 0.36	12.14 ± 0.02
4	−494.49 ± 0.16	4.86 ± 0.32	11.91 ± 0.02
5	−471.69 ± 0.12	2.99 ± 0.20	11.91 ± 0.02
6	−448.58 ± 0.38	2.21 ± 0.87	11.15 ± 0.06
7	−416.88 ± 0.08	1.76 ± 0.20	11.91 ± 0.02
8	−403.01 ± 0.16	2.19 ± 0.37	11.79 ± 0.02
9	−393.52 ± 0.10	3.39 ± 0.22	12.12 ± 0.01
10	−375.95 ± 0.16	4.38 ± 0.22	11.77 ± 0.02
11	−321.19 ± 0.30	6.98 ± 0.58	11.52 ± 0.04
12	−239.01 ± 0.08	1.66 ± 0.11	12.55 ± 0.02
13	−235.28 ± 0.16	5.15 ± 0.15	12.51 ± 0.02
14	−182.74 ± 0.45	4.02 ± 0.42	12.07 ± 0.07
15	−175.12 ± 0.47	4.92 ± 0.40	12.18 ± 0.05
16	−137.26 ± 0.10	3.11 ± 0.18	12.05 ± 0.01
17	−123.47 ± 0.14	4.47 ± 0.20	12.00 ± 0.02
18	−53.76 ± 0.38	6.04 ± 0.59	11.43 ± 0.05
19	−34.40 ± 0.21	5.81 ± 0.36	11.77 ± 0.03
20	−14.11 ± 0.09	5.09 ± 0.10	12.85 ± 0.01
21	−1.07 ± 0.05	3.76 ± 0.06	13.56 ± 0.01
22	8.71 ± 0.06	3.46 ± 0.10	13.28 ± 0.01
23	22.12 ± 0.04	4.53 ± 0.06	13.54 ± 0.01
24	37.33 ± 0.08	6.04 ± 0.14	13.13 ± 0.01
25	59.75 ± 0.16	11.3 ± 0.3	13.48 ± 0.01
26	72.71 ± 0.06	5.69 ± 0.08	13.50 ± 0.01
27	88.98 ± 0.24	9.16 ± 0.52	12.51 ± 0.02
28	110.09 ± 1.44	11.4 ± 1.7	11.70 ± 0.08
29	134.09 ± 0.43	4.08 ± 1.00	11.19 ± 0.07

are propagated by means of Monte Carlo simulation. The coefficient of determination is $r^2 = 0.005$, i.e. only half a percent of the variation among the relative displacement of lines is accounted for by the difference in sensitivity. Consulting the t statistic, the observed data contradict the null hypothesis $\langle\Delta\alpha/\alpha\rangle = 0$ at a significance level of 9 percent, whereas the MFW04 result $\langle\Delta\alpha/\alpha\rangle = -5.7 \times 10^{-6}$ is contradicted at 88 percent.

4.3. Systematic effects

Contributing to the discussion of potential systematic effects presented in MWF03 and MFW04, we recall attention to another important source of error. As formerly illustrated by Levshakov & D'Odorico (1995) and Levshakov (1994), the presence of unresolved narrow lines with different optical depths can strongly affect the position of the line centroids in an ensemble of lines and result in a biased expectation value $\langle\Delta\alpha/\alpha\rangle$. This effect will be most noticeable in the case of optically thick lines. In fact, the expectation value $\langle\Delta\alpha/\alpha\rangle_{\rm MM}$ increases by 3.6×10^{-6} if we do not ignore the ensemble of sat-

Table 3. Regression MM analysis: optimized centroid positions (Å) of the Fe II lines between λ1608 and λ2600 in the selected absorption components. Formal standard deviations are indicated in parentheses

No.	1608	2344	2374	2383	2587	2600
1	3453.2908 (57)	5032.9469 (24)		5115.7159 (17)	5553.4531 (29)	5582.4812 (19)
12	3456.6993 (39)	5037.9119 (23)	5102.9147 (36)	5120.7677 (21)	5558.9313 (28)	5587.9914 (21)
20	3459.2892 (37)	5041.6969 (25)	5106.7434 (36)	5124.6089 (22)	5563.1057 (30)	5592.1855 (24)
21	3459.4431 (11)	5041.9145 (12)	5106.9734 (12)		5563.3452 (11)	
23	3459.7131 (13)	5042.3034 (10)	5107.3695 (16)		5563.7764 (11)	
26	3460.2938 (17)	5043.1547 (15)	5108.2272 (21)		5564.7129 (16)	

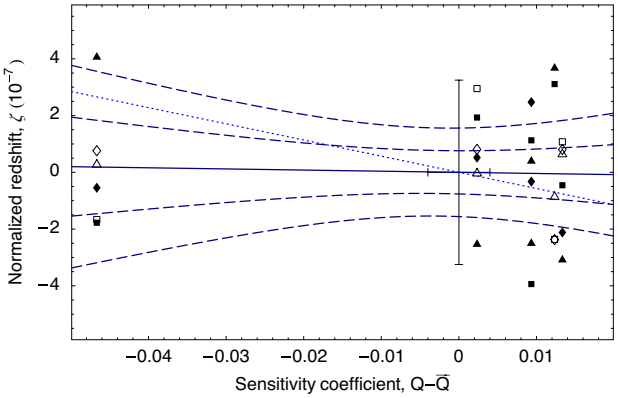

Fig. 3. Regression MM analysis of the lines listed in Table 3. Each component is represented by a different symbol. The regression line $\langle\Delta\alpha/\alpha\rangle_{\rm RMM} = -0.4 \times 10^{-6}$ and its 68 and 95 percent confidence limits are marked by the solid and dashed curves, respectively, whereas the dotted line indicates the MFW04 result $\langle\Delta\alpha/\alpha\rangle = -5.7 \times 10^{-6}$. The median total errors of ζ and Q are illustrated

urated Fe II λ2383 and λ2600 profiles in the optimization, and the systematic increase of variance in the normalized residuals with increasing optical depth (see Figs. B.1 and B.2 provided in the Online Material) might well be explained by the presence of unresolved narrow lines.

5. Conclusions

Our results strongly support the null hypothesis of a non-varying fine-structure constant, but do not contradict the MFW result $\langle\Delta\alpha/\alpha\rangle = -5.7 \times 10^{-6}$ at a significance level higher than 88 percent. Nevertheless, we conclude: (i) The MM technique is capable of providing stringent bounds on $\langle\Delta\alpha/\alpha\rangle$ even if the analysis is restricted to the Fe II lines only. (ii) The RMM technique is illustrative and methodically more transparent than the standard MM technique. In addition, the regression analysis facilitates the consideration of systematic errors inherent to the wavelength calibration of QSO spectra. (iii) The accuracy of the individual $\Delta\alpha/\alpha$ assessment is principally limited by systematic errors inherent to the wavelength calibration. The accuracy attainable with high-quality QSO spectra recorded with the UVES spectrograph is limited to 10^{-5}. (iv) Optically thick profiles are susceptible to systematic effects biasing the expectation value $\langle\Delta\alpha/\alpha\rangle$. (v) We suggest the analysis of an extensive homogenous sample of Fe II absorption lines to provide an independent and crucial test of the MFW04 result.

Besides, HE 0515–4414 is the brightest known intermediate redshift QSO in the sky and is therefore predestinated for spectroscopy with the new High Accuracy Radial velocity Planet Searcher (HARPS) operated at the ESO La Silla 3.6 m telescope. This very high-resolution spectrograph is specified to provide an efficient wavelength calibration facilitating the performance of radial velocity measurements with an accuracy of up to 1 m s^{-1} (Pepe et al. 2002). Presumably, HARPS will improve the accuracy of the individual $\Delta\alpha/\alpha$ assessment by more than an order of magnitude.

Acknowledgements. We kindly thank Michael Murphy for thorough comments on the manuscript. This research has been supported by the Verbundforschung of the BMBF/DLR under Grant No. 50 OR 9911 1. SAL has been supported by the RFBR Grant No. 03-02-17522.

References

Bahcall, J. N., Steinhardt, C. L., & Schlegel, D. 2004, ApJ, 600, 520
de la Varga, A., Reimers, D., Tytler, D., Barlow, T., & Burles, S. 2000, A&A, 363, 69
Dzuba, V. A., Flambaum, V. V., & Webb, J. K. 1999, Phys. Rev. A, 59, 230
Dzuba, V. A., Flambaum, V. V., Kozlov, M. G., & Marchenko, M. 2002, Phys. Rev. A, 66, 022501
Edlén, B. 1966, Metrologica, 2, 71
Hansen, N., Müller, S. D., & Koumoutsakos, P. 2003, Evol. Comput., 11, 1
Levshakov, S. A. 1994, MNRAS., 269, 339
Levshakov, S. A. 2004, Lect. Not. Phys., 648, 151
Levshakov, S. A. & D'Odorico, S. 1995, in QSO Absorption Lines, ESO Astrophys. Symp., 202
Murphy, M. T., Webb, J. K., Flambaum, V. V., Churchill, C. W., & Prochaska, J. X. 2001a, MNRAS., 327, 1223
Murphy, M. T., Webb, J. K., Flambaum, V. V., Prochaska, J. X., & Wolfe, A. M. 2001b, MNRAS., 327, 1237
Murphy, M. T., Webb, J. K., & Flambaum, V. V. 2003, MNRAS., 345, 609 (MWF03)
Murphy, M. T., Flambaum, V. V., Webb, J. K., et al. 2004, Lect. Not. Phys., 648, 131 (MFW04)
Olive, K. A., Pospelov, M., Qian, Y.-Z., et al. 2004, Phys. Rev. D, 69, 027701
Pepe, F., Mayor, M., & Rupprecht, G. 2002, ESO Mess., 110, 9
Quast, R., Baade, R., & Reimers, D. 2002, A&A, 386, 796
Reimers, D., Hagen, H.-J., Rodriguez-Pascual, P., & Wisotzki, L. 1998, A&A, 334, 96
Reimers, D., Baade, R., Quast, R., & Levshakov, S. A. 2003, A&A, 410, 785
Uzan, J. P. 2003, Rev. Mod. Phys., 75, 403
Varshalovich, D. A. & Levshakov, S. A. 1993, JETP Lett., 58, 237

Online Material

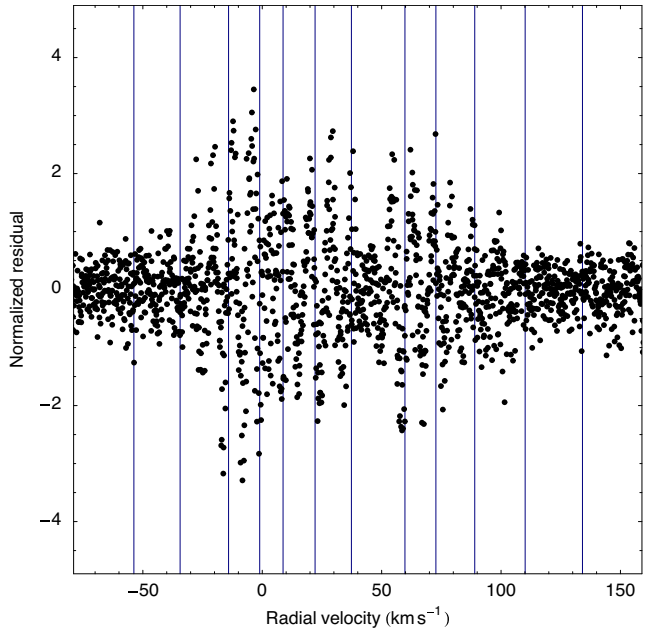

Fig. B.1. Normalized residuals of the optimized RMM model. For the purpose of residual analysis the calculation of the sum of residual squares takes into account the optically thick parts of the line ensemble

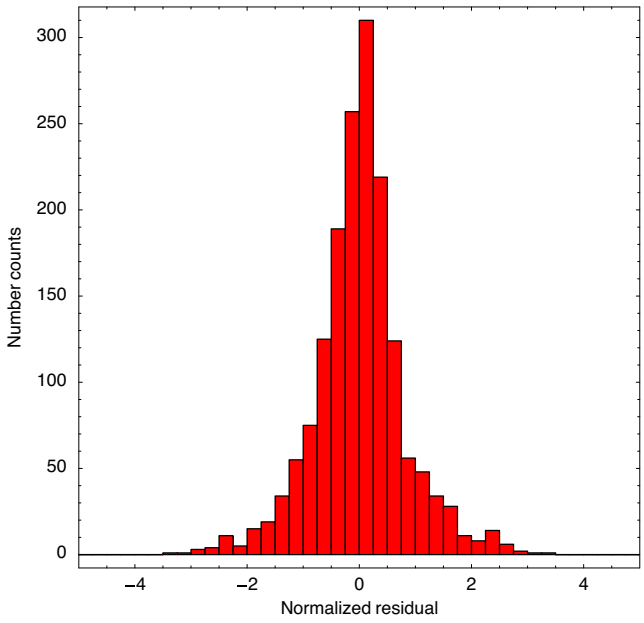

Fig. B.2. Number distribution of the normalized residuals rendered in Fig. B.1. The distribution is approximately normal with zero mean and does not indicate any obvious misspecification of the model

Appendix A: Derivation of Eqs. (4) and (6)

In the regime $|\Delta\alpha/\alpha| \ll 1$ Eq. (3) reduces to the linear limit

$$\omega_{\alpha,i} = \omega_i + 2q_i(\Delta\alpha/\alpha). \tag{A.1}$$

Dividing by ω_i and substuting $\omega_i = (1 + z_i)/\lambda_{\mathrm{obs},i}$ and $\omega_{\alpha,i} = (1 + z_\alpha)/\lambda_{\mathrm{obs},i}$, we obtain

$$\frac{1 + z_\alpha}{1 + z_i} = 1 + 2(\Delta\alpha/\alpha)Q_i \tag{A.2}$$

or equivalently

$$z_i = z_\alpha - 2(1 + z_i)(\Delta\alpha/\alpha)Q_i. \tag{A.3}$$

Substituting Eq. (A.3) into itself and neglecting non-linear terms we arrive at

$$z_i = z_\alpha - 2(1 + z_\alpha)(\Delta\alpha/\alpha)Q_i \tag{A.4}$$

which is equivalent to Eq. (4). The intercept z_α of the regression line Eq. (4) is calculated as

$$z_\alpha = \bar{z} - \kappa_\alpha \bar{Q}. \tag{A.5}$$

Substituting Eq. (A.5) into Eq. (4) and neglecting non-linear terms we obtain

$$\bar{z} - z_i = 2(1 + \bar{z})(\Delta\alpha/\alpha)(Q_i - \bar{Q}), \tag{A.6}$$

which is equivalent to Eq. (6).

Appendix B: Residual analysis

The crucial point in any MM analysis is the specification of the number of absorption components to be incorporated in the model of the optical depth. The analysis of the normalized residuals of the optimized model reveals a systematic increase of variance with increasing optical depth (Fig. B.1). The addition of further absorption components does decrease the variance but the resulting optimized models exhibit unresolved and ambigously positioned narrow lines. Nevertheless, the resulting expectation values $\langle\Delta\alpha/\alpha\rangle$ are consistent with the results presented in Sect. 4, even in case we do not ignore the optically thick parts of the line ensemble.

The systematic increase of variance with increasing optical depth visible in Fig. B.1 might well be explained by the presence of unresolved narrow lines or by deviations from the Voigt profile resulting from kinematic effects due to e.g. mesoturbulent velocity fields and rotational motion. The number distribution of normalized residuals is approximately normal with zero mean (Fig. B.2) and does not indicate any obvious misspecification of the model.

Cosmochemistry, Cosmology, and Fundamental Constants High-Resolution Spectroscopy of Damped Lyman-Alpha Systems

R. Quast, D. Reimers
Hamburger Sternwarte, Universität Hamburg, D-21029 Hamburg, Germany
A. Smette, O Garcet
Institut d'Astrophysique et de Géophysique, Université de Liège, B-4000 Liège, Belgium
C. Ledoux
European Southern Observatory, Santiago, Chile
S. Lopez
Departamento de Astronomía, Universidad de Chile, Santiago, Chile
L. Wisotzki
Astrophysikalisches Institut Potsdam, D-14482 Potsdam, Germany

Spectroscopy of QSO absorption lines provides essential observational input for the study of nucleosynthesis and chemical evolution of galaxies at high redshift. But new observations may indicate that present chemical abundance data are biased due to deficient spectral resolution and unknown selection effects: Recent high-resolution spectra reveal the hitherto unperceived chemical nonuniformity of a molecule-bearing damped Lyman-alpha (DLA) system, and the still ongoing H/ESO DLA survey produces convincing evidence for the effect of dust attenuation. We present a revised analysis of the H_2-bearing DLA complex toward the QSO HE 0515–4414 showing nonuniform differential depletion of chemical elements onto dust grains, and introduce the H/ESO DLA survey and its implications. Conclusively, we aim at starting an unbiased chemical abundance database established on high-resolution spectroscopic observations. New data to probe the temperature-redshift relation predicted by standard cosmology and to test the constancy of fundamental constants will be potential spin-offs.

1. CHEMICAL UNIFORMITY AT HIGH Z?

In stark contrast to many interstellar lines-of-sight in the Milky Way or the Magellanic Clouds, high-redshift DLA systems usually appear to be chemically uniform [1]. But despite their chemical uniformity, for any redshift the observed metallicities are different by up to two orders of magnitude [2].

The known DLA systems make a heterogeneous population involving very different physical environments – a very unfavorable precondition for tracing nucleosythesis and the chemical evolution of galaxies. But the physical environments of molecular clouds are less diverse. In fact, for the known H_2-bearing DLA systems the metallicity-redshift distribution may exhibit less variation than for the regular DLA systems [3].

Molecular hydrogen is detected in DLA components exhibiting high particle densities and low kinetic temperatures [4, 5]. The metallicity of DLA systems is usually calculated by averaging ad hoc radial velocity intervals, i.e. by averaging several absorption components. But the depletion of chemical elements in H_2-bearing components may surpass the average by up to one order of magnitude [4, 5]. Moreover, narrow components arising from cold gas are blurred in the usually complex absorption profiles.

In fact, high-resolution (55 000) and exceptionally high signal-to-noise (90-140) spectra of the H_2-bearing DLA system toward the QSO HE 0515–4414 indicate the hitherto unperceived chemical nonuniformity of individual metal absorption profile components, similar to the interstellar lines-of-sight intersecting Galactic warm disk and halo clouds (Figs. 1, 2). In addition, for the H_2-bearing components the calculated [6] fraction of iron in dust of 98 percent is close to that of Galactic cold disk gas. Is the DLA system toward HE 0515–4414 just a rare case, or are compact high-metallicity dust clouds systematically missed in present spectroscopic observations due to insufficient resolution or low signal-to-noise ratio?

2. FAINT QSOS OBSCURED BY DUST?

The possibility that present surveys of DLA systems are affected by dust is an ongoing concern: If the extinction of DLA absorbers is high enough, optical surveys will miss the QSOs behind them. However, present samples of DLA absorbers toward radio-selected and SDSS QSOs do not indicate any distinct selection bias due to dust [8, 9].

In contrats, the new H/ESO survey of DLA systems toward a complete subsample of 182 HE QSOs produces convincing evidence for the effect of dust attenuation: Four new DLA systems were discovered toward the bright half of the QSO subsample, but 14 were detected toward the faint. The probability for both numbers being drawn from the same Poissonian is less than 2.5 percent (Fig. 3). Do the DLA systems toward the fainter QSOs exhibit more dust than those toward the bright?

3. FUTURE AIMS

In order to study the possible biases and selection effects involved with duts, we aim at starting a sound abundance database established on high-resolution and high signal-to-noise spectroscopy of the complete sample of DLA systems discovered by the H/ESO survey. The database will

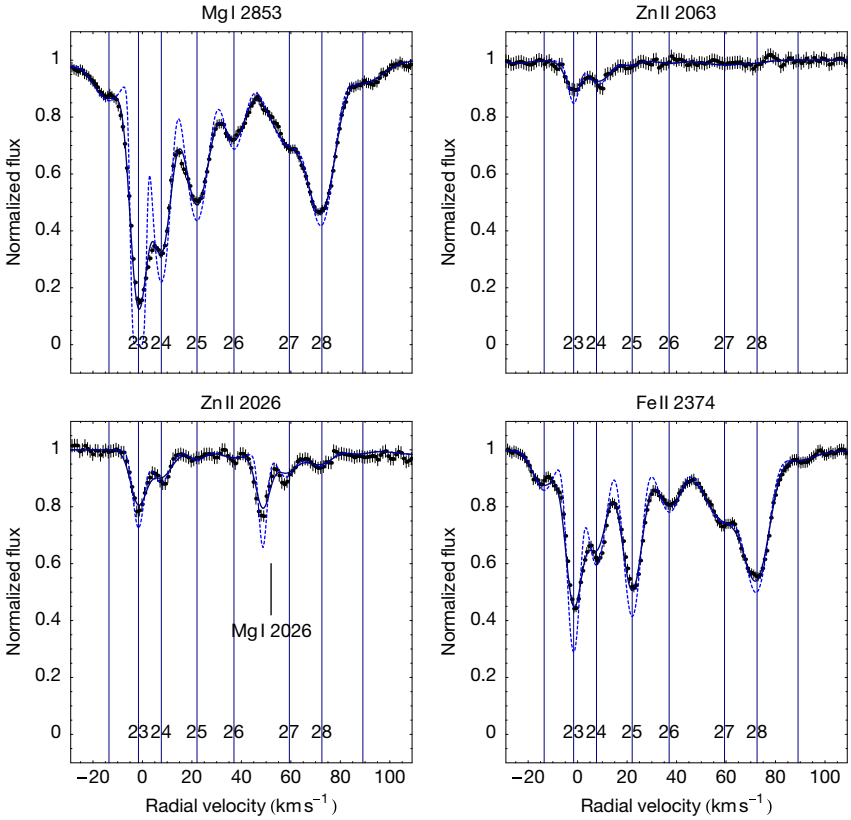

Figure 1: Selected metal absorption profiles associated with the DLA system toward HE 0515–4414. The blue curves indicate the optimized profile decomposition and its deconvolution. Individual components are labeled by numbers 23-28. Note the different optical depths of Fe II and Zn II for the H_2-bearing componets 23/24 and component 28. Component 23 also exhibits rare neutral species (S I, Si I, Fe I). Radial velocity zero corresponds to the redshift $z = 1.1508$.

be extremely useful for studying the physical conditions in DLA systems, and may shed some light on the star formation history of the universe and the problem of missing metals [10, 11].

As spin-off product, newly detected C I and C II fine-structure absorption lines may be used to test the temperature-redshift relation predicted by the standard big-bang cosmology. A further potential spin-off will be a homogenous sample of Fe II lines suitable for probing the hypothetical variation of the fine-structure constant α by means of the regression many multiplet method [12, 13].

Acknowledgments

This research is based on observations made with the ESO Very Large Telescope under Programme ID 066.A-0212 and hs been funded by the Verbundforschung of the BMBF/DLR under Grant No. 50 OR9911 1.

References

[1] J. X. Prochaska, ApJ **582**, 49 (2003).
[2] J. X. Prochaska, E. Gawiser, A. M. Wolfe, S. Castro, and S. G. Djorgovski, ApJ **595**, L9 (2003).
[3] S. J. Curran, J. K. Webb, M. T. Murphy, and R. F. Carswell, MNRAS **351**, L24 (2004).
[4] P. Petijean, R. Srianand, and C. Ledoux, MNRAS **332**, 383 (2002).
[5] C. Ledoux, P. Petijean, and R. Srianand, MNRAS **346**, 209 (2003).
[6] G. Vladilo, A&A **421**, 479 (2004).
[7] D. E. Welty, J. T. Lauroesch, J. C. Blades, L. M. Hobbs, and D. G. York, ApJ **554**, L75 (2001).
[8] S. L. Ellison, C. W. Churchill, S. A. Rix, and M. Pettini, ApJ **615**, 118 (2004).
[9] M. T. Murphy and J. Liske, MNRAS **354** (2004).
[10] A. M. Wolfe, J. X. Prochaska, and E. Gawiser, ApJ **593**, 215 (2003).
[11] A. M. Wolfe, E. Gawiser, and J. X. Prochaska, ApJ **593**, 235 (2003).
[12] S. A. Levshakov, Lect. Not. Phys. **648**, 151 (2004).
[13] R. Quast, D. Reimers, and S. A. Levshakov, A&A **415**, L7 (2004).

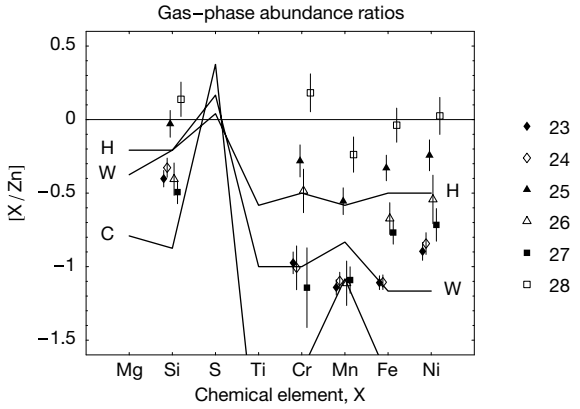

Figure 2: Evidence for chemical nonuniformity at high redshift. Gas-phase abundance ratios (relative to solar ratios) for the absorption components shown in Fig. 1 compared with typical values found for Galactic cold (C) and warm (W) disk and halo (H) clouds [7]. Since the volatile element Zn is only mildly depleted, the abundance ratios reflect the differential depletion of chemical elements into dust. Note that Cr, Mn, Fe, and Ni are strongly depleted in the H_2-bearing components 23/24 but appear essentially undepleted in component 28.

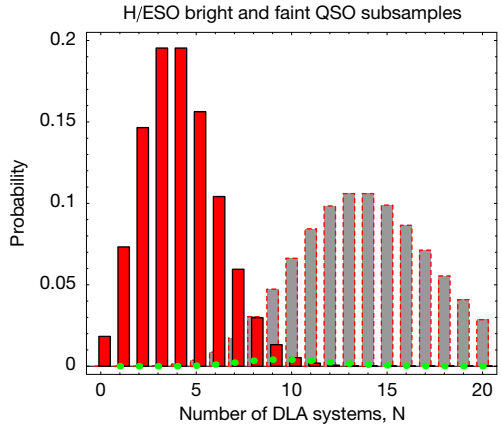

Figure 3: Evidence for attenuation of fainter QSOs by dust. The number of DLA systems detected toward the bright (faint) half of 182 HE QSOs is 4 (14). The absorption paths of both subsamples exhibit almost the same length. Two Poissonians with means 4 and 14 are marked by, respectively, the red and gray vertical bars. The probability for both numbers being drawn from the same Poissonian with mean N is indicated by green dots.